

Stability of a Laminar Streaky Boundary-Layer Behind a Roughness Element

A thesis accepted by the Faculty of Aerospace Engineering and Geodesy of the
Universität Stuttgart in partial fulfillment of the requirements for the degree of
Doctor of Engineering Sciences (Dr.-Ing.)

By

Shin Yong-su

born in Seoul, Korea Republic

main referee: apl. Prof. Dr.-Ing. U. Rist

co referee: Prof. Dr.-Ing. C. Brücker

Prof. Dr.-Ing. E. Krämer

Date of defence: February 17, 2015

Institute of Aerodynamics and Gas Dynamics

University of Stuttgart

2015

Contents

Nomenclature	III
Abstract	VII
Zusammenfassung	IX
1 Introduction	1
1.1 Background	1
1.2 State of the art	3
1.2.1 Paths to turbulence	3
1.2.2 Streamwise elongated streaks	8
1.3 Present contributions and overview	11
2 Bi-global Linear Stability Theory	15
2.1 Linear stability theory	15
2.2 Bi-global approach	19
2.2.1 Governing equations and boundary conditions	20
2.2.2 Numerical method	22
3 Experimental Setup	25
3.1 Laminar water channel	25
3.2 Roughness element	28
3.3 Flow condition	31
3.4 Measurement techniques	36

II

3.4.1	Constant temperature anemometry	37
3.4.2	Particle image velocimetry	40
3.5	Asymmetrical external forcing	43
4	Streaky Boundary-layer Flow	45
4.1	Wall-normal shear and separation	45
4.2	Streamwise elongated streaks	48
5	Linear Stability Analysis	57
5.1	Eigenmode spectrum	57
5.2	Varicose and sinuous mode	62
5.2.1	Eigenfunctions	62
5.2.2	Experimental measurements	65
5.2.3	Streamwise development of disturbances	71
5.3	Asymmetric external forcing	76
6	Nonlinear Instability	83
6.1	Nonlinear secondary growth	83
6.2	Breakdown	86
7	Summary and Conclusions	91
A	Technical Data	95
B	Installation of the Flat Plate in the Test Section	97
C	Calibration of the CTA System with Hot-film Probe	101
	Bibliography	105

Nomenclature

Roman

a	Over-heat ratio of hot-film sensor
c_{gr}, c_{ph}	Group and phase velocity
D	Diameter of a pipe
d	Distance
d_R	Diameter of roughness element
f	Frequency
f_g	Cut-off frequency
f_{Ny}	Nyquist frequency
h	Height of roughness element
L	Reference length
N	Number of points
p	Pressure
q_0, q'	Steady and fluctuating physical parameter vector
Re	Reynolds number VD/ν
Re_h	Roughness-height Reynolds number hu_h/ν
Re_x	Streamwise Reynolds number ux/ν
Sr	Strouhal number
t	Time
Tu	Turbulence intensity
$\bar{u}, \bar{v}, \bar{w}$	Averaged steady velocity components
$\hat{u}, \hat{v}, \hat{w}$	Amplitude components of eigenfunction

IV

\tilde{u}	By e^N -factor corrected amplitude in streamwise direction
u', v', w'	Fluctuating velocity components
u_e	Free-stream velocity
u_h	Boundary-layer velocity at the height of roughness element in a case without the roughness element
u_p	Streamwise velocity difference $u(z) - u(z_{max})$
V	Averaged flow velocity in a pipe
x, y, z	Cartesian coordinate system, x streamwise, y wall-normal, and z spanwise direction
x_R	Streamwise position of roughness element
y_{max}	Maximum length in wall-normal direction

Greek

α, β	Streamwise and spanwise complex wave number
δ_1	Displacement thickness of boundary-layer
δ_r	Phase shift factor in the Floquet system
η'	Fluctuating wall-normal vorticity
$\hat{\eta}$	Vorticity amplitude
ν	Kinematic viscosity
ω_x	Streamwise vorticity distribution
ω	Complex angular frequency
Φ	Phase distribution
ρ	Density
τ	Settling time after a move of hot-film probe
ξ	Streamwise coordinate component based on phase velocity

Subscript

A	Air
avg	Averaged value
c	Cathode
R	Roughness element

<i>ref</i>	Reference value
<i>s, t</i>	Spatial, temporal
<i>vari, sinu</i>	Varicose and sinuous mode
<i>W</i>	Water
<i>w</i>	Wire

Acronyms

CFD	Computational Fluid Mechanics
CTA	Constant Temperature Anemometer
DLR	German Aerospace Center, Deutsches Zentrum für Luft- und Raumfahrt e.V.
DNS	Direct Numerical Simulation
DPSS	Diode-Pumped Solid-State
FFT	Fast Fourier Transform
HP	High-Pass
IAG	Institut für Aerodynamik und Gasdynamik
LP	Low-Pass
LST	Linear Stability Theory
LWK	Laminar Water Channel, Laminarwasserkanal
ODE	Ordinary Differential Equation
PIV	Particle Image Velocimetry
TS	Tollmien-Schlichting
TTL	Transistor-to-Transistor Logic

Abstract

Analysis of flow instability is of importance to understand laminar-turbulent transition which is a crucial factor for aerodynamic performance. The present study deals with influences of a roughness element on the flow instability of a laminar boundary-layer. Roughness elements in laminar boundary-layers generate localized disturbances. They grow transiently and formulate streamwise elongated streaky structures downstream. Spanwise periodicity of these streaky structures disturbs the streamwise development of two-dimensional Tollmien-Schlichting waves in a laminar boundary-layer. In this way, a delay of the laminar-turbulent transition is achieved (*flow stabilization*). On the other side, physically unavoidable velocity reduction behind the roughness elements brings on high shear layers in wall-normal direction at the same time. Also, separations or strong vortical structures occur occasionally depending on both shape of the roughness elements and flow conditions. They cause a flow destabilization and sometimes trigger a bypass transition. Because these two opposite phenomena happen concurrently and interact with each other, it is difficult to precisely understand the instability mechanisms provoked by the roughness elements.

Therefore, the goal of the present work is to study the stability of a laminar streaky layer induced by a roughness element. This work consists of two parts: Bi-global linear stability analysis and experimental measurements. A complex instability procedure of the three-dimensional streaky layers arranged parallel in streamwise and periodical in spanwise direction can be analysed by a bi-global approach. Corroborating experiments were conducted in the laminar water chan-

VIII

nel at the University of Stuttgart. Simultaneous operation of two hot-film probes and signal processing enabled to find the theoretically calculated unstable eigenmodes in practical flow. In addition, observations of both velocity distribution in a complex flow field and nonlinear vortex structures were carried out by a flow visualization using a hydrogen-bubble method and Particle-Image-Velocimetry measurements.

As a result, a streaky layer which includes streamwise elongated high- and low-speed streaks and a separation behind the roughness element was found by a CFD computation using a laminar solver and confirmed by time-averaged experimental velocity components. The bi-global LST identified two highly unstable eigenmodes. These eigenmodes oscillate symmetrically and asymmetrically with respect to the spanwise coordinates and were accordingly termed varicose and sinuous mode, respectively. Their streamwise evolution depends mainly on a streamwise development of the streaks. Experimental results confirmed the presence of these two unstable modal modes. The varicose mode dominates flow instability, and the sinuous mode has a smaller signal-to-noise ratio.

Additionally, an external forcing was tried to increase the initial amplitude of the smaller sinuous mode with respect to the varicose one. Despite some deficiencies of the experimental setup, a separate artificial amplification of a specific eigenmode, i.e. the sinuous mode, was possible. In the latter part of the present study, the nonlinear behaviour of the streaky layer further downstream and the breakdown under an over-critical condition were explored. Because the *linear* theory cannot calculate nonlinear instability, complex three-dimensional flows and vortical structures were investigated by experimental flow visualization methods, and an evolution from nonlinear streaks to hairpin vortices was detected.

Zusammenfassung

Die Analyse der Strömungsinstabilität ist bedeutungsvoll um die laminar-turbulente Transition, die ein entscheidender Faktor für aerodynamische Leistungen ist, zu verstehen. Die vorliegende Studie befasst sich mit Einflüssen eines Rauigkeitselements auf die Strömungsinstabilität einer laminaren Grenzschicht. Rauigkeitselemente in laminaren Grenzschichten erzeugen lokale Störungen. Sie wachsen vorübergehend und bilden längliche *streaky*-Strukturen in Strömungsrichtung. Spannweite Periodizität dieser *streaky*-Strukturen stört die Entwicklung von zwei-dimensionalen Tollmien-Schlichting-Wellen in Strömungsrichtung. Auf diese Weise wird eine Verzögerung der laminar-turbulenten Transition erreicht (*Strömungsstabilisierung*). Auf der anderen Seite bringt die physikalisch unvermeidbare Geschwindigkeitsreduzierung hinter den Rauigkeitselementen zur gleichen Zeit Hoch-Scherschichten in der Wandnormalrichtung hervor. Auch entstehen Ablösungen oder starke Wirbelstrukturen abhängig sowohl von der Form des Rauigkeitselements als auch von den Strömungsverhältnissen. Sie verursachen eine Destabilisierung der Strömung und lösen manchmal eine *bypass*-Transition aus. Da diese beiden entgegengesetzten Erscheinungen gleichzeitig geschehen und miteinander interagieren, ist es schwierig, die Mechanismen der bei den Rauigkeitselementen provozierten Strömungsinstabilität genau zu verstehen.

Daher ist das Ziel dieser Arbeit, die Stabilität der bei einem Rauigkeitselement induzierten laminaren *streaky*-Schicht zu untersuchen. Die Arbeit besteht aus zwei Teilen einer bi-globalen linearen Stabilitätsanalyse und experimentellen Messungen. Ein komplexes Stabilitätsverhalten der drei-dimensionalen *streaky*-Schicht, die parallel in Strömungsrichtung und periodisch in Spannweitenrich-

tung angeordnet ist, kann durch einen bi-globalen Ansatz analysiert werden. Bestätigende Experimente wurden im Laminarwasserkanal der Universität Stuttgart durchgeführt. Der gleichzeitige Betrieb von zwei Heißfilmsonden und Signalverarbeitung ermöglichten, die theoretisch berechneten instabilen Eigenmoden in der praktischen Strömung zu finden. Darüber hinaus Beobachtungen sowohl der Geschwindigkeitsverteilung im einen komplexen Strömungsfeld und nicht-linearen Wirbelstrukturen wurden durch eine Strömungsvisualisierung mit Hilfe einer Wasserstoff-Blasenmethode und *Particle-Image-Velocimetry* Messungen durchgeführt.

Als Ergebnis wurden die länglichen *high- and low-speed streaks* in der Strömungsrichtung und eine Ablösung hinter dem Rauigkeitselement durch eine CFD-Berechnung gefunden und von den gemittelten experimentellen Geschwindigkeitskomponenten bestätigt. Die bi-globale LST hat zwei hoch instabile Eigenmoden identifiziert. Diese Eigenmoden schwingen symmetrisch und asymmetrisch in Bezug auf die spannweite Koordinate und sind entsprechend mit *varicose* und *sinuous* bezeichnet. Die Entwicklung der instabilen Eigenmoden in Strömungsrichtung wurden auf einer Entwicklung der *streaks* basiert. Experimentelle Ergebnisse bestätigten das Vorhandensein der beiden instabilen Moden. Die *varicose*-Mode dominiert die Strömungsinstabilität und die *sinuous*-Mode hat eines kleineres Signal-zu-Rausch-Verhältnis.

Zusätzlich wurde durch eine externe Anregung versucht, die initiale Amplitude der kleineren *sinuous*-Mode zu erhöhen. Trotz einigen Schwächen des experimentellen Aufbaus war eine separate künstliche Amplifikation einer spezifischen Eigenmode, d.h. der *sinuous*-Mode, möglich. Im letzten Teil der vorliegenden Studie wurden der nichtlineare Verhalten der *streaky*-Schicht weiter stromabwärts und der Zusammenbruch im überkritischen Zustand untersucht. Da die *lineare* Theorie keine nichtlineare Instabilität berechnen kann, wurden komplexe drei-dimensionale Strömungen und Wirbelstrukturen durch experimentelle Strömungsvisualisierungsmethoden beobachtet. Eine Entwicklung aus der nichtlinearer *streaks* in Haarnadelwirbel wurde festgestellt.

Chapter 1

Introduction

1.1 Background

Laminar and turbulent boundary-layer The velocity at the immediate surface of aerodynamical bodies is zero (no-slip condition) in viscous flows. The velocity increases gradually in wall-normal direction and finally reaches the free-stream velocity. Prandtl (1904) divided for the first time such a flow field into two regions: a very thin layer adjacent to the surface, in which the fluid viscosity plays an important role, is defined as *boundary-layer*. The frictionless flow outside the layer, which has a non-viscous effect, is called irrotational potential flow.

Reynolds (1883) in his experiment using a flow along a pipe showed a transition from laminar to turbulent flow, as a dimensionless number exceeds a critical value. This dimensionless number, now called Reynolds number, is expressed as the ratio of inertia and viscous forces, $Re = VD/\nu$, and it consists of flow velocity V , the diameter of the pipe D and the kinematic viscosity of fluid ν . In a similar manner, *laminar-turbulent transition* of boundary-layers (cf. Figure 1.1) can be also characterized by the streamwise Reynolds number $Re_x = ux/\nu$, where x is the streamwise distance from the leading edge. At small Re_x below a critical number Re_{cr} where transition occurs, stable fluid elements move along a straight path in downstream direction while maintaining a relatively thin layer thickness

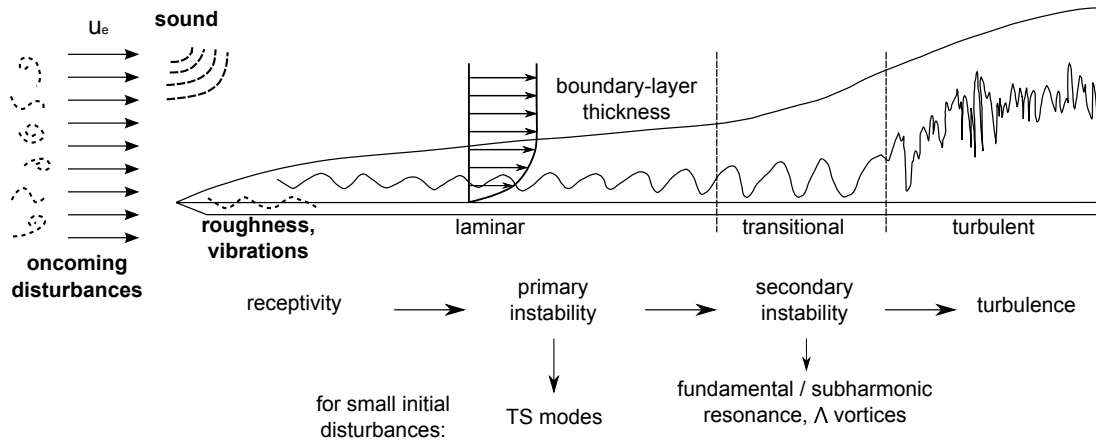


Figure 1.1: Laminar and turbulent boundary-layer on a flat plate and evolution of its instability (Kloker, 2008)

(*laminar boundary-layer*). As Re_x increases, namely, as boundary-layer flow evolves in downstream direction, flow instability grows and unstable random eddies appear in the boundary-layer. They actively transport high energy momentum fluid and the velocity distribution consequently becomes more uniform in wall-normal direction (*turbulent boundary-layer*). Accordingly, friction drag at the wall also increases (Schlichting and Gersten, 2000).

Flow stabilization Although the boundary-layer flow has been comprehensively studied for over a century, the stability problems related with the laminar-turbulent transition and flow stabilization catch still many attentions in both environmental and economical aspects (Green, 2008). Nowadays, more strict environmental regulations about CO_2 production and a continuous increase of oil price intensively pressure a reduction of oil consumption of transportation vehicles, for example, airplanes or automobiles. In terms of aerodynamics, because turbulent boundary-layers make larger wall friction than laminar ones, flow stabilization for delaying the transition and maintaining the laminar boundary-layer as long as possible is of importance to save the oil consumption.

There have been many efforts to delay the laminar-turbulent transition. Suction at the wall (Schrauf (2005); Friederich and Kloker (2012)) retains laminar boundary-layer by pulling high-momentum fluid towards the wall which leads

to attenuated growth of flow instability. Another recent active method is the dielectric barrier discharge (DBD) actuator (Duchmann et al., 2013) by which fluids are displaced into the plasma state and then draws the high-momentum energy upper boundary-layer onto the bottom. As a passive stabilization method, usage of an array of roughness elements (Fransson et al. (2005); Fransson et al. (2006); Fransson and Talamelli (2012)) has been introduced. In fact, surface roughness, for example insects or dust on the wing surface, has been considered as a factor to produce aerodynamic resistance or noise by increasing the flow instability. However, the studies about streamwise elongated streaks in laminar boundary-layers have showed that roughness elements having an appropriate shape and size can delay the laminar-turbulent transition. Particularly, this passive method is a very efficient way due to an easy install and a saving of additional operating energy. In a similar manner, Shahinfar et al. (2012) used an array of passive vortex generators to maximize this stabilising effect.

1.2 State of the art

In this section, several scenarios passing from laminar to turbulent boundary-layer (Subsection 1.2.1) are summarized. Previous studies of flow instability with localized disturbances generated by roughness elements are the particular focus here. Subsection 1.2.2 introduces streamwise elongated streaks in boundary-layers which are induced by roughness elements.

1.2.1 Paths to turbulence

Initial disturbances in boundary-layers are formed by surrounding conditions, e.g., vortical disturbances in free-stream and external acoustic perturbations (see Figure 1.1). Local changes in the boundary-layers, such as surface roughness and vibrations, or wall-curvatures, also play an important role in the initiation of dis-

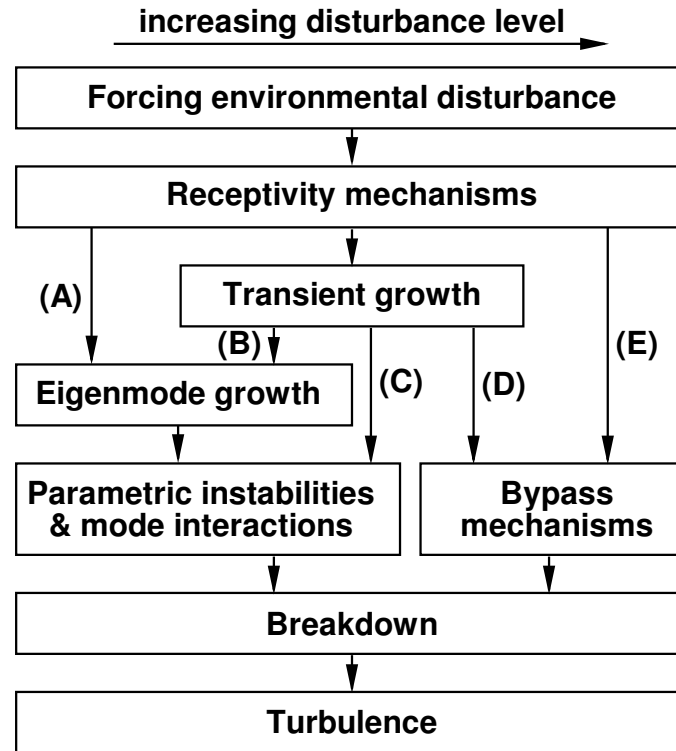


Figure 1.2: Paths to turbulence (Reshotko, 2001)

turbances in the boundary-layer. This entrainment process of initial disturbances into the boundary-layer has been called *receptivity* (Morkovin, 1968). As seen in Figure 1.2, paths of flow instability from laminar to turbulence are distinguished by the magnitude of initial disturbances forced by the receptivity mechanism.

Classical scenario: TS path and bypass transition Infinitesimal initial disturbances in a boundary-layer generated by a low-level external perturbation are developed into two-dimensional disturbance waves stretched parallel in a span-wise direction, so-called Tollmien-Schlichting (TS) waves. Theoretically (cf. Linear Stability Theory in Section 2.1), they are calculated with an assumption of normal mode in linearized perturbation equations (Tollmien (1929); Schlichting (1933)). These eigenmodes grow exponentially in the downstream direction (*TS path*, Path (A) in Figure 1.2), process called *primary instability* (cf. Figure 1.1). Experimentally, under a very low-level turbulence intensity $Tu < 0.1\%$ of a wind tunnel with controlled disturbance input (Schubauer and Skramstad, 1943), this theoretical

primary instability has been confirmed.

Subsequently, as they reach an amplitude above an order of 1 % of free-stream velocity, the TS waves evolve into a new steady or quasi-steady state which consists of spanwise vorticity structures (Schmid and Henningson, 2000). At this stage (*secondary instability*, see Figure 1.1), Klebanoff et al. (1962) experimentally found spikes which are large amplitudes in a short-time event and initiate turbulence. A numerical study by Rist and Fasel (1995) shows these spikes as a high wall-normal shear on a head of three-dimensional Λ -vortices. These Λ -vortices are experimentally observed as a fundamental (K-type) and subharmonic (N- or H-type) mode in staggered pattern (detailed in Kachanov (1994)). A *breakdown* of these three-dimensional vortical structures occurs when lifting the head and growing a number of scales and frequencies and by subsequent mode interactions (*transition*).

Together with this well-known TS path, *bypass transition* (path (E) in Figure 1.2) is also understood (Morkovin, 1985). If external disturbances are over 10 % of free-stream velocity or local perturbations with substantial magnitude are forced in the boundary-layer, the flow by-passes the TS mechanism and evolves rapidly to turbulence at subcritical Reynolds numbers.

Non-modal transient growth As mentioned above, the classical TS mechanism can be obtained only in a carefully controlled laboratory. In most practical flows, disturbances with moderate amplitudes are excited inside boundary-layers. Physically, they pull down higher momentum from the upper part of the boundary-layer and push up lower momentum from the lower part (*lift-up effect*). Landahl (1980) showed that an algebraic increase of streamwise perturbations occurs in a short time because of this lift-up mechanism. Afterwards, an exponential decay of the perturbations follows, which is called *transient growth* (Reshotko, 2001). This *non-modal* transient growth is expressed mathematically as a non-orthogonal growth between normal modes (Schmid, 2007).

Disturbances experiencing transient growth evolve in three different ways towards turbulence according to the magnitude of amplitudes. In the first case, path (B) in Figure 1.2, relatively small disturbances after a lower algebraic growth are advanced in modal eigenmode growth as a primary instability and then followed by secondary instability in order, as in path (A). In the second way (path (C)), finite amplitudes are formed in the transient growth with either external or local moderate perturbations. They attain a new quasi-steady flow and the secondary instability begins. Third, disturbances grow over a critical limit, then directly evolve into turbulent state through bypass mechanisms (Path (D)).

Optimal growth and disturbances In these paths, the case in which disturbances grow to the maximum before reaching bypass transition is called *optimal* transient growth. Initial upstream disturbances which accomplish the optimal growth are called optimal disturbances (Butler and Farrell, 1992; Luchini, 2000). Andersson et al. (1999) calculated the spatially optimal disturbances in boundary-layers and showed that steady counter-rotating vortices in streamwise direction with a spanwise wave number $\beta = 0.45$ yield the optimal initial disturbances. Here, the behavior of streamwise rotation is the most effective way to realize the lift-up mechanism.

Some experiments to study the transient growth have been conducted by means of free-stream turbulence (Matsubara and Alfredsson, 2001; Westin et al., 1994) and distributed surface roughness (Kendall, 1981; Reshotko and Leventhal, 1981). However, there are difficulties involved in obtaining the optimal disturbances in producing steady vortices and controlling a fixed spanwise wave length. To solve these problems, White (2002) tried to use an array of roughness elements. He showed stationary disturbances in the form of streamwise counter-rotating vortices on both left and right sides of the roughness elements and a transient growth of the disturbances with a controlled spanwise wave length. White and Ergin (2003) investigated the receptivity and transient growth of initial distur-

bances generated by various heights of roughness elements which are the most critical parameter to determine flow instability. Experiments have been performed for relatively low roughness-height Reynolds number $Re_h \leq 162$. These discovered that the streamwise disturbance energy in transient growth could be scaled by the squared Reynolds number based on the roughness-height Re_h^2 . Some other geometrical parameters are the ratios between height and boundary-layer thickness and the ratios between height and interval between the roughness elements (Choudhari and Fischer, 2005; Fransson et al., 2004; Joslin and Grosch, 1995). Piot et al. (2008) summarized several previous results for various roughness element shapes, and observed that structures of streamwise vortices also depend on the elements' shape. A nonlinear receptivity mechanism may also influence a generation of streamwise counter-rotating vortices either one pair or a pair on both spanwise sides (Tumin and Reshotko, 2004).

Suboptimality of roughness-induced disturbances The studies of White (2002) and Fransson et al. (2004) showed that transient growth initiated by roughness elements qualitatively agrees well with the non-modal growth theory, but quantitative comparisons are less consistent. Local disturbances generated by the roughness elements reach their maximum growth farther upstream at lower local wave number β than predicted by the optimal theory and accordingly decay earlier downstream. To find a physical reason for this suboptimal behavior, Fransson et al. (2004) calculated theoretically the optimal disturbance under the same conditions as their experiments and then compared the calculations with their experimental results by changing the wall-normal position of initial streamwise vorticity in the calculations. They found that, at a lower wall-normal position of streamwise vortices, a suboptimal growth very similar to that found in the experiments occurred. Moreover, the wall-normal position was remarkably close to the height of the roughness elements used in the experiment.

Here, we should keep in mind that the roughness elements induce not only

streamwise rotating vortices, which lead to transient growth, but also spanwise vorticity within the wall-normal shear layer. This layer behind the roughness element normally includes inflection-points on velocity profiles, which produce unstable perturbations in the wake zone and occasionally develop into a separation. According to Piot et al. (2008), a streaky layer behind a roughness element is induced on competition between the streamwise vortices and the wake effects, depending on the shape of the roughness elements. Hence, this wall-normal shear may influence the formation of the streamwise vortices in combination with spanwise vorticity and become a possible cause of suboptimality. Moreover, this wall-normal shear could be at the origin of bypass transition via vortex shedding (Rizzetta and Visbal, 2007) or hairpin vortices (Acarlar and Smith, 1987) in an over-critical case. However, Fransson et al. (2004) in their theoretical study mentioned above did not include spanwise vorticity for initial disturbance in the wake zone owing to difficulties in calculation. Hence, a detailed analysis of the flow and its stability in the vicinity of roughness elements and in the wake zone is needed.

1.2.2 Streamwise elongated streaks

Non-modal transient growth with moderate external and/or localized perturbations in boundary-layers typically appears as streamwise elongated streaks (Path (C) in Figure 1.2). In this subsection, previous studies of the generation of these streamwise streaks and their instability are introduced. In addition, flow stabilization effects based on these streaks are explained in order to set out the motivation of the present study.

Generation of streaks Several methods to induce transient growth and subsequently streamwise streaks in boundary-layers have been presented hitherto. First, Matsubara and Alfredsson (2001) performed experiments by means of moderate free-stream turbulence in a range $1 < Tu < 6$ %. Streaks were measured by

two-point hot-wire measurements and presented as a rapid decay of free-stream turbulence in high frequency ranges into disturbances with low frequencies in a boundary-layer. These disturbances grew linearly according to increasing displacement thickness Reynolds numbers. Such experimental results were also seen in a theoretical calculation by Luchini (2000) for optimal disturbance results. Second, Elofsson et al. (1999) used continuous suction at the wall with a constant wave number for generating stationary streaky structures in a channel flow. Several different amplitudes of streaks were obtained by varying the suction rates. Growth rates of the streaks increased linearly according to the amplitudes. Third, Fransson et al. (2004) attempted to generate streamwise high- and low-speed streaks using an array of cylindrical roughness elements in boundary-layers. As explained in the previous subsection, this method using roughness elements is the most appropriate method to induce optimal growth. Quasi-steady streamwise vortices were generated on both right and left sides of the roughness elements, and a sinusoidal base flow including streaks with controlled spanwise wave number was formed through the non-modal transient growth process. A formation of streamwise vortices, which are dependent on various geometrical parameters of roughness elements and their initial arrangement, consequently induces streaks further downstream. A DNS (Direct Numerical Simulation) study by Wörner (2004) investigated the flow field in the vicinity of a roughness element and showed a pair of counter-rotating inner and outer steady vortices around the roughness element. One high-speed and two low-speed streaks were then induced in each spanwise side. Fransson et al. (2004), White (2002), and Joslin and Grosch (1995) found a pair of high- and low-speed streaks on both sides further downstream.

Instability of streaks Based on a streaky base flow obtained by a DNS calculation with optimal disturbances input (Andersson et al., 1999), Andersson et al. (2001) investigated an inviscid secondary instability of the streaks based on a

linear Floquet expansion. They found the most dangerous sinuous mode, about 26 % amplitude of free-stream velocity, and a more stable varicose mode. Another study by Ricco et al. (2011) which induced the streaks by physically realizable free-stream disturbance rather than represented by an optimal disturbance, showed also that the sinuous mode is the most unstable. Vaughan and Zaki (2011) studied the secondary instability of a zero-pressure-gradient boundary-layer distorted by unsteady Klebanoff streaks, which leads to a lower critical streak amplitude than the steady streaks of Andersson et al. (2001). An interesting finding in their results is that, according to the amplitudes of the steady streaks, the most unstable mode is changed from the sinuous to the varicose mode. Breakdown of the streaks to turbulence was found in the study by Hack and Zaki (2014) which investigated the secondary instability of boundary layer streaks by means of direct stability analysis. They found that the streaks formed by the free-stream perturbations evolved into the sinuous mode as a most unstable mode. The breakdown is initiated by the amplification of localized instabilities of individual streaks after a wavy non-linear behavior calculated by a non-linear DNS. To induce the varicose mode, they used an adverse pressure boundary-layer with free-stream turbulence. In this case high-speed streaks were lifted over the low-speed streaks and a wall-normal inflection was formed. Breakdown of the streaks happened with a formation of Λ -vortical structures.

Flow stabilization by streaks Cossu and Brandt (2004) investigated the influences of streamwise streaks on stability of unstable TS waves by calculating perturbation kinetic energy. For perturbations, normal modes with the Floquet expansion corresponding to the spanwise periodical basic flow were applied. Evolution equations for the perturbation kinetic energy were divided into a viscous dissipation term and two production terms, which consist of Reynolds stresses associated with wall-normal and spanwise shear. Growth rates of the perturbations were determined by these terms. As a result, the negative perturbation energy

caused by spanwise shear contributed to reducing the energy growth rate of unstable TS waves. In other words, the stabilizing mechanism is explained by the fact that the spanwise velocity gradients of the streamwise elongated streaks disturb the streamwise development of the two-dimensional TS waves. They also showed that stronger amplitudes of streaks can stabilize the TS waves more effectively. This implies that the optimal transient growth is expected to maximize such an effect of flow stabilization.

Piot et al. (2008) studied the stability of a streaky boundary-layer using a bi-global stability approach. The streaky base flow was induced by a \cos^3 -shaped roughness element in a DNS calculation of Wörner (2004). They also found decaying growth rates of a streaky layer, including unstable TS waves. Experimental attempts were carried out by Fransson et al. (2005), using an array of cylindrical roughness elements. They showed a smaller amplification of TS wave than in a case without streaks. Moreover, the amplitudes of streaks grew proportional to the element's height, and amplification of TS waves was decayed more effectively, as predicted by Cossu and Brandt (2004). Accordingly, Fransson and Talamelli (2012) and Shahinfar et al. (2012) attempted a maximizing of the stabilization effect using vortex generators, which induce streaks with strong amplitudes while avoiding a high wall-normal shear to prevent bypass transition. In these ways, a passive flow stabilization method using roughness elements emerged.

1.3 Present contributions and overview

Aim Transient growth of localized disturbances generated by roughness elements has been investigated in various aspects as introduced in the previous section. Streamwise elongated streaks derived from the transient growth can stabilize the boundary-layer flow by delaying the laminar-turbulent transition. Thanks to its advantages of easier installation and a saving of operation energy in comparison with active methods, such a passive flow stabilization method has recently

received renewed attention. However, the roughness elements also play a role as obstacles in flows. High shear on the top of the roughness elements is a major factor in flow destabilization. Besides, the roughness elements initiate a complex combination of vortices in both a streamwise and spanwise direction, and their influences on a generating process of streaks, namely suboptimal transient growth, have also not yet been clearly understood. Secondary instability of such a streaky boundary-layer including *wake* effects of roughness element have not been assessed sufficiently hitherto.

Therefore, the purpose of the present study is to analyze the stability of a streaky boundary-layer induced by a roughness element. This streaky layer consists of strong velocity gradients in wall-normal *and* spanwise direction. A bi-global linear stability analysis is suitable for modal stability analysis of such a three-dimensional streaky layer in the wake zone (Theofilis, 2003). To date, not many experiments have been done parallel to theoretical and numerical efforts for analyzing the instability of the streaky layer. Contrary to a theoretical analysis, in which modal modes are calculated independently of each other, the simultaneous occurrence of modal modes and the interaction between them can be explored in experiments. Besides, the *linear* theory is not able to deal with nonlinear behavior. Modal modes grow based on larger amplitudes increased through transient growth, thus evolving easily into a secondary nonlinear state. Therefore, the present study consists mainly of experimental observations. Additionally, the nonlinear behavior of the streaks in the farther downstream region and the breakdown by an over-critical condition with a higher external velocity will be also considered.

At first, a CFD (Computational Fluid Mechanics) numerical calculation and experimental measurements by CTA (Constant Temperature Anemometer) and PIV (Particle Image Velocimetry) in the laminar water channel (LWK) were performed to explore the steady streaky boundary-layer flow. By observing the steady velocity and vorticity field in the vicinity of the roughness element and in the

wake zone, it is found that the streaky layer consists of a separation and high- and low-speed streaks and shows how the streaks are generated. Comparisons of experimental disturbances with numerical velocity gradients in both wall-normal and spanwise direction enable the major reasons for flow instability to be predicted. Additionally, a cross-validation between numerical and experimental results is accomplished. The bi-global modal stability analysis is implemented based on this steady streaky base flow. As a result, varicose and sinuous eigenmodes are identified and instability features of their eigenfunctions are analyzed. These theoretical results are confirmed by experimental measurements in which streamwise perturbations at each opposite side in the spanwise direction are acquired by two simultaneous hot-film probes in order to obtain each varicose and sinuous signal. As will be explained in Section 5, the varicose mode dominates the instability characteristics in the natural condition. To identify the sinuous signal is very difficult, owing to disturbances of the varicose mode and/or experimental noise. Therefore, an attempt is made to raise the sinuous mode by artificial forcing. In the last part of the present work, three-dimensional flow structures of nonlinear behaviour and breakdown of the streaks are observed by a hydrogen-bubble flow visualization.

Outline The present study is organized as follows. Fundamentals of linear stability theory, and a bi-global approach and its numerical method in the present work are presented in Chapter 2. In Chapter 3, the experimental setup is described. The laminar water channel (Section 3.1) and the shape of the roughness element and its installation in the test section (Section 3.2) are explained. In Section 3.3, several Reynolds numbers Re_h are tested, changing either the height of the roughness element or the external velocity to find a test flow condition. This is followed by a short introduction of flow measurement techniques (Section 3.4). Setup and operation of an external disturbance input to force a specific mode are presented in Section 3.5. Chapter 4 deals with features of the steady underlying

flow and a generation mechanism of a streaky layer by the roughness element. Chapter 5 presents the main results of the stability analysis. Section 5.1 shows eigenmode spectra, in which a grid convergence study and the streamwise evolution of unstable eigenmodes are examined. Eigenfunctions of relatively stable modes are also shown. Second, theoretical and experimental results of the modal stability analysis are presented and compared with one another in Section 5.2. Streamwise development and interactions between the two unstable modes are considered. This is followed by the preliminary results of forced mode (Section 5.3). Comparisons with unforced mode and some limitations of the current device for forcing asymmetrical disturbances are described. In Chapter 6, nonlinear motion of streaks is considered and breakdown is tested on an over-critical Reynolds number by a higher external velocity. Finally, the main results are summarized and conclusions are given in Chapter 7.

Chapter 2

Bi-global Linear Stability Theory

Analysis of flow instability has been considered in two ways. The first is by estimating a rate of change of perturbation energy and the second is by tracking small perturbations in time and space (Schmid and Henningson, 2000). The linear stability theory (LST) based on the second method has historically been well established and will be used in the present work for theoretical analysis. In this chapter, fundamentals of the classical local stability theory are summarized by referring both to Schlichting and Gersten (2000) and Kloker (2008) (Section 2.1). Thereafter, a bi-global approach for the analysis of a three-dimensional streaky layer and its numerical method are introduced in Section 2.2.

2.1 Linear stability theory

A starting point of the stability theory is to decompose the flow quantities into a basic stationary state \bar{u}_i and a small perturbation u'_i :

$$u_i = \bar{u}_i + u'_i. \quad (2.1)$$

It is assumed that this flow satisfies the Navier-Stokes equations. For a two-dimensional laminar boundary-layer, it could be assumed that changes in stream-

wise direction are much smaller than in the wall-normal direction, owing to a long enough streamwise distance compared with the boundary-layer thickness (*parallel-flow assumption*). Thus, the streamwise velocity component depends mainly on the wall-normal coordinate $\bar{u} = \bar{u}(y)$, and the other velocity components vanish $\bar{v} = \bar{w} = 0$. In addition, the perturbations are very small compared to the steady quantities; thus their production can be neglected (*linearization*). Accordingly, the Navier-Stokes equations for incompressible flow can be reformulated based on these assumptions into the linearized momentum equations:

$$\begin{aligned} \frac{\partial u'}{\partial t} + \bar{u} \frac{\partial u'}{\partial x} + v' \frac{d\bar{u}}{dy} &= -\frac{\partial p'}{\partial x} + \frac{1}{\text{Re}} \nabla^2 u' \\ \frac{\partial v'}{\partial t} + \bar{u} \frac{\partial v'}{\partial x} &= -\frac{\partial p'}{\partial y} + \frac{1}{\text{Re}} \nabla^2 v' \\ \frac{\partial w'}{\partial t} + \bar{u} \frac{\partial w'}{\partial x} &= -\frac{\partial p'}{\partial z} + \frac{1}{\text{Re}} \nabla^2 w'. \end{aligned} \quad (2.2)$$

Orr-Sommerfeld and Squire equation To solve the linearized equations (2.2) for two-dimensional laminar boundary-layers, the mathematical procedures set out below are needed. First, to eliminate the pressure terms in the equations, the pressure disturbance equations are obtained by taking the divergence of the linearized momentum equations and employing the continuity equation. These are then combined with the ∇^2 of the y -momentum equation. This results in an equation for the normal velocity component v' . Second, to describe the three-dimensional disturbances, wall-normal vorticity η' is combined with derivatives of the momentum equations. As a result, two equations are formulated for v' and η' . These small disturbances can be assumed as a wavelike form

$$\begin{aligned} v'(x, y, z, t) &= \hat{v}(y) e^{i(\alpha x + \beta z - \omega t)} \\ \eta'(x, y, z, t) &= \hat{\eta}(y) e^{i(\alpha x + \beta z - \omega t)} \end{aligned} \quad (2.3)$$

where α and β are the streamwise and spanwise complex wave number, respectively. ω is the complex angular frequency. \hat{v} and $\hat{\eta}$ are the amplitude across the shear layer. By applying these ansatzes into the equations, the linearized equations (2.2) can be finally rewritten as a 4th-order ordinary differential equation (ODE) eigenvalue problem, the so-called *Orr-Sommerfeld and Squire equation* as below,

$$\begin{aligned} \left[(-i\omega + i\alpha\bar{u})(\mathcal{D}^2 - k^2) - i\alpha\bar{u}'' - \frac{1}{\text{Re}}(\mathcal{D}^2 - k^2)^2 \right] \hat{v} &= 0 \\ \left[(-i\omega + i\alpha\bar{u}) - \frac{1}{\text{Re}}(\mathcal{D}^2 - k^2) \right] \hat{\eta} &= -i\beta\bar{u}'\hat{v} \end{aligned} \quad (2.4)$$

where, $k^2 = \alpha^2 + \beta^2$ and \mathcal{D} is a derivative operator. Primes denote y -derivatives. Boundary conditions at the wall and free-stream are $\hat{v} = \mathcal{D}\hat{v} = \hat{\eta} = 0$. The Orr-Sommerfeld equation for the Blasius boundary-layer was first solved by Tollmien (1929) and Schlichting (1933); hence, this solution was named Tollmien-Schlichting waves (TS waves).

To solve this eigenvalue problem, there are two strategies: temporal and spatial. Waves are periodic in the x - and z -direction for the temporal approach and in the t and z -direction for the spatial approach. Thus, α and β for temporal and ω and β for spatial case can be inserted as a constant real number. Each complex number ω for temporal and α for spatial analysis can now be calculated. The results of their imaginary part ω_i and α_i describe growth rates of perturbations and a point of neutral stability $\alpha_i = \omega_i = 0$ divides flow instability into a stable and an unstable state. Detailed results of eigenvalues and -functions containing various effects on the solutions are found in Schlichting and Gersten (2000).

A general property of the perturbation equation For an inviscid flow, viscous terms are omitted from the Orr-Sommerfeld equation (2.4) (*Rayleigh equation*). Many earlier studies of stability analysis dealt with inviscid flows because the equations are simpler and they enable some important analytical results to be

obtained. Rayleigh (1880) deduced that flows of which the velocity profile has an inflection point are unstable (*point of inflection criterion*). He proved that this is a necessary condition for the appearance of unstable waves, and Tollmien (1935) showed that the presence of an inflection point is a sufficient condition for an amplification of unstable perturbations. Physically, inflection points occur on velocity profiles where adverse pressure gradients exist, and they raise flow destabilization (*inviscid instability*).

Secondary instability As mentioned in Chapter 1, two-dimensional TS waves evolve into three-dimensional quasi-steady perturbation structures. The theoretical approach for secondary stability of such three-dimensional perturbations is performed in a similar manner to that for primary instability above. First, it is assumed that infinitesimal disturbances in primary instability are superimposed on a new approximately steady or quasi-steady basic state of periodic base flow. Here, three-dimensional infinitesimal disturbances u_i^* for the secondary instability are defined as

$$u_i^* = \phi_i^*(\xi, y) \cdot e^{i(\alpha^*z - \beta^*t)} \quad (2.5)$$

where α^* is the wave number of secondary perturbation. A new coordinate system based on a phase velocity of the TS wave c_{ph} ,

$$\xi = x - c_{ph}t \quad (2.6)$$

is applied for describing a new *steady* basic flow in a coordinate system (ξ, y, z) . To calculate these three-dimensional perturbations, the Floquet system (Herbert, 1988) is applied. According to a phase shift factor δ_r in a range $0 \leq \delta_r \leq 1/2$, instability is separated 0 for the harmonic and 1/2 for the subharmonic case. These theoretical results are described in detail in Herbert (1988). Experimental confirmations have been done by several researchers (Kachanov and Levchenko, 1984; Klebanoff et al., 1962) showing that harmonic (K-type) and subharmonic (H-

type) perturbations for secondary instabilities move downstream with the same velocity as the phase of TS waves.

Secondary instability for streamwise streaks As introduced in section 1, the inviscid secondary instability of the streamwise streaks was calculated by Andersson et al. (2001). They assumed that perturbation quantities consist of a single wave component in the streamwise direction.

$$p(x, y, z, t) = \text{Re} \left\{ \tilde{p}(y, z) e^{i\alpha(x-ct)} \right\} \quad (2.7)$$

where α is the streamwise wave number and c is the phase speed. Here, the Floquet exponent was also applied for presenting the secondary instability

$$\tilde{p}(y, z) = \sum_{k=-\infty}^{\infty} \hat{p}_k(y) e^{i(k+\gamma)\beta z}. \quad (2.8)$$

β is the spanwise wave number of the primary disturbance field. The detuning parameter γ of the Floquet system shows $\gamma = 0$ for a fundamental and $\gamma = 1/2$ for a subharmonic instability mode. These symmetries for even and odd mode in a spanwise direction make either a sine or cosine expansion. As a result, defined sinuous and varicose modes are formed in fundamental and subharmonic modes on the high- and low-speed streaks.

2.2 Bi-global approach

As seen above, the classical linear stability analysis for the shear flows based on 1D eigenfunctions has been theoretically well established in the last few decades. However, in the present study, the streaky layers induced by roughness elements consist of both streamwise streaks and high wall-normal shear with a separation, and the classical method is not suitable for such a complex three-dimensional underlying base flow. According to Cossu and Brandt (2004) who quantified the

kinetic perturbation energy of streaky boundary-layers on TS-like waves, each positive and negative production in terms of Reynolds stresses is associated with the wall-normal and spanwise shear of the streaky layer, respectively. Solutions of two-dimensional eigenvalue problems can describe the essentially non-parallel base flows which are inhomogeneous in two directions or periodic in the third spatial direction (Theofilis, 2003). Therefore, a bi-global LST is an appropriate method for the present study. Groskopf et al. (2008) examined the bi-global LST to analyze the stability of a supersonic boundary-layer with roughness elements depending on both directions of the velocity gradient, and showed a good agreement with unsteady DNS calculations. A brief introduction to a bi-global stability solver and numerical calculation procedures are given in this section and a more detailed description and examples can be found in Theofilis (2003) and Groskopf et al. (2008).

2.2.1 Governing equations and boundary conditions

The bi-global stability solver used in the present study is based on the three-dimensional Navier-Stokes equations with components which are normalized by a free-stream velocity u_e^* , reference length L^* , and density ρ^* , where $*$ means dimensional quantities. Non-dimensional time t and pressure p are defined as follows:

$$t = \frac{t^* u_e^*}{L^*}, \quad p = \frac{p^*}{\rho^* u_e^{*2}}. \quad (2.9)$$

The normalized components are decomposed into the steady primary state \mathbf{q}_0 which is a solution of the underlying flow equation and unsteady perturbing quantities \mathbf{q}' :

$$\mathbf{q}(x, y, z, t) = \mathbf{q}_0(x, y, z) + \mathbf{q}'(x, y, z, t). \quad (2.10)$$

In addition to that, the assumptions below are employed to formulate the equations for a linear stability analysis.

- A quasi-parallel assumption ($\frac{\partial}{\partial x} \equiv 0$) for steady base flow, i.e.

$$\mathbf{q}_0 = \mathbf{q}_0(y, z). \quad (2.11)$$

It should be mentioned that this assumption does not imply $v_0 \equiv 0$ for fully parallel flow like in the classical LST. Because this eliminates streamwise vortices on a two-dimensional spanwise (y, z) -plane, a less-severe restriction that only the mean value in spanwise periodic flows is zero ($\bar{v}_0 \equiv 0$) is set for the present study. Such a way, v_0 and w_0 for the streamwise streaks are retained, while v_0 for the Blasius flow is being disregarded.

- Perturbating quantities are small ($q' < 1$) and its production can be neglected ($q'_i \cdot q'_j \ll 1$) (*Linearization*).
- Perturbations can be thought to occur like waves and applied in the modal ansatz:

$$\mathbf{q}'(x, y, z, t) = \hat{\mathbf{q}}(y, z) \cdot e^{i(\alpha x - \omega t)} \quad (2.12)$$

where $\hat{\mathbf{q}}(y, z)$ is the amplitude distribution of perturbations. α and ω are the streamwise spatial wave number and the angular frequency, respectively, and both of them could be complex values.

Finally, the equations could be formulated to the generalized eigenvalue problem in temporal approach ($\alpha \in \mathbb{R}, \omega \in \mathbb{C}$):

$$\mathcal{A} \hat{\mathbf{q}} = \omega \mathcal{B} \hat{\mathbf{q}} \quad (2.13)$$

where, \mathcal{A} and \mathcal{B} are coefficient matrices. With a no slip condition at the bottom and the high enough y_{max} from maximum shear layer, the Dirichlet condition is applied at the bottom plate and top free-stream

$$\hat{\mathbf{q}}(0, z) = \hat{\mathbf{q}}(y_{max}, z) = 0. \quad (2.14)$$

Each left and right side in spanwise direction is supposed as a periodic wall.

2.2.2 Numerical method

For the base flow calculation The steady primary state q_0 was calculated by means of a CFD simulation (Herzog, 2013) with a laminar steady model in a three-dimensional computation domain in Figure 2.1. The commercial software *Star-CCM+* with *Gridgen* for grid generation were used. To reach a consistent Blasius flow input before the roughness element and to fully cover the flow influenced by a roughness element in downstream, the streamwise domain length extends from $x = 1.915 \sim 3.655 \text{ m}$. A stretch of the domain in y-direction is $y = 0 \sim 24 \cdot \delta_1$, where, δ_1 is the displacement thickness in the middle of the roughness element at $x = 2.35 \text{ m}$ in the case without roughness element. Although boundary conditions in the stability calculation are periodic, the half domain in spanwise direction $z = 0 \sim 3 \cdot d_R$ (d_R is the diameter of the roughness element) was calculated with a symmetry condition for saving computational cost. Because the spanwise computation domain $3 \cdot d_R$ is sufficiently large and the influences of the roughness element cannot reach the boundary wall, differences between these two conditions can be neglected. Configurations of the roughness element and all other flow conditions followed the experimental conditions identically (cf. Section 3).

For the stability analysis The generalized eigenvalue problem Equation (2.13) was solved by the implicitly restarted Arnoldi method (IRAM) implemented in the ARPACK routines (Lehoucq et al. (1998)) for such a huge size eigenvalue problem. Two-dimensional cross-cut slices of the steady state q_0 at different streamwise positions were extracted from the three-dimensional CFD calculation volume and interpolated by the cubic spline method onto the 2D stability analysis domains (See Figure 2.1). These stability planes were calculated independently at each selected streamwise position.

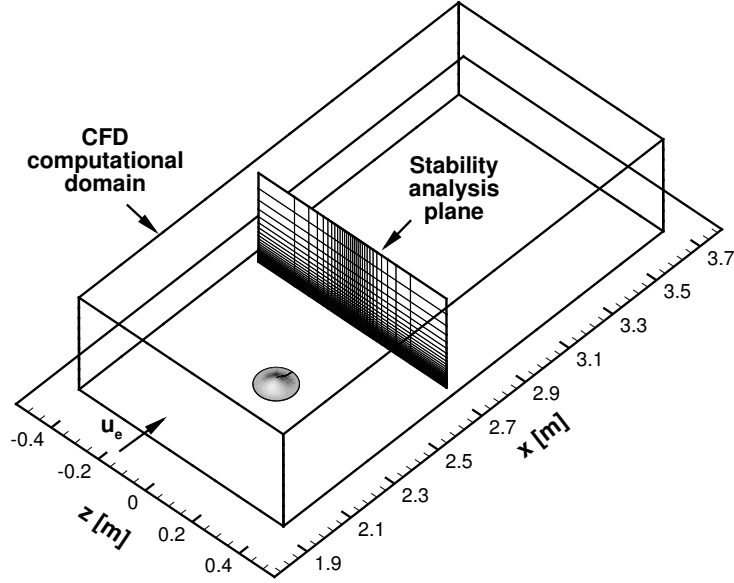


Figure 2.1: Computational volume domain for CFD calculation and 2D grid plane for stability analysis

Central finite-differences were used for the discretization of first and second derivatives on a Cartesian grid. A mesh refinement and stretching were implemented in both y - and z -direction to concentrate the grid nodes on the center of the roughness element where variables' quantities change remarkably. A method of Erlebacher and Hussaini (1991), which consists of two steps as described below, was used for the y -direction. First, an intermediate variable ψ is substituted for a computation domain $\eta \in [-1, 1]$ according to

$$\psi + t_\epsilon \tanh\left(\frac{\psi - \psi_0}{\Delta\psi}\right) = \frac{\eta - \eta_0}{\Delta\eta} \quad (2.15)$$

where the degree of influence of the hyperbolic tangent is set to $t_\epsilon = 1.2$. Second, the ψ is transformed into a physical domain $y \in [0, y_{max}]$ by

$$y = \frac{y_{1/2} y_{max} (1 + \psi)}{y_{max} - \psi (y_{max} - 2y_{1/2})}. \quad (2.16)$$

In this way, a half number of nodes could be collected within a length of twice the boundary-layer thickness ($y = 0 \sim 2 \cdot \delta_{99}$) by setting $y_{1/2} = 2 \cdot \delta_{99}$. $\Delta\psi$ and $\Delta\eta$

are related via

$$\Delta\psi = \left. \frac{d\psi}{dy} \right|_{y=y_0} \Delta y. \quad (2.17)$$

To aggregate densely towards the bottom wall and to widen the grid gradually in a normal direction, a focus point $y_0 = 0.0 \text{ m}$ is inserted with a concentration width $\Delta y_0 = y_{1/2}$. For a sufficiently large computation area, the end of the free-stream is set to $y_{max} = 20 \cdot \delta_{99}$ (not scaled in Figure 2.1). The detailed executing procedures can be found in Erlebacher and Hussaini (1991).

For the spanwise z -direction, a simple formula (Schmid and Henningson, 2000) such as

$$z = z_{max} \cdot \hat{z} \frac{\sqrt{\delta_z}}{\sqrt{1 + \delta_z - \hat{z}^2}}, \quad \hat{z} \in [-1, 1] \quad (2.18)$$

where a stretching factor $\delta_z = 0.1$ and spanwise range $z_{max} = 0.4 \text{ m}$ is used for a concentration of the grid in the middle of the roughness element at $z = 0.0 \text{ m}$ in a physical domain $z \in [-z_{max}, z_{max}]$ (cf. Figure 2.1).

Chapter 3

Experimental Setup

3.1 Laminar water channel

Measurements for experimental stability analysis were carried out in the laminar water channel (LWK, Laminarwasserkanal, Figure 3.1) at the Institut für Aerodynamik und Gasdynamik (IAG) of the University of Stuttgart. This facility was designed specifically for the study of instability of boundary-layer flows and their laminar-turbulent transition. For this purpose, the test section has a 10 *m* long streamwise distance with 1.2 *m* width and 0.5 *m* height; and this allows the whole process of natural transition from laminar to turbulence to be observed. An 8.0 *m* long glass flat plate with an elliptical leading edge (axial ratio 10:1) was installed in the test section and a height of 15 *cm* from the bottom of the flat plate to the free surface of water was maintained during all measurements. For a low turbulence intensity, the LWK has a three-dimensional contraction with a ratio 1 : 7.7 and three screens. Consequently, the streamwise turbulence intensity is less than 0.05 % in the frequency range 0.1 ~ 10 *Hz* at a free-stream velocity $u_e = 0.145 \text{ m/s}$ (Wiegand, 1996). Installation of the glass flat plate and a qualitative streamline test are described in Appendix B. An additional screen is positioned at the end of the flat plate (cf. Figure 3.9). This screen leads to a small pressure increase and imposes a zero pressure gradient on the whole plate, together with accurate control

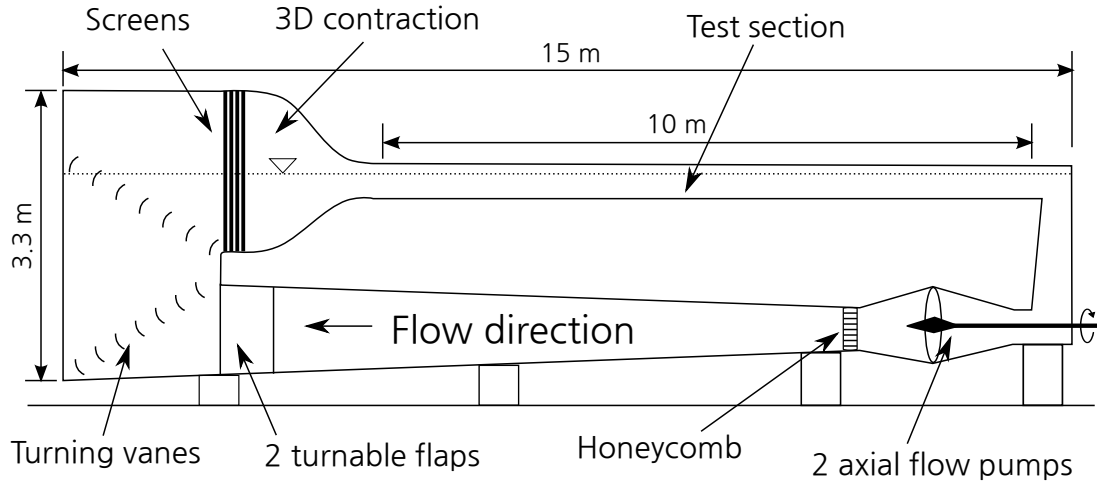


Figure 3.1: Schematic of the laminar water channel (LWK)

of the plate's angle. Moreover, a pressure difference between the upper and lower side of the plate forces a suction through a gap between the plate and the test section walls. This prevents the formation of an unstable corner boundary-layer flow. Good isolation of the LWK room having an air conditioner from the outside and a sandwich structure of the test section walls with thick wall glasses, keeps the change of water temperature in the test section below $0.05\text{ }^{\circ}\text{C}/\text{day}$ and minimizes thermal convection perturbations. More detailed technical improvements for stabilizing the flow in the LWK are introduced in Wiegand (1996).

Comparisons with wind tunnel In wind tunnel tests with small model inner boundary-layer flows, flow measurements and visualizations may be limited by a distinct size of instruments. For such cases, water channels are an appropriate substitute owing to the one order smaller magnitude of kinematic viscosity of water than air. For example, an experimental study by Fransson et al. (2004) in a wind tunnel used cylindrical roughness elements of height $h = 0.78\text{ mm}$ for a roughness-height Reynolds number $Re_h = hu_h/\nu = 340$, where u_h is the boundary-layer velocity at $y = h$ in the case without the roughness element, with a free-stream velocity $u_e = 8\text{ m/s}$. If the same Reynolds number is tested in a water channel with an assumption of the free-stream velocity $u_e = 0.08\text{ m/s}$ which is also a reference velocity in the present work, length scale about 6.7 times larger

is obtained,

$$\text{Re}_A \approx \text{Re}_W \quad \longrightarrow \quad \frac{L_W}{L_A} = \frac{u_A \nu_W}{u_W \nu_A} \approx 6.7 \quad (3.1)$$

where, subscript A and W denote air and water and L is a reference length. ν is the kinematic viscosity at 20 °C. This provides particular advantages in measurements and visualizations in the boundary-layers with such a small roughness element. However, it should be noted that about 667 times longer measurement time is required in the water channel under the same flow conditions,

$$\text{Sr}_A \approx \text{Sr}_W \quad \longrightarrow \quad \frac{f_W}{f_A} = \frac{L_A u_W}{L_W u_A} = \frac{\nu_A u_W^2}{\nu_W u_A^2} \approx 0.0015 \quad (3.2)$$

where, Sr is the Strouhal number and f is the frequency.

Spanwise non-uniformity Streamwise elongated high- and low-speed streaks are described as periodical velocity changes in the spanwise direction; hence, a uniform velocity distribution in the boundary-layer is a prerequisite before reaching the roughness element for avoiding any ambiguities in the streaks generated by the roughness element. However, as seen in Figure 3.2 (a), a spanwise velocity distribution with the maximum amplitude of disturbances of 1.75 % of the free-stream velocity at $z = 0.12 \text{ m}$ existed in the LWK. This may have been caused by both LWK's own properties and debased screens in the contraction. To regulate this variation, an additional screen was installed at the end of the contraction (Figure 3.2 (b)), with the result; that the variation of spanwise velocity distribution was reduced to under $\pm 2 \%$ of u_e in Figure 3.2 (a) and the maximum amplitude of disturbances was 0.7 %. Furthermore, the inclined velocity distribution in the spanwise direction is recovered in the downstream direction (*dashed lines* in Figure 3.3). The velocity variation does not exceed $\pm 2 \%$ at all streamwise positions. The amplitudes of disturbances are also maintained at a low value, except near the test wall side at about $z = -0.2 \text{ m}$ at the streamwise position $x = 1.7 \text{ m}$. The influence of the spanwise non-uniformity on the stability of boundary-layer

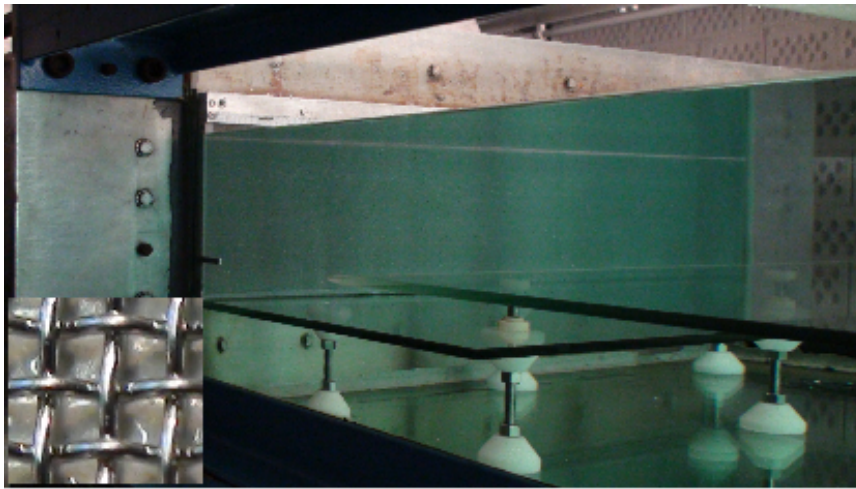
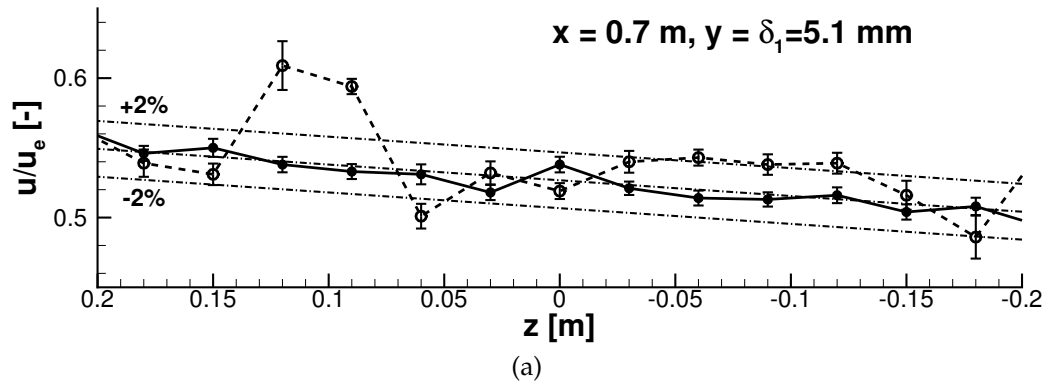


Figure 3.2: (a) Velocity distribution in spanwise direction without (*dashed line*) and with (*solid line*) the screen. *Error bars* describe *rms*-amplitudes of disturbances (b) Installation of a screen of stainless steel mesh with a wire diameter $d = 0.24 \text{ mm}$ and wire spacing $M = 0.63 \text{ mm}$ at the end of contraction

is proven to be less remarkable.

3.2 Roughness element

As discussed in Chapter 1, both transient growth of local disturbances generated by a roughness element and the appearance of a streaky layer behind the roughness element are formed, depending on the shape and height of the roughness element. According to the goal of the present analysis of the stability of a laminar streaky layer, the shape and height were designed to induce streamwise streaks that were as strong as possible, while avoiding a bypass transition. For

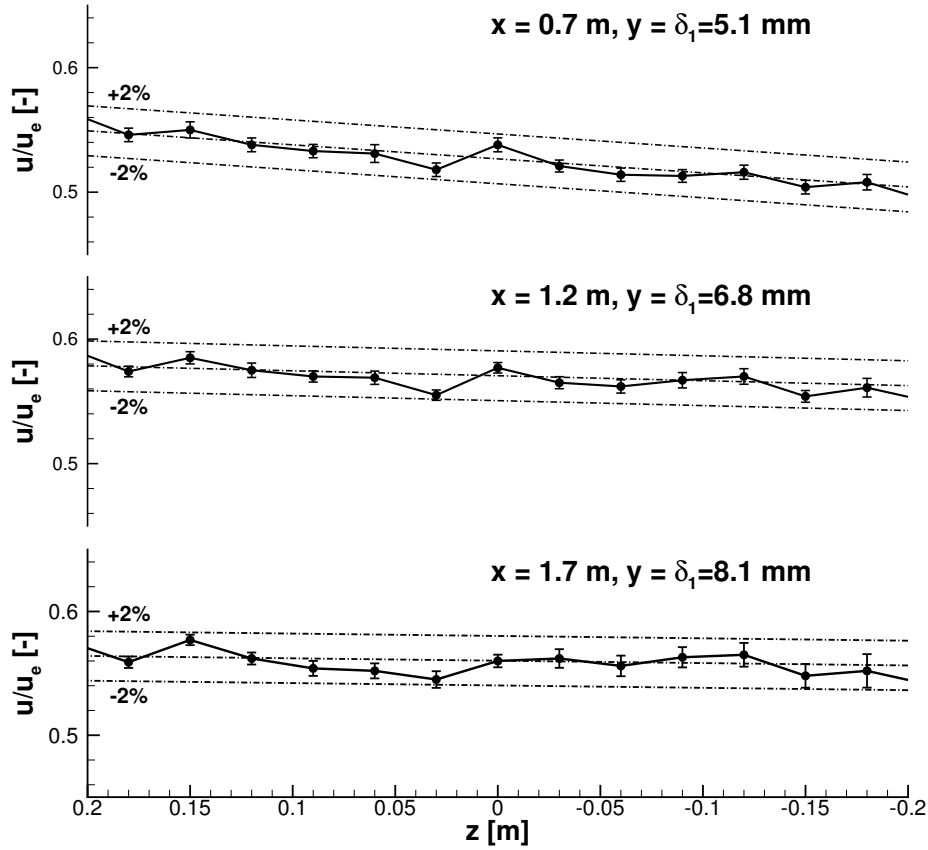


Figure 3.3: Streamwise evolution of velocity distribution in spanwise direction. Error bars describe *rms*-amplitudes of disturbances

these reasons, a smoothly curved \cos^3 -shaped roughness element was selected for obtaining relatively large streamwise vortices in comparison with separation that is induced just behind the roughness element.

$$y(x, z) = h \cos^3 \left(\frac{\pi r}{d_R} \right), \quad 0 \leq r = \sqrt{x^2 + z^2} \leq d_R/2 \quad (3.3)$$

where the diameter of the roughness element is $d_R = 0.145 \text{ m}$ and its height is $h = 0.89 \cdot \delta_1 = 8.3 \text{ mm}$ (cf. Section 3.3). δ_1 is the displacement thickness in the case without the roughness element at $x_R = 2.35 \text{ m}$, where x_R is the streamwise position of the roughness element from the leading edge (cf. Figure 3.9). A mathematical illustration of the shape and an experimental model made of plexiglas are shown in Figure 3.4 (a) and (b), respectively.

The experimental model was installed in the spanwise middle of the flat plate.

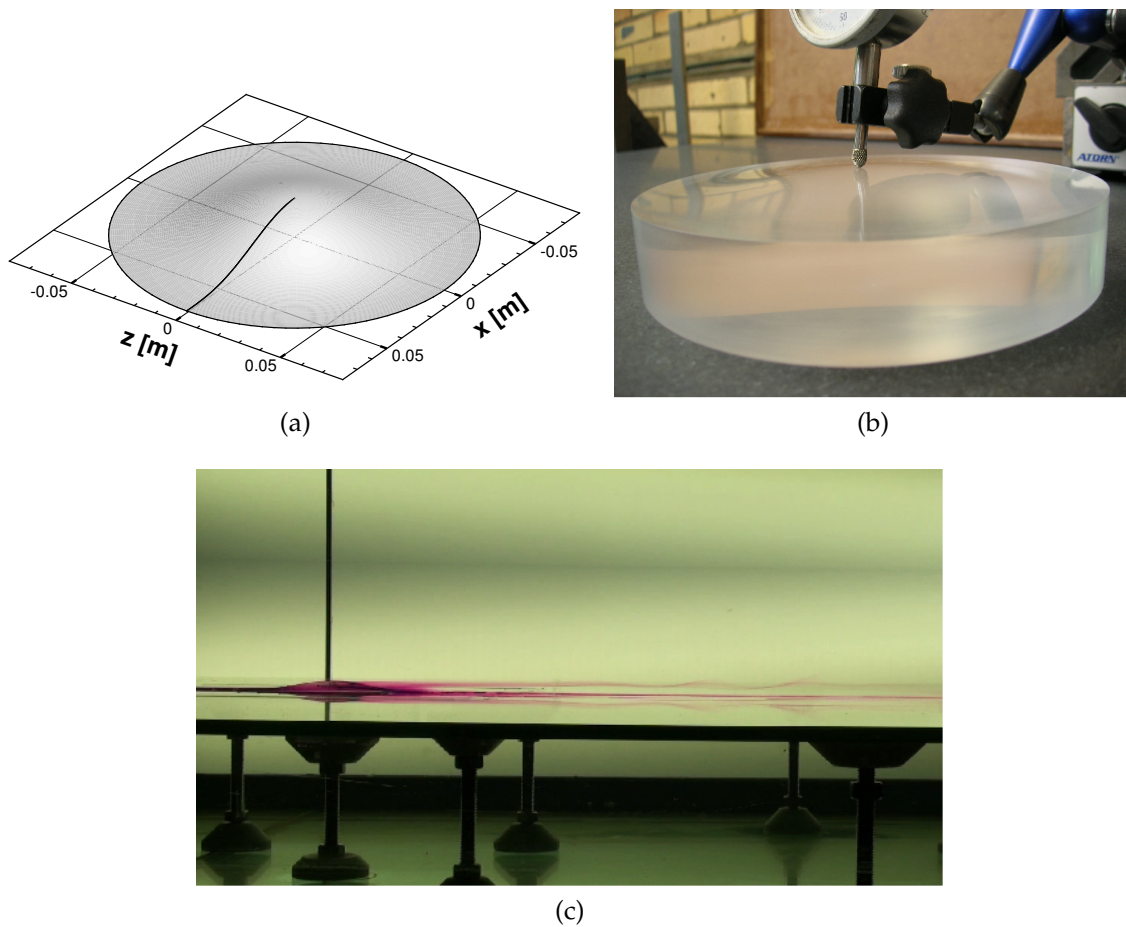


Figure 3.4: (a) Mathematical and (b) experimental roughness element model (c) Installation of the model in the test section and visualization of the wake flow by potassium permanganate crystal

As seen in Figure 3.4 (c) and 3.6, the experimental model was placed by a support under the model, and splits between the roughness element and the flat plate were sealed by silicon and covered by a tape with a 0.05 mm height (cf. Figure B.1 (b) in Appendix B). Accordingly, there were no steps and splits that could disturb the flow around the roughness element. In fact, an array of roughness elements is considered in the CFD simulation with a periodical boundary condition. However, only a single roughness element has been installed for the experiments, owing to the limited width of the test section. The spanwise wave length $\beta = 6 \cdot d_R$ of the computational domain is large enough in consideration of very weak spanwise spreading of streamwise streaks. Thus, discrepancies between numerics and experiments can be neglected.

3.3 Flow condition

Flow phenomena are normally characterized by the non-dimensional Reynolds number, and the flow in the present study, which is provoked by a roughness element, is specified by the roughness-height Reynolds number Re_h . As seen in the previous section, Re_h consists of the boundary-layer velocity and the height of the roughness element, as well as the kinematic viscosity. Hence, Re_h can be controlled by changing the free-stream velocity and the height of the roughness element. In this section, several Reynolds numbers obtained by changing these two parameters are explored by flow visualization, and a test case is selected for the present study, in which the streamwise streaks are growing as large as possible, while avoiding bypass transition.

Hydrogen-bubble method The streaky flow behind the roughness element was visualized by the hydrogen-bubble method. The principle of this method is to visualize the flow by illuminating successively generated timelines by hydrogen bubbles created by electrolysis. If a DC voltage is applied between two electrodes in water working as an electrolyte itself, hydrogen bubbles arise on the cathode (tungsten, $\varnothing 30 \mu m$) and conduct themselves as tracer particles in the flow. As an anode, a copper rod was used. The experimental setup is illustrated in Figure 3.5. These bubbles are visualized by the light sheet of a DPSS (diode-pumped solid-state) laser. The laser light sheet rays in a spanwise direction and illuminates a two-dimensional (x, z) -plane. For observation in different heights, laser and camera move up and down by the same distance, so that all pictures always have the same length scale. The high- and low-speed streaks are essentially a spanwise velocity variation, and this can be observed by the timelines. For an occurrence of the timelines in the (x, z) -plane, a pulse duration of 2.0 ms and a pulse interval of 200.0 ms with a voltage of 1000 V were entered into a pulse generator. To observe three-dimensional flow structures, for example the case in Figure 3.7 (c), a bubble

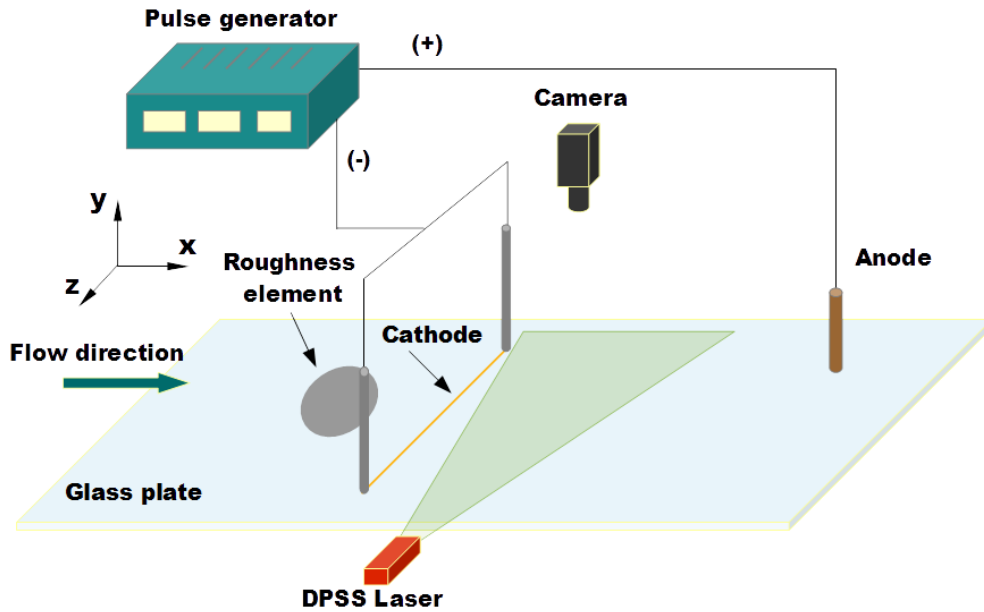


Figure 3.5: Experimental setup for flow visualization by the hydrogen-bubble method

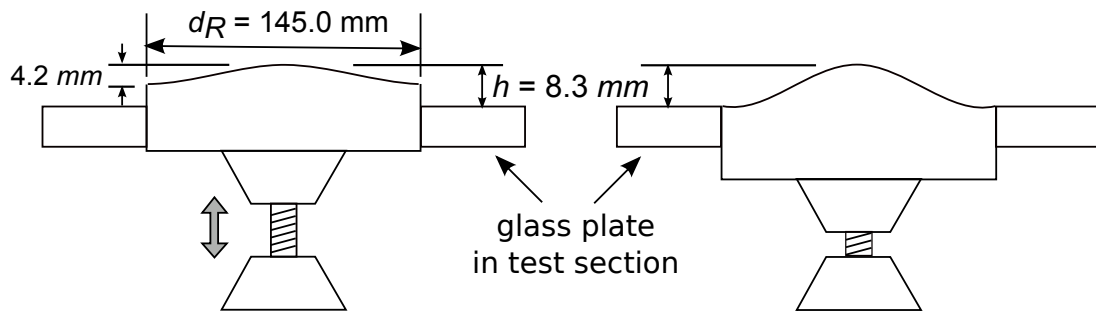
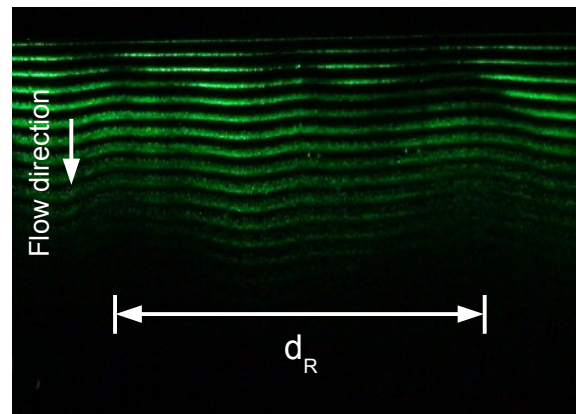


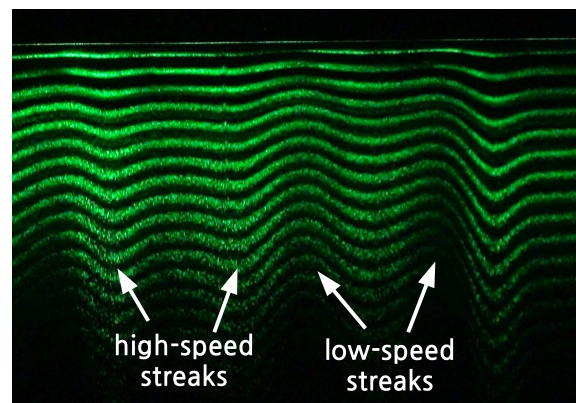
Figure 3.6: Schematic of roughness element on a support for changing in various heights (left side) and a fixed model in a height of roughness element $h = 8.3 \text{ mm}$ (right side)

carpet was introduced with a pulse duration 1.0 ms and a pulse interval 0.0 ms with a voltage 70 V and illuminated by a halogen lamp.

Changing the height of the roughness element The height of the roughness elements is a fundamental parameter determining the instability of streaky boundary-layer flows induced by roughness elements. To find an appropriate height of the roughness element, three different heights were tested with a fixed free-stream velocity $u_e = 0.1 \text{ m/s}$. The height can be changed by a support under the experimental model, as in Figure 3.6. The element has an upper roughness part



(a)



(b)



(c)

Figure 3.7: Flow visualization for three different heights (a) height of the element $h = 4.2 \text{ mm}$, cathode wire at $x_c = 2.6 \text{ m}$, $y_c = 4.0 \text{ mm}$ (b) $h = 8.3 \text{ mm}$, $x_c = 2.65 \text{ m}$, $y_c = 6.0 \text{ mm}$ (c) $h = 12.5 \text{ mm}$, $x_c = 2.6 \text{ m}$, $y_c = 10.0 \text{ mm}$ and camera position $x = 2.8 \text{ m}$

of a height $h = 0.5 \cdot \delta_1 \approx 4.2 \text{ mm}$ (cf. left side in Fig. 3.6), where δ_1 is the displacement thickness at $x = 2.35 \text{ m}$ in the case without the roughness element with a free-stream velocity $u_e = 0.1 \text{ m/s}$.

Figure 3.7 shows the results of flow visualization by timelines (Figure 3.7 (a) and (b)) and bubble carpet ((c)). The cathode wire is positioned at $x_c = 2.6$ and 2.65 m, respectively, where the maximum growth of the streaks' amplitudes was predicted. With the height $h = 4.2$ mm in Figure 3.7 (a), a minimal velocity variation in spanwise direction is observed, but the streamwise streaks are unidentifiable. The high- and low-speed streaks are seen clearly in the case with the height $h = 8.3$ mm in Figure 3.7 (b). Behind the roughness element (center of the figure), a low-speed streak arises and high-speed streaks locate on each left and right side. Additionally, as the experimental model rises up, the cylindrical part of the model is disclosed in the flow, which also induces high- and low-speed streaks outside. These outside streaks are also seen as a continuous line in Figure 3.7 (c). In the case of a higher height $h = 12.5$ mm, hairpin vortices followed by a breakdown to turbulence were observed. From these results, the height of the roughness element $h = 8.3$ mm was selected and a new experimental model with that height was manufactured (cf. right side in Figure 3.7) and installed in the test section for the whole measurements.

Changing free-stream velocity Another important parameter in the flow instability by roughness elements is the boundary-layer velocity. Thus, a parametric test was done by adjusting four different free-stream velocities. The first result with the lowest velocity $u_e = 0.045$ m/s in Figure 3.8 (a) shows very weak high- and low-speed streaks. As the velocity increases to $u_e = 0.06$ and 0.08 m/s, the streaks are seen more clearly, as in Figure 3.8 (b) and (c). The timelines of low-speed streak in the middle become increasingly dense, in contrast to the widening gap between the timelines of outer high-speed streaks. This means that both the wake behind the roughness element and the streamwise rotating vortices concurrently occur more intensively along with a velocity increase, and, as a result, larger amplitudes of the high- and low-speed streaks are induced. In the case with the highest velocity $u_e = 1.0$ m/s, the time lines are

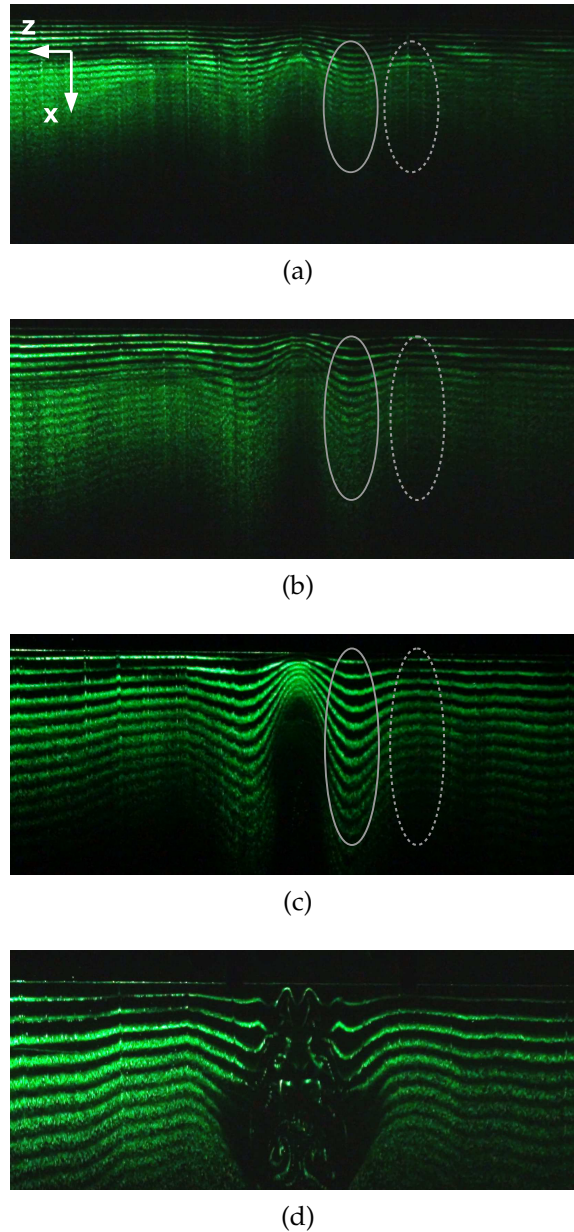


Figure 3.8: High- (*solid*) and low- (*dashed ellipse*) speed streaks for four different free-stream velocities (a) $u_e = 0.045 \text{ m/s}$ (b) $u_e = 0.06 \text{ m/s}$ (c) $u_e = 0.08 \text{ m/s}$ (d) $u_e = 0.1 \text{ m/s}$. Timelines begin at $x_c = 2.6 \text{ m}$, $y_c = h = 8.3 \text{ mm}$

broken in the middle, as seen in Figure 3.8 (d). Because the laser sheet illuminates only a two-dimensional plane, three-dimensional vortical structures cannot be pictured in Figure 3.8 (d). Spanwise expansion of the chaotic motion was observed, although not visible in this figure. In conclusion, the free-stream velocity $u_e = 0.08 \text{ m/s}$ with the height of the roughness element $h = 8.3 \text{ mm}$ corresponding to a Reynolds number $Re_h = hu_h/\nu = 329$ is selected for the present

study. This roughness-height Reynolds number is a little smaller than the critical Reynolds number, according to Klebanoff et al. (1962). A streamwise Reynolds number $Re_x = x_R u_e / \nu = 1.88 \times 10^5$ is calculated where the roughness element is located.

3.4 Measurement techniques

For an analysis of flow instability of the streaky layer, accurate measurements of disturbances generated locally by the roughness element are of importance. These disturbances are characterized by a periodic shedding originating from an unstable shear layer on the top of the roughness element and by quasi-steady streamwise rotating vortices on both sides of the roughness element. To analyze these two different types of disturbances and their complex mixing downstream, both a sensitive response to small changes in a short time and temporally continuous measurements in a time period for spectral investigations are needed. The Constant-Temperature-Anemometry (CTA) method with hot-film probes satisfies these requirements.

However, the hot-film probe itself is an obstacle disturbing the flow field and cannot measure negative velocity components of, for example, a separation behind the roughness element. Particle-Image-Velocimetry (PIV), which is a non-intrusive optical measurement technique using a laser illumination, can solve these problems. Moreover, results of PIV measurements give a highly resolved spatial observation (a whole-flow-field technique) and can be compared intuitively with numerical simulations.

Therefore, the CTA method was mainly used to measure velocities and disturbances at several selected streamwise positions. A simple positioning of the hot-film probes in the test section by a traversing system enables a long downstream range to be covered. PIV measurements were accessorially performed to measure and visualize the flow and separation in the wake near the roughness

element. The PIV method was also used to catch a non-linear motion of three-dimensional vortex structures in the last part of the present study (Chapter 6). Several major components for the CTA and PIV measurement system and some features at the LWK will be introduced in this section. Fundamentals and general operating instructions are described in Bruun (1995) for CTA and in Raffel et al. (2007) for PIV measurements.

3.4.1 Constant temperature anemometry

The CTA method is a thermal technique measuring temperature changes on heated sensor by flows. The sensor of the hot-film probe is made of a nickel-fiber-film coated by quartz that allows to operate in water (Dantec, 2005). Sensor heating and maintaining constantly on an over-heated temperature against cooling by flows are done by a CTA bridge from which temporally continuous signals are generated. The electronical signals acquired by a A/D converter are transformed into velocities by a calibration curve. Appendix C describes in detail the technical procedure to setup the CTA measuring system and calibrating it for getting the calibration curve. Technical data and experimental parameters are summarised in Table 3.1.

Signal conditioning and acquisition For measurements of the small disturbances in a high resolution, an analog low-pass filter (IMD EST 1BU T4) of $f_{g,LP} = 5 \text{ Hz}$ was set to eliminate the noise in the high frequency area, and then the DC part of the signal was separated by a high-pass filter with a cut-off frequency $f_{g,HP} = 0.1 \text{ Hz}$ (cf. flow chart in Figure 3.9). The AC signal was amplified by an amplifier (IMD DMC-45-R) 100 times for natural cases and 50 times for the forcing cases with external disturbance input. Consequently, the signals were acquired by a 16-bit A/D converter (NI USB-6216 BNC). To minimize the

influences of the cut-off frequency of the high-pass filter, a settling time

$$\tau = \frac{10}{f_{g,HP}} = 100 \text{ s} \quad (3.4)$$

had been employed after every moving of the probe by the traversing mechanism. With these parameters, a sufficiently low cut-off frequency can be set while preventing an excessive measurement time.

A fast Fourier transform (FFT) had been carried out for spectral analysis of the measured time signal. A spectral resolution $\Delta f = f_{min} = 0.01 \text{ Hz}$ was selected and the corresponding measuring duration is

$$T = \frac{1}{\Delta f} = 100 \text{ s}. \quad (3.5)$$

For an efficient signal sampling and transforming, the maximum frequency (*Nyquist frequency*) is determined as $f_{max} = f_{Ny} = 5.12 \text{ Hz}$, according to this the sampling

Table 3.1: Technical data and experimental parameters for the CTA system

Hot-film anemometry	Bridge	Dantec 56C17 DISA55M10	
	Probe	Dantec 55R15 boundary-layer type	
	Sensor	Nickel-fiber, $\varnothing 70 \mu m$ with $2 \mu m$ quartz coating	
	Warm-up time	T_{wu}	2 h
	Overheat ratio	a	5 %
Signal conditioning	Low-pass filter	$f_{g,LP}$	5.0 Hz
	High-pass filter	$f_{g,HP}$	0.1 Hz
	Settling time	τ	100 s
	Amplifier factor	V	50 ~ 150
Data acquisition	Duration	T	100 s
	Points	N	1024 pts
	Sampling rate	f_s	10.24 Hz

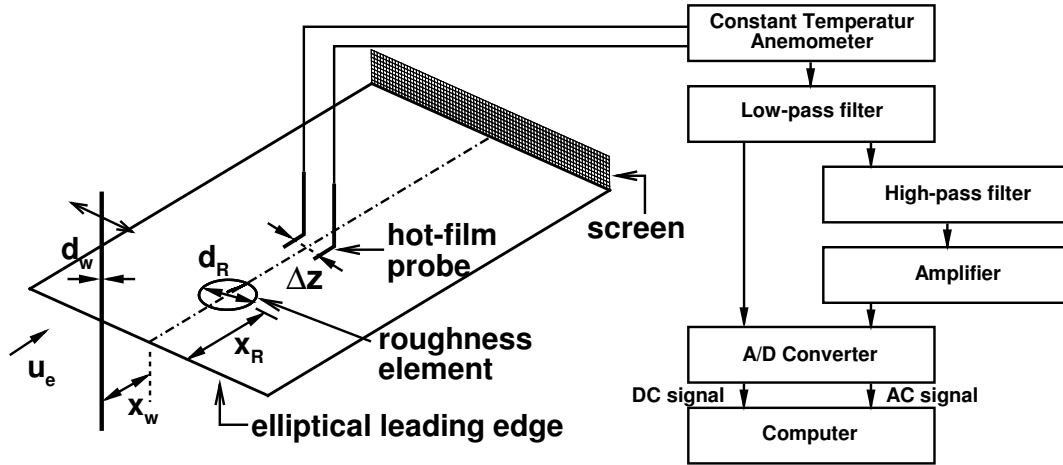


Figure 3.9: Schematic of experimental setup and flow chart of analog signal processing. Swing wire for external disturbance input locates in front of the leading edge

rate and the number of data points are

$$f_s = 2 \cdot f_{Ny} = 10.24 \text{ Hz} \quad (3.6)$$

$$N = 2 \cdot f_s T = 1024 \text{ pts.} \quad (3.7)$$

A settling time of 100 s was also inserted for every measurement. All parameters above are summarized in Table 3.1.

Varicose and sinuous signal As will be explained in Chapter 5, the two most unstable eigenfunctions obtained by the bi-global LST behave themselves symmetrically and asymmetrically in respect to spanwise coordinate, so named *varicose* and *sinuous*, respectively. To find these eigenmode experimentally, two hot-film probes connected with two different bridges were located on opposite sides equidistantly in spanwise direction relative to the centre (cf. Figure 3.9) and acquired signals simultaneously. The measured disturbances were separated into their varicose and sinuous component by

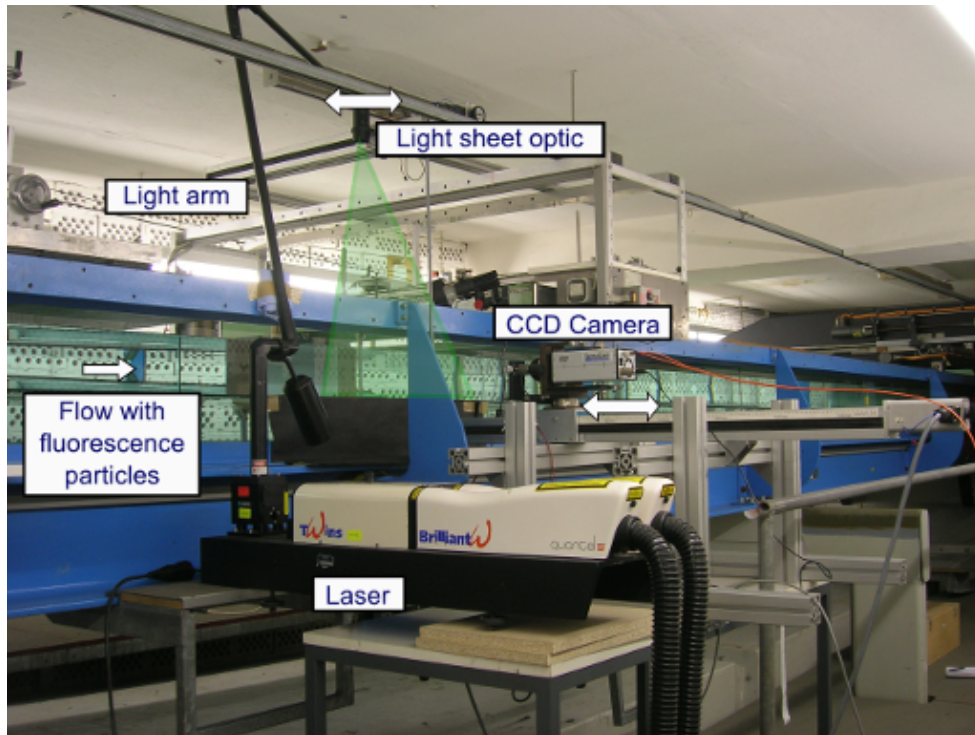
$$u'_{vari} = \frac{u'_1 + u'_2}{2}, \quad u'_{sinu} = \frac{u'_1 - u'_2}{2} \quad (3.8)$$

where u'_1 and u'_2 are the streamwise perturbation components from respective probe. Positions of the probes were $z = \pm 0.0095 \text{ m}$ in spanwise direction, where the amplitude of the sinuous eigenmode is maximal (cf. Section 5.2). To illustrate the experimental mode shape on a two-dimensional (y, z) -plane (cf. Figure 5.9), additional measurements in five spanwise positions $z = \pm 0.0, 0.0045, 0.0095, 0.02, 0.035 \text{ m}$ were done at $x = 2.7 \text{ m}$ by changing the distance Δz between the probes.

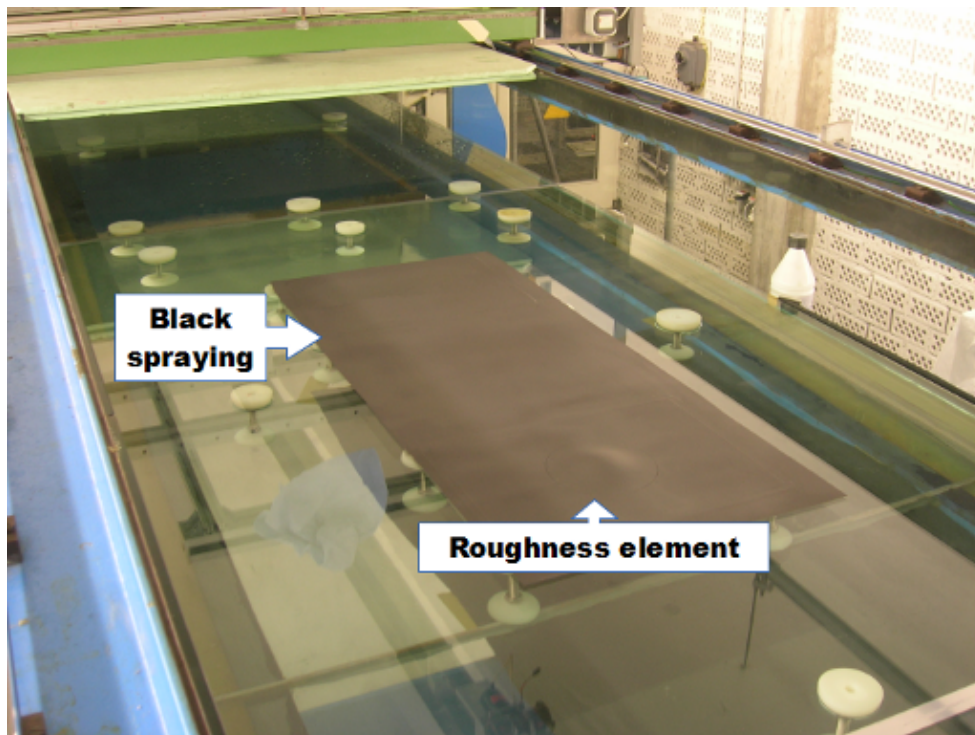
3.4.2 Particle image velocimetry

Figure 3.10 (a) shows the installation of the mono-PIV measurement system at the LWK. Fluorescence particles (Toray SP-500) seeded in the flow are illuminated by a dual pulsed Nd:YAG Laser (Quantel, Brillant Twins). The pulsed laser beams are introduced by a light-guiding arm and widened by the light sheet optics perpendicular to the flat plate (green triangle in Figure 3.10 (a)). A time-interval between the two pulsed laser lights $\Delta t = 8.0 \text{ ms}$ was selected for the free-stream velocity $u_e = 0.08 \text{ m/s}$ by which an averaged particle-offset of ca. 8 px between two scattered light pictures was obtained (cf. Raffel et al. (2007)). The scattered light was pictured by a so-called cross-correlation CCD camera (PCO SensiCam) with a zoom objective (Nikkor $f = 50 \text{ mm}$) and sent to a PC through an optical fiber. All independent components of the PIV-system above had been synchronized by a sequencer of the German Aerospace Center (DLR, Deutsches Zentrum für Luft- und Raumfahrt) generating a programmable TTL (Transistor-to-Transistor Logic) pulse train. Finally, the velocity field was obtained by calculations of cross-correlation between the first ($32 \times 32 \text{ px}$) and second ($64 \times 64 \text{ px}$) interrogation window of the scattered light pictures. Detailed technical data of the devices are summarized in Appendix A.

Reflection and refraction of light Difficulties of PIV measurements, as an optical measurement method, especially at the LWK, occurred owing to the reflection and refraction of the laser light. First, unwanted reflection on the glass wall



(a)



(b)

Figure 3.10: (a) Experimental setup of 2D mono-PIV system at the LWK (b) Black spraying on the roughness element and the glass plate area illuminated by the laser

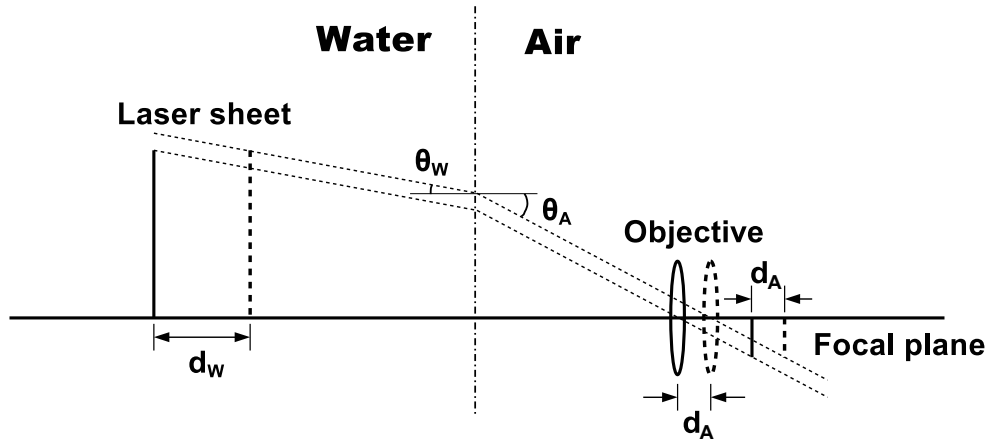


Figure 3.11: Refraction of light beam at the boundary between water and air. d_W , d_A : spanwise moving length of laser sheet plane and focal plane of objective, respectively θ_W , θ_A : angle of refraction (indices W and A indicate water and air, respectively)

and the roughness element model made of plexiglas hides the light scattered by the particles. To prevent this, the measurement section of the glass plate and the roughness element were painted black, as shown in Figure 3.10 (b). Second, when the light penetrates from water into air, a refraction of the light beam at the boundary between water and air occurs, owing to different phase velocities of light in air and water, as seen in Figure 3.11. To depict an equal length scale on the focal plane of objectives, a moving distance of the CCD-camera must be corrected by a ratio to Snell's law

$$\frac{d_W}{d_A} \approx \frac{\sin\theta_W}{\sin\theta_A} = \frac{n_A}{n_W} = \frac{1}{1.33} \quad (3.9)$$

where n_A and n_W are refraction indices of air and water, respectively. For instance, if a light sheet plane moves 10 cm in the spanwise direction, the CCD-camera must be shifted 7.52 cm. For spanwise scanning of the flow field, the light sheet optics and the CCD-camera are arranged on two separate traversing mechanisms.

3.5 Asymmetrical external forcing

As will be shown in Chapter 5, two distinguished unstable varicose and sinuous eigenmodes are identified in a laminar streaky layer induced by the roughness element. The experimental amplitudes of the varicose mode are quite larger than the sinuous ones and it seemed that the smaller sinuous amplitudes are somehow hidden by either the dominant varicose mode or a lower signal-to-noise ratio. For this reason, an amplification of the sinuous mode had been attempted by forcing initial asymmetric amplitudes in the free-stream.

In fact, a symmetric forcing is comparatively easy. Classical forcing technique using a vibrating ribbon stretched in spanwise direction within the boundary-layer (Klebanoff et al. (1962); Lang et al. (2004)) excites TS- and shear layer instabilities in the high shear layer above and behind the roughness element, such that the varicose mode would gain in amplitude and periodicity. On the contrary, an asymmetrical forcing is much more challenging. In practice, there has been no simple method for asymmetric forcing in the wake of the roughness element up to now. Pulsed jets directly through the wall can force asymmetry in flows, but these might have detrimental side effects because they are injecting mass. For these reasons, a method using a vertical single wire operating by a computer controlled traversing system was carried out in the present work. As will be seen in Section 5.3, this method is also very difficult to perfectly accomplish in practice. So, these results should be considered just preliminary and interpreted cautiously. Nevertheless, checking out predictable problems would be valuable to pursue such further investigations for developing a new exact method to elaborate measurements.

As sketched in Figure 3.9, a thin wire of diameter $d_w = 1.0 \text{ mm}$ was placed upstream of the plate's leading edge in a distance $x_w = 0.012 \text{ m}$. The upper end of the wire was fixed to a traversing device and traversed back and forth in spanwise direction, by which a sinuous perturbation with respect to the spanwise centre

was introduced. As the lower end was let free, this might generate uncontrolled chaotic disturbances. However, these disturbances flow underneath the plate, therefore, no influences are ingested into the boundary-layer above the plate. A periodic frequency of 0.225 Hz which is close to the theoretical frequency of the sinuous mode at $x = 2.7 \text{ m}$ (angular frequency $\omega_r = 16.7$ in Figure 5.3 (b)) had been imposed. The wire had been translated in a range $z = -0.0095 \sim 0.0095 \text{ m}$ which is the interval between the two hot-film probes (cf. Figure 3.9). Triggering signals were generated when the wire reaches the end of the spanwise position $z = -0.0095 \text{ m}$ and signal acquisition of the probe was started by these signals. A waiting time after every start of the wire translation was set $t = 100 \text{ s}$, so that forced disturbances can reach up to the maximum measurement position $x_{max} = 3.1 \text{ m}$. The measuring duration and settling time as well as all the other parameters for the measurements were set identical to the natural case without external forcing.

Chapter 4

Streaky Boundary-layer Flow

This chapter deals with the steady streaky boundary-layer induced by the \cos^3 -shaped roughness element. This includes two major flow phenomena: a separation behind the roughness element and streamwise elongated high- and low-speed streaks. These flow features are separately analyzed by the streamwise velocity distributions in both wall-normal and spanwise direction and by the velocity gradients. The numerically calculated gradients are compared with experimental unsteady disturbances in terms of flow instability.

The comparison of numerical and experimental velocity distributions in both y - and z - direction show a good agreement between them. Particularly, fast changing shear inflection of velocity profiles and their gradual recovery in a downstream direction are well described. From that, an acceptability of the experimental setup and a validation of the numerical results are achieved.

4.1 Wall-normal shear and separation

Figure 4.1 shows experimental and numerical velocities in the vicinity of the roughness element. In front of the roughness elements, the flow goes smoothly over the roughness element without any stagnation (Figure 4.1 (a)). On the back side, streamwise velocities are reduced by an adverse pressure gradient. Finally,

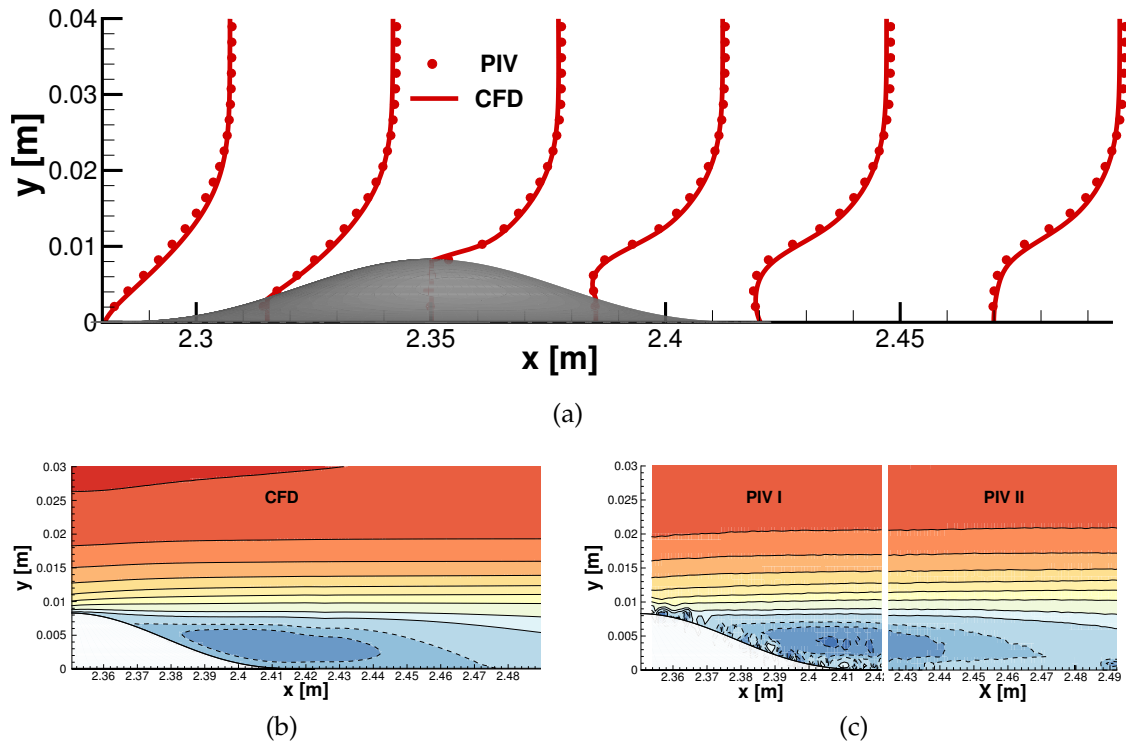


Figure 4.1: (a) Velocity profiles in the vicinity of the roughness element obtained by PIV measurement (*circle*) and CFD calculation (*solid line*). Separation (*dashed line*) at $z = 0.0$ m behind the roughness element obtained by (b) CFD calculation and (c) PIV measurements

negative velocities occur and constitute a separation, which ranges from about $x = 2.37$ to 2.475 m as can be seen in Figure 4.1 (b) and (c).

Using the CTA method, the streamwise velocities can be measured in a large range from $x = 2.0$ m to $x = 3.5$ m. Figure 4.2 (a) illustrates the numerical and experimental velocity distributions in y -direction at several streamwise positions in the symmetry plane $z = 0.0$ m. At $x = 2.0$ m, where influences of the roughness element are not yet perceptible, both numerical and experimental velocity profiles are consistent with the Blasius flow. Behind the roughness element at $x = 2.5$ m, a rapid velocity change in wall-normal direction and an inflection point are observed. As seen above, this originates from the separation behind the roughness element. These reduced velocities are gradually recovered further downstream at $x = 2.8$ and 3.5 m (Figure 4.2 (a)). Velocity profiles at $x = 3.5$ m still show a good agreement between experiments and the steady laminar simulation. This means

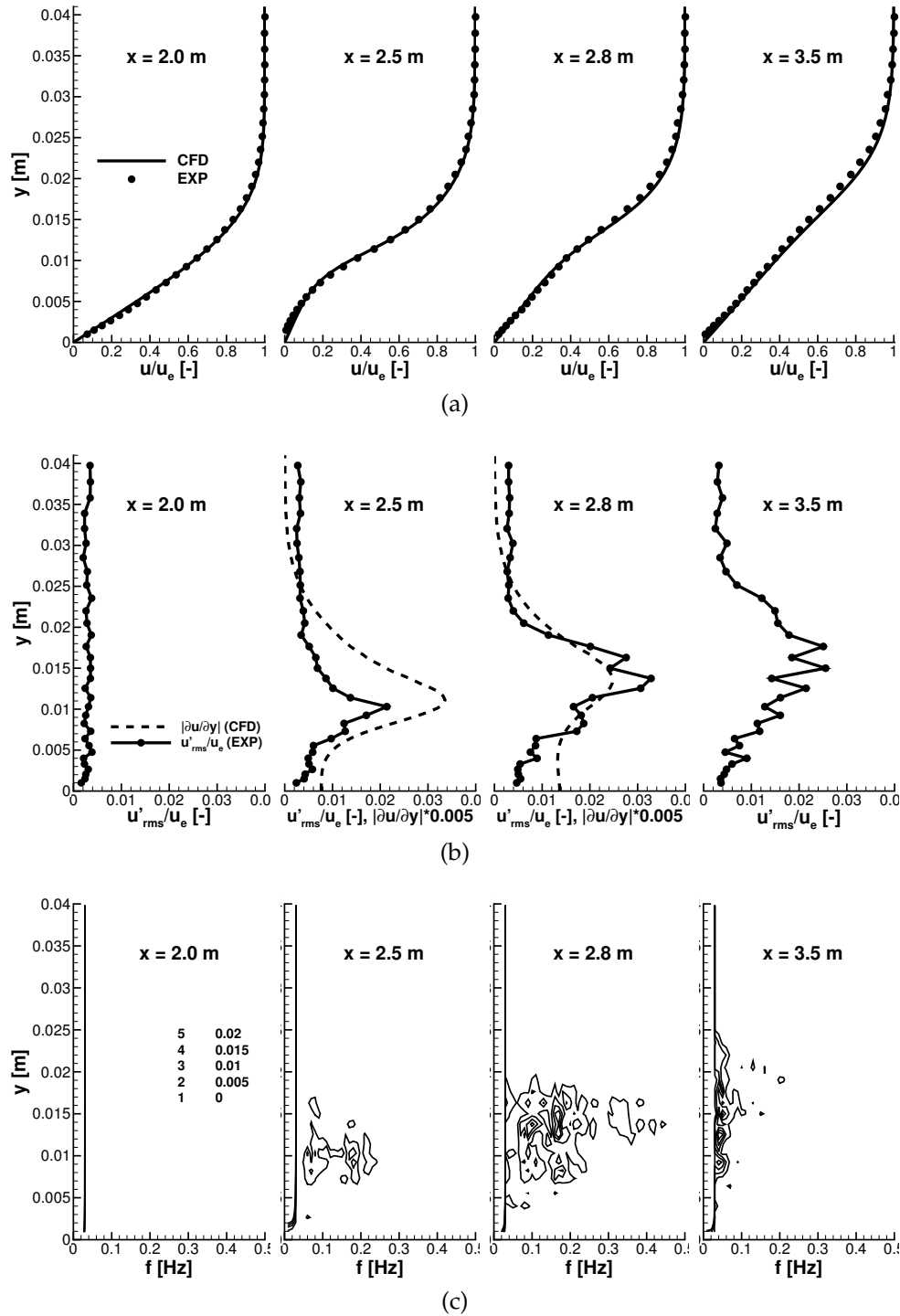


Figure 4.2: (a) Comparison of numerical (*solid line*) and experimental (*circle*) velocity profiles and (b) experimental disturbances (*solid line with circle*) and numerical wall-normal velocity gradient (*dashed line*) and (c) distribution of spectral amplitudes in front of roughness element ($x = 2.0$ m) and downstream ($x = 2.5, 2.8, 3.5$ m) on the symmetry plane $z = 0.0$ m

that the flow has not yet evolved into turbulence.

Figure 4.2 (b) shows experimentally measured disturbances in comparison

with numerically calculated velocity gradients. According to Rayleigh's inflection theorem, as mentioned in Chapter 2, an inflection point on velocity profiles is a sufficient condition for unstable flow. A high shear layer normally presents inflection points; therefore, a study of velocity gradients of velocity profiles compared with disturbances allows an origin of flow instability to be estimated. First, the magnitude of disturbances at $x = 2.0 \text{ m}$ is about $u'_{rms}/u_e = 0.002$ both in- and outside of the boundary layer. This means that neither fundamental instability nor localized disturbances due to the roughness element occurred. Spectral amplitudes illustrated by contour lines with an increment 0.005 in Figure 4.2 (c) also show nothing at $x = 2.0 \text{ m}$. Second, a distinct appearance of disturbances is observed at $x = 2.5 \text{ m}$. The distribution of the disturbances looks like the wall-normal velocity gradient of the numerical calculation. This means that the disturbances in the middle ($z = 0.0 \text{ m}$) originate from the wall-normal shear. Their spectral amplitudes in Figure 4.2 (c) are characterized by a shedding motion with frequencies 0.07 and 0.17 Hz. Third, the growth of the disturbances at 2.8 m also follows the wall-normal velocity gradient. The wall-normal position of the peak rises slightly upward. The distribution of the spectral amplitude also widens in the center of the two frequencies 0.07 and 0.17 Hz. Last, at $x = 3.5 \text{ m}$ ($Re_x = 2.8 \times 10^5$), the disturbances spread out widely and their profile changes into a zig-zag pattern. Spectral amplitudes in Figure 4.2 (c) are concentrated on the lowest frequency area. This means that unstable secondary instability has begun at this position, but a transition to turbulence has not yet started as previously demonstrated by the steady streamwise velocity profiles in Figure 4.2 (a).

4.2 Streamwise elongated streaks

Another important physical phenomenon of the streaky boundary layer induced by a three-dimensional roughness element can be found in the spanwise velocity distribution (Figure 4.3 (a)). First, a reduced velocity area due to the separation

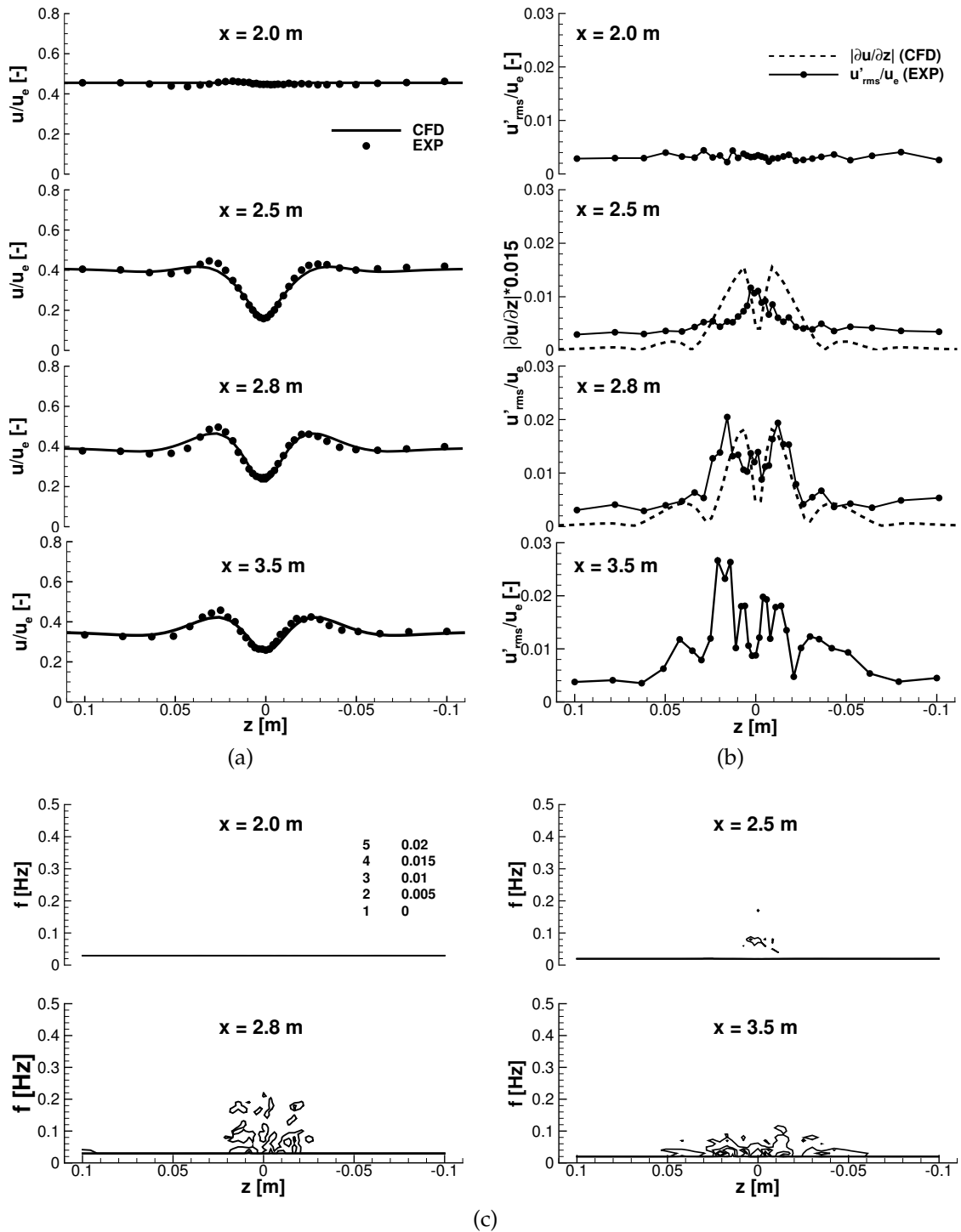
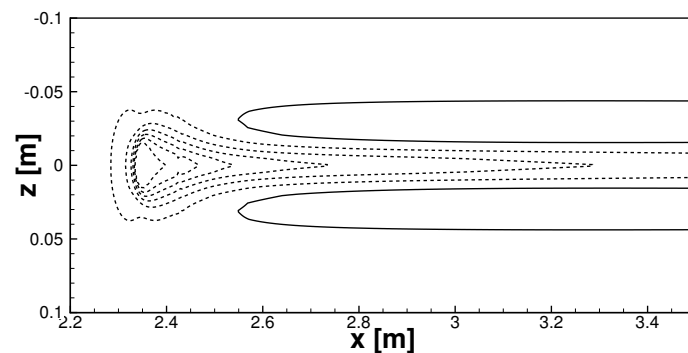


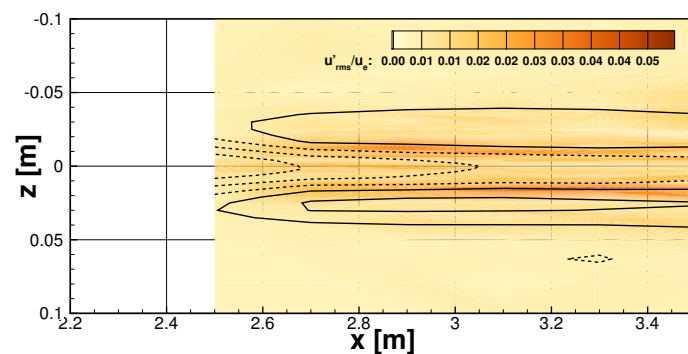
Figure 4.3: (a) Comparison of numerical (*solid line*) and experimental (*circle*) velocity profiles; (b) experimental disturbances (*solid line and circle*) and numerical spanwise velocity gradient (*dashed line*); (c) distribution of spectral amplitudes in front of roughness element ($x = 2.0$ m) and downstream ($x = 2.5, 2.8, 3.5$ m) at $y = 7$ mm

is observed as seen in the previous section in the middle $z = 0.0$ m and recovered gradually in a downstream direction. On both left and right sides, velocity

increases are seen at $x = 2.5 \text{ m}$, $z = \pm 0.025 \text{ m}$ in the spanwise direction. The velocities grow up to $x = 2.8 \text{ m}$ and then decrease slowly to $x = 3.5 \text{ m}$. A noticeable feature of this spanwise velocity variation can be captured by the distribution of streamwise velocity difference $u_p = u(z) - u(z_{max})$ seen in Figure 4.4, in which the undisturbed boundary-layer part $u(z_{max})$ is subtracted from the entire velocity distribution with streaks $u(z)$. In this figure, streamwise elongated high- (on both flanks) and low- (at the middle) speed streaks are clearly recognized on both the results of CFD simulation and experiment. The low-speed streak is stretched from the separation into a downstream direction and the high-speed streaks on the left and right sides are formed from about $x = 2.55 \text{ m}$. (cf. the next paragraph ‘Generation of streamwise streaks’). One should notice here again that the experimental spanwise velocity distribution has a small asymmetry. Figure 4.3 (a) shows a consistent deviation of spanwise velocity profiles between CFD simula-



(a)



(b)

Figure 4.4: Velocity difference distribution u_p (Positive (*solid*) and negative (*dashed line*) value with $\Delta u_p = 0.042$) of (a) CFD simulation and (b) CTA measurements at $y = 0.007 \text{ m}$

tions and experiments at $z = 0.025 m$, and this is also observed in Figure 4.4 (b). In Section 3.1, an improvement of the non-uniformity of the spanwise velocity distribution in the LWK was tried. However, it was difficult to control perfectly and it still appears here.

As in the previous section, experimental disturbances in the spanwise direction are compared with spanwise velocity gradients in Figure 4.3 (b), and their spectral amplitudes are shown in Figure 4.3 (c). The experimental disturbances at $x = 2.5 m$ grow only in the middle, in spite of the distribution of spanwise velocity gradients concentrated on around $z = \pm 0.015 m$. This implies that the disturbances at this streamwise position were produced mainly by the wall-normal shear seen in Figure 4.2 (b) of the previous section and are less affected by the spanwise shear. Spectral amplitudes in Figure 4.3 (c) appear as two groups, one is at about 0.07 and the other at about 0.17 Hz. This is consistent with the spectral amplitude distribution in wall-normal direction in Figure 4.2 (c). Although the spectral amplitudes at $x = 2.5 m$ are too small because the wall-normal measuring position is $y = 7 mm$ (cf. Figure 4.2 (c)), there is no doubt that these amplitudes are produced by wall-normal shear when comparing spectral positions of both 0.07 and 0.17 Hz with wall-normal distribution seen in Figure 4.2 (c). At $x = 2.8 m$, the disturbances in the middle were reduced and outer disturbances were increased on the left and right sides where the spanwise velocity gradient is maximum. It is also seen in Figure 4.4 (b) that these disturbances grow between high- and low-speed streaks. Disturbances at $x = 2.8 m$ are evenly distributed in a range from 0.04 Hz to about 0.2 Hz. This shows that, in contrast to the distribution by wall-normal shear in $x = 2.5 m$, streamwise disturbances that are generated by spanwise shear are steady or quasi-steady. Consequently, these disturbances are originating from spanwise shear based on streamwise streaks. Finally, the disturbances become more irregular further downstream ($x = 3.5 m$) and spread out in both left and right directions. Their spectral amplitudes are also concentrated in a low frequency area, like the wall-normal distribution shown in

Figure 4.2 (c).

Generation of streamwise streaks As introduced in Chapter 1, the streamwise streaks are induced by quasi-steady streamwise vortices generated around the roughness elements based on the lift-up mechanism. Thus, their formation can be identified by investigating the streamwise vorticity, although the *steady* CFD results do not contain perturbing components. Figure 4.5 shows the streamwise vorticity structures ω_x around the roughness element and the high- and low-speed streaks illustrated by velocity differences $u_p = u(z) - u(z_{max})$ in the downstream direction. At $y = 2.0 \text{ mm}$, a pair of counter-rotating vorticities is generated at the front and back side of the roughness element symmetrically in the spanwise direction. In higher positions, the vorticity structures in front of the roughness element are elongated by higher boundary-layer velocities in the streamwise direction and reach the farthest downstream at $y = 6.0 \text{ m}$. At this height, high-speed streaks are also strengthened most significantly. As they reach the top of the roughness element, the vorticity structures steadily disappear (lowest picture at $y = 8.0 \text{ mm}$).

These streamwise elongated vorticity structures and their influences on the flow field are illustrated in streamwise (y, z) -planes in Figure 4.6. At $x = 2.4 \text{ m}$, two pairs of counter-rotating vorticity structures are seen on the upper and lower part of the roughness element (cf. (x, z) -planes at $y = 2.0$ and 6.0 mm in Figure 4.5). A swirling motion of vectors having negative streamwise velocities, i.e., a separation, is observed in the middle behind the roughness element. The vorticity structures gather towards the center at $x = 2.5 \text{ m}$ while decreasing the separation. High-speed flow from the upper boundary-layer is drawn into the area between positive and negative vorticities (*lift-up effect*). The vorticities then decay gradually in the downstream direction and high-speed streaks, which are visualized by the velocity difference u_p in the lowest picture of Figure 4.6, are distinctly formed at $x = 2.6 \text{ m}$ as a result of the lift-up mechanism between the

two counter-rotating streamwise vorticity structures. The low-speed streak arose mainly from a velocity deficiency caused by the separation (also see Figure 4.5).

Fransson et al. (2004) raised a hypothesis that the suboptimal transient growth can be led when a wall-normal position of initial streamwise vortices is lower than optimal disturbances. As seen from the vorticity structures at $x = 2.4 m$ in Figure 4.6, the initial vortices generated by a roughness element depend strongly on the height of the roughness element. Moreover, a development of the streamwise vortices seems to be disturbed somehow by the separation behind the roughness element. Consequently, the roughness element and its separation could be a reason for the suboptimality by itself.

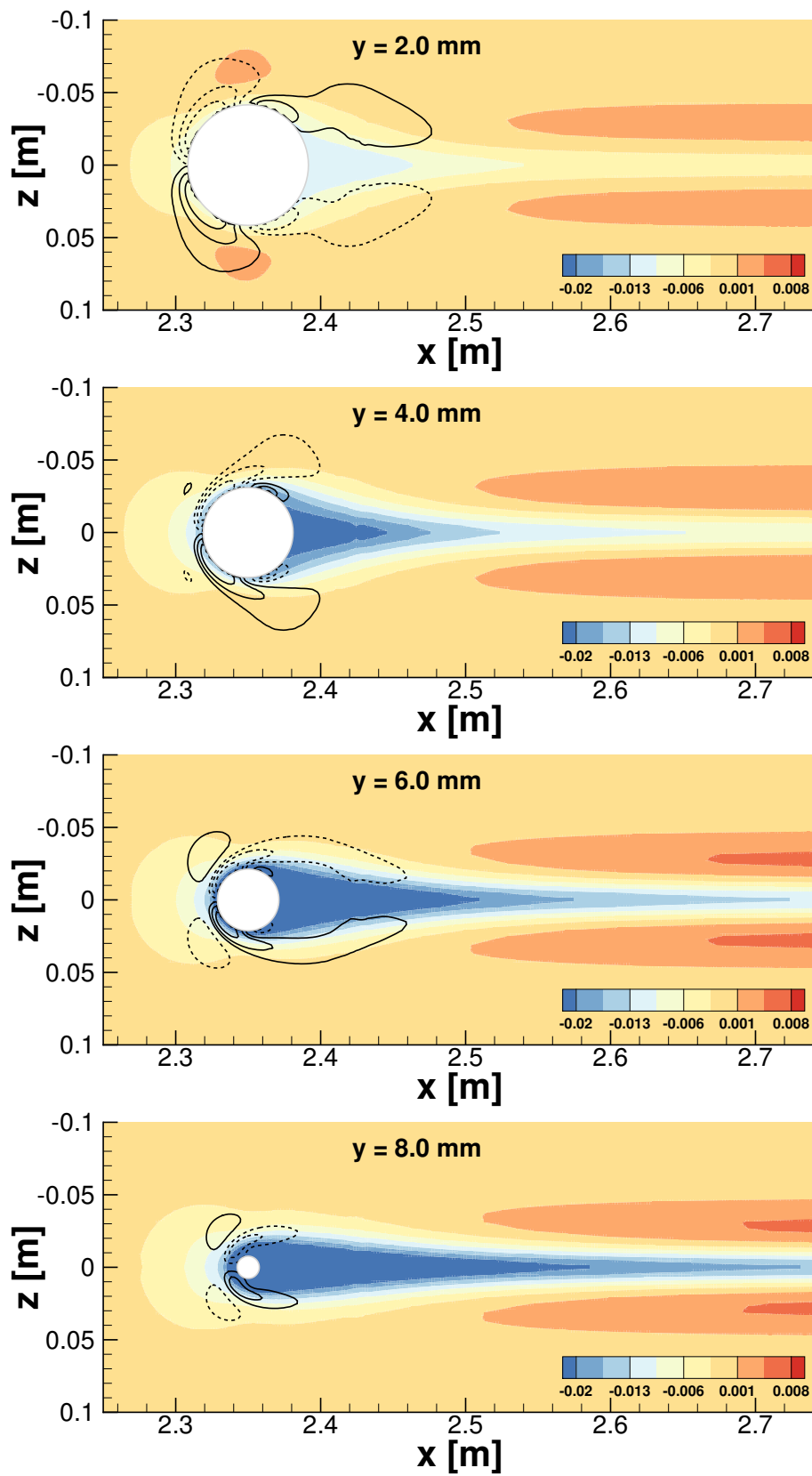


Figure 4.5: Velocity difference u_p (color) and vorticity distribution $\omega_x = \pm 0.5, 1.1, 2.0$ (solid and dashed lines)

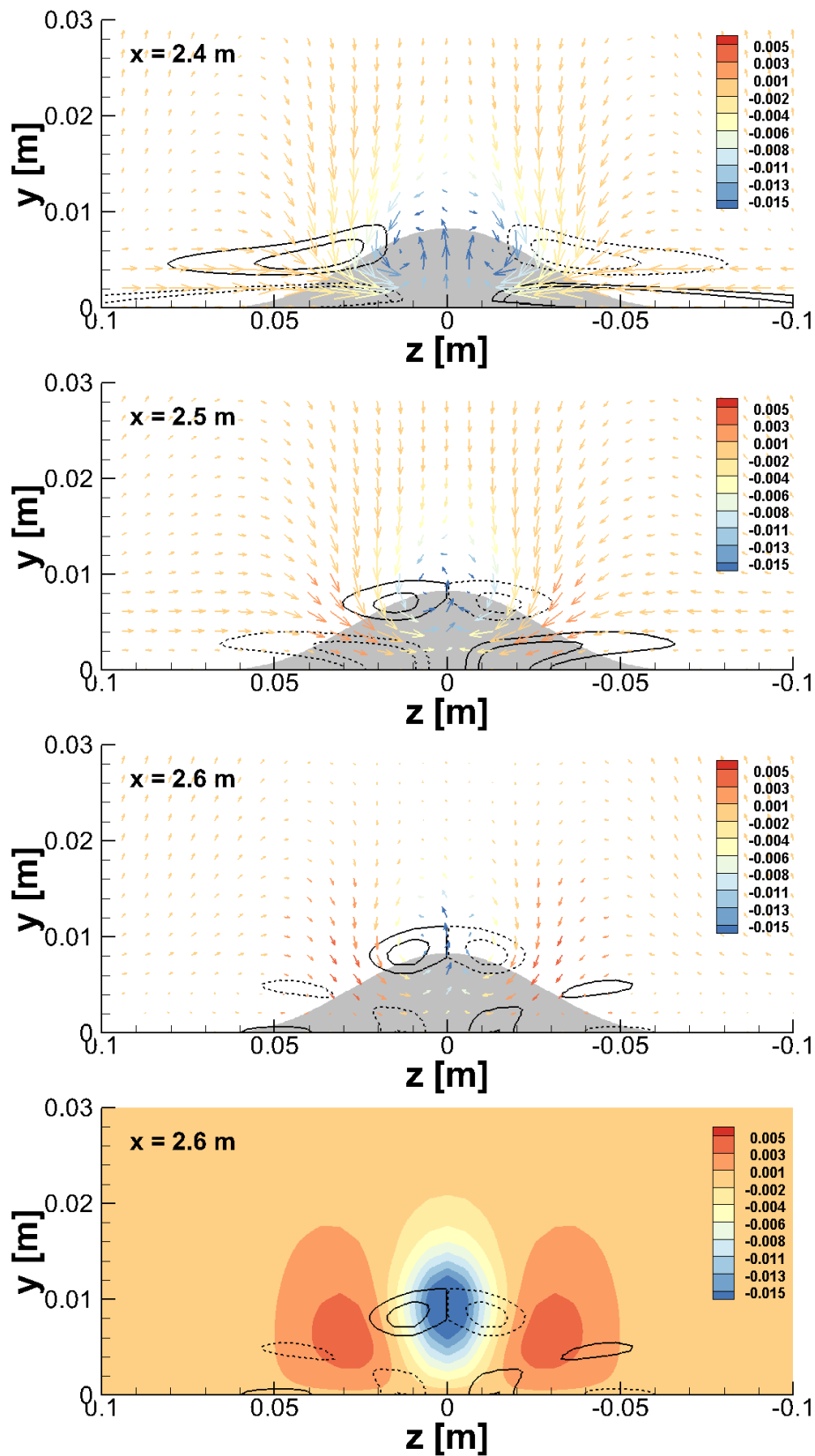


Figure 4.6: Velocity vectors and distribution of velocity difference u_p (color) and vorticity distribution $\omega_x = \pm 0.3, 0.5$ in $x = 2.4$ m, $\omega_x = \pm 0.2, 0.3$ in $x = 2.5$ m, $\omega_x = \pm 0.11, 0.15$ in $x = 2.6$ m (solid and dashed lines)

Chapter 5

Linear Stability Analysis

This chapter shows the results of a stability analysis of the streaky base flow described in the previous chapter and comparisons of calculated eigenmodes with experimental measurements. First, an eigenmode spectrum and its streamwise evolution are considered in Section 5.1. Eigenfunctions of relatively stable TS-modes and their spanwise higher harmonics are also introduced. The main part of this chapter is Section 5.2, in which comparisons of theoretical and experimental eigenfunctions of the most unstable eigenmodes and an analysis of streamwise evolution are performed. A preliminary test for an artificial forcing of a specific eigenmode is dealt with in Section 5.3.

5.1 Eigenmode spectrum

An eigenmode spectrum with a streamwise wave number $\alpha = 2\pi/\lambda = 33$ at $x = 2.5 \text{ m}$ is shown in Figure 5.1 (a). At first, a grid convergence study was conducted with various grid points from 30×30 to 130×130 on a 2D (y, z) -cross-cut domain, as seen in Figure 2.1. Some high-resolution results in Figure 5.1 (a) show that most eigenvalues converged with 130×130 resolution. Thus, this resolution has been used for all calculations that follow below. Two distinguishable unstable modes, which exhibit symmetrical and asymmetrical eigenfunctions with respect

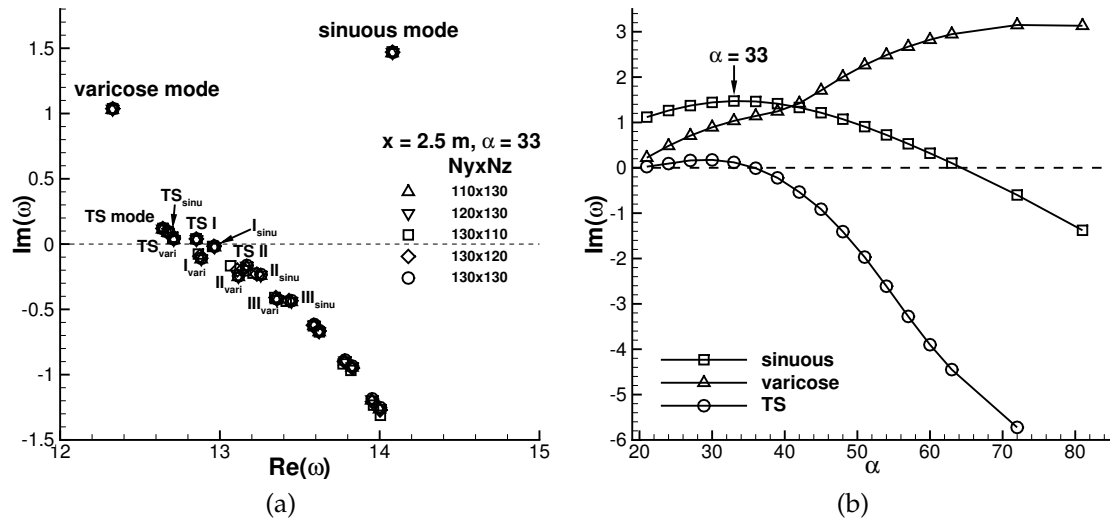


Figure 5.1: (a) Eigenmode spectrum in terms of growth rate $\text{Im}(\omega)$ with varying angular frequency $\text{Re}(\omega)$ at $x = 2.5 \text{ m}$. Streamwise wave number is $\alpha = 33$ and N_y and N_z are the number of grid points in wall-normal and spanwise direction, respectively. I, II, and III mean first, second, and third harmonic and subscript **sinu** and **vari** indicate sinuous and varicose mode. (b) Growth rate of varicose (Δ), sinuous (\square), and TS (\circ) mode with varying streamwise wave number α

to the spanwise coordinate and are the so-called *varicose* and *sinuous* mode, are found in the highly unstable region, and their eigenfunctions will be explained in detail in Section 5.2. As described by Andersson et al. (2001), who investigated the breakdown of boundary-layer streaks, the sinuous eigenmode is the most unstable mode. So, the present study focuses on the sinuous mode. The streamwise wave number $\alpha = 33$, in which the sinuous mode has the maximum growth rate (see Figure 5.1 (b)), was selected for a temporal stability calculation.

TS mode and spanwise higher harmonic An unstable mode indicated as **TS-mode** in Figure 5.1 (b) is seen slightly above the neutral line $\text{Im}(\omega) = 0$ and followed by pairs of higher harmonic modes in the spanwise direction, which also occur in varicose and sinuous patterns. The eigenfunctions of the TS modes are shown in Figure 5.2. Figure 5.2 (a) shows an amplitude concentration in the middle, which occurred by a provocation of the roughness element, and undisturbed TS wave amplitudes are observed outward. The growth rate and angular

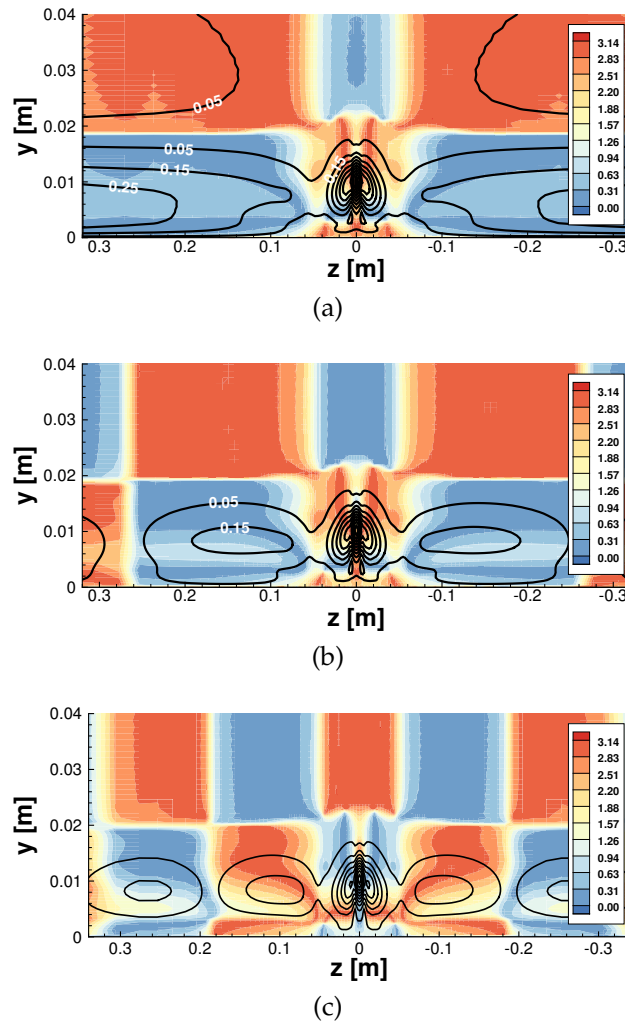


Figure 5.2: Streamwise amplitude \hat{u}/\hat{u}_{max} (solid lines with 0.1 increment) and phase (color) distribution of (a) TS and its (b) 1st and (c) 2nd harmonic mode (TS mode, TS I, and TS II in Figure 5.1, respectively)

frequency of the mode is $\omega = 12.6 + 0.11i$, and this is consistent with a classical TS wave of $\omega = 12.5 + 0.18i$ in a 2D boundary-layer without roughness element under the same flow conditions in this study, although its calculation is not described here. Moreover, the amplitude distribution in y -direction on the outside, where the influences of the roughness element are non-existent or sufficiently weak, is very similar to the classical TS wave, especially with respect to a double peak with a phase difference π . For these reasons, this was named TS mode. The phase differences between the middle where the amplitudes are generated by the roughness element and the outside also have opposite signs. Spanwise high harmonics of the TS mode are illustrated in Figure 5.2 (b) and (c). The amplitude

concentration in the middle has hardly changed, whereas the amplitudes outside of the center are divided into standing wave patterns, which oscillate oppositely. The growth rates $\text{Im}(\omega)$ of these modes are mostly found in the negative area, which means they decay gradually.

Streamwise evolution To compare with experimentally measured disturbances, which are growing spatially in a laboratory test section (cf. subsection 5.2.3), spatial growth rates α_i are required, and these can be calculated by the LST with a spatial approach. However, spatial stability calculations, in which the governing equations are formulated as a non-linear eigenvalue problem, need maximal twice the working memory. For this reason, the Gaster transformation according to Koch et al. (2000)

$$\begin{aligned}
 \omega_{r,s} &= \omega_{r,t} \\
 \alpha_{r,s} &= \alpha_{r,t} \\
 \hat{q}_s(y, z) &= \hat{q}_t(y, z) \\
 \alpha_{i,s} &= -\frac{\omega_{i,t}}{c_{gr,t}}, \quad c_{gr,t} = \frac{\partial \omega_{r,t}}{\partial \alpha_{r,t}} \approx \frac{\omega_{r,t}}{\alpha_{r,t}} = c_{ph,t}
 \end{aligned} \tag{5.1}$$

where c_{gr} and c_{ph} are group and phase velocity and indices s and t indicate spatial and temporal approach, respectively, is a very efficient way of converting the temporal growth rates (ω_i) into spatial ones (α_i). Figure 5.3 (a) shows a comparison of the spatial growth rates calculated by the Gaster transformation with those obtained by directly applying the spatial approach. The temporal stability calculation was performed with a streamwise wave number $\alpha_r = 33$, as explained above, and then their temporal growth rates were transformed into spatial ones by the Gaster transformation. The spatial stability calculations were done with two constant frequencies $\omega_r = 12.33$ and 14.08 , which are the frequencies of the sinuous and varicose eigenmode calculated by the temporal calculation. Although the temporal calculations were performed with a grid resolution 130×130 , a grid resolution 120×120 was used for the spatial calculation owing to a limitation

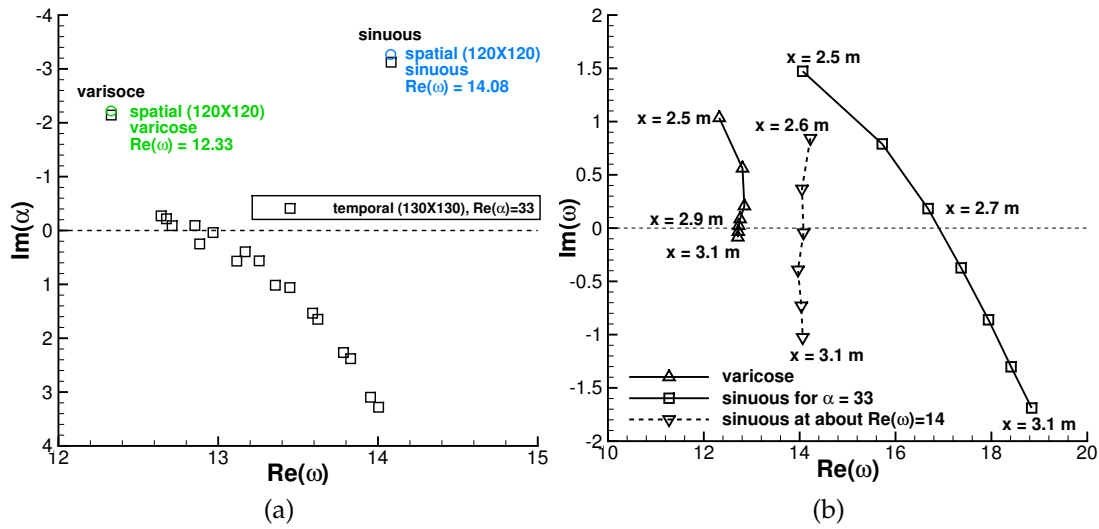


Figure 5.3: (a) Comparisons of spatial growth rates α_i calculated by the Gaster transformation (\square) and by spatial approach (\circ) at $x = 2.5$ m (b) Streamwise evolution of growth rate $\text{Im}(\omega)$ according to angular frequency $\text{Re}(\omega)$ of varicose (\triangle) and sinuous (\square, ∇) mode from $x = 2.5$ to 3.1 m. All eigenvalues connected by a solid line are obtained for the constant $\alpha = 33$. Those connected by a dashed line are obtained for $\omega_r \approx \text{const}$.

of working memory. Nonetheless, the results are reasonably close to each other. Also, Groskopf et al. (2010), who used the same computer code as in the present study, showed an excellent agreement of directly computed spatial growth rates with temporal growth rates after applying Gaster's transformation. Moreover, as will be seen in Section 5.2, the mode shape is less dependent on the streamwise spatial evolution. Therefore, for an efficient computation, the temporal stability calculations with the Gaster transformation were carried out in the present study for comparison with the experimental results.

The streamwise evolution of the two most unstable varicose and sinuous modes can be analyzed by observing several successive eigenmodes in the streamwise direction (Figure 5.3 (b)). Amplitudes of the varicose and sinuous mode increase up to $x = 2.9$ m and $x = 2.7$ m, respectively, and then decrease gradually in the downstream direction. The temporal growth rate $\text{Im}(\omega)$ of the sinuous mode is higher than of the varicose case near the roughness element at $x = 2.5$ m, but also falls off faster in the downstream direction. As the growth rates of the vari-

cosine mode are gathered close to the neutral line $\text{Im}(\omega) = 0$, amplitudes of the varicose mode are reduced far more slowly. The angular frequency of the sinuous mode rises steadily in a wide range between $\text{Re}(\omega) = 14$ and 19 with a constant α . However, the frequency of the sinuous mode may be physically conserved in experiments. To approximate this assumption, the most unstable frequency $\text{Re}(\omega) = 14$ of the sinuous mode at $x = 2.5 \text{ m}$ was tracked by adjusting α (see dashed line in Fig. 5.3 (b)). As a result, the amplification rates for this path are somewhat larger than for the case with fixed streamwise wave number $\alpha = 33$. The corresponding streamwise wave numbers vary from $\alpha = 30$ at $x = 2.6 \text{ m}$ to $\alpha = 25$ at $x = 3.1 \text{ m}$. In comparisons with experiments later, these eigenvalues will be considered. In contrast, the frequency and the streamwise wave number of the varicose mode are maintained at about $\text{Re}(\omega) = 13$ and $\alpha = 33$, which are very similar to the angular frequency of the TS-mode.

5.2 Varicose and sinuous mode

5.2.1 Eigenfunctions

Amplitude and phase distributions of the varicose and the sinuous mode at $x = 2.7 \text{ m}$ where the sinuous mode is most developed (cf. Figure 5.3 (b)) are illustrated in Figure 5.4 from (c) to (h). The streamwise amplitudes \hat{u}/\hat{u}_{max} of the varicose mode in Figure 5.4 (c) are intensively concentrated in the middle of the roughness element $z = 0.0 \text{ m}$, and this is comparable with the largest velocity gradient in wall-normal direction in Figure 5.4 (a). These strong wall-normal velocity gradients originate from the low-speed streak generated behind the roughness element. Relatively weaker amplitudes at both opposite sides $z = \pm 0.035$ and $\pm 0.075 \text{ m}$ in Figure 5.4 (c) can be compared with wall-normal velocity gradients of the high- and low-speed streaks illustrated by the velocity difference u_p in Figure 5.4 (a). Hence, the varicose mode depends on the wall-normal velocity

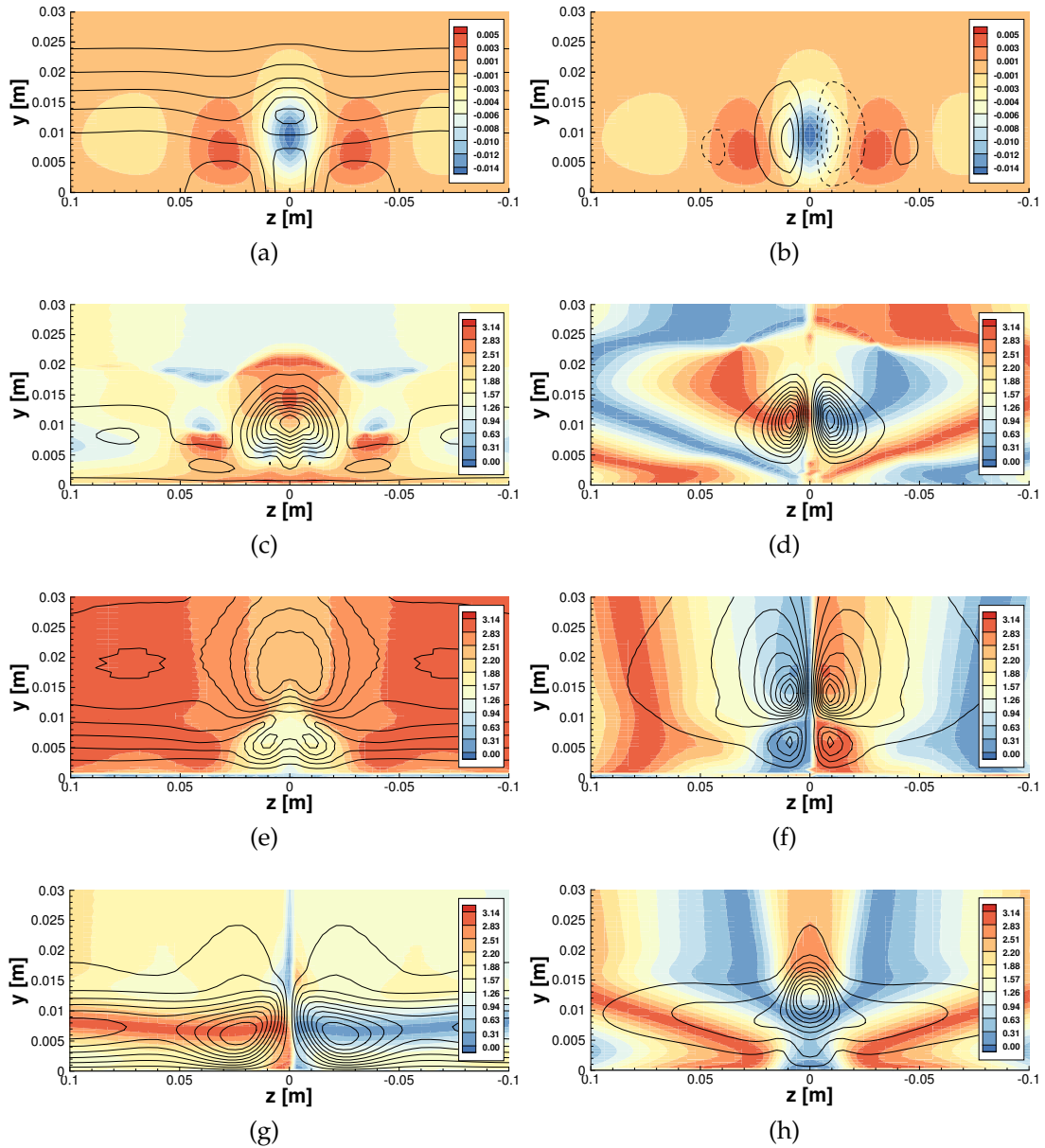


Figure 5.4: (a) Wall-normal and (b) spanwise velocity gradient (*solid and dashed line* with 10 increment for (a) and 5 increment for (b)) and velocity difference u_p (*color*) at $x = 2.7$ m. Eigenfunction of varicose mode (c) \hat{u}/\hat{u}_{max} (e) \hat{v}/\hat{v}_{max} (g) \hat{w}/\hat{w}_{max} and sinuous mode (d) \hat{u}/\hat{u}_{max} (f) \hat{v}/\hat{v}_{max} (h) \hat{w}/\hat{w}_{max} . *Solid lines* illustrate amplitudes with 0.167 increment, *color* absolute phase distribution

gradients of the streaky base flow. In combination with a dragging up of wall-normal \hat{v}/\hat{v}_{max} (Figure 5.4 (e)) amplitudes and a centering of spanwise \hat{w}/\hat{w}_{max} (Figure 5.4 (g)) amplitudes, the streamwise amplitudes oscillate symmetrically with respect to the spanwise coordinate.

The sinuous eigenmode can be understood by correlating with a spanwise ve-

locity gradient of the streaky base flow in Figure 5.4 (b). This velocity gradient is based on velocity differences between the high- and low-speed streaks in the spanwise direction and the maximum gradients are located between them. The streamwise amplitudes of the sinuous mode in Figure 5.4 (d) are also split into two parts with respect to the middle at $z = 0.0$ m, like the spanwise velocity gradient, and concentrated on the position where the velocity gradient is maximum. Furthermore, the opposite sign of the velocity gradient on left and right side matches well with the phase difference of about π shown in Figure 5.4(d). With an intersecting up- and downward movement of the wall-normal amplitudes (Figure 5.4 (f)) and a translating left and right side of spanwise amplitudes (Figure 5.4 (h)), respectively, left and right halves of the streamwise amplitudes oscillate alternatively forward and backward. Consequently, it can be assumed that the sinuous mode belongs to the spanwise velocity gradient of the streamwise streaks.

Temporal evolution The behaviour of the eigenfunctions and quasi-steady flows distorted by them can be intuitively observed in a temporal evolution. A sinusoidal expansion can be used for the evolution

$$u' = \hat{u} \cdot \sin(\alpha_r x - \omega_r t + \Phi) \quad (5.2)$$

where α_r and ω_r are the streamwise wave number and frequency, respectively, and Φ is the phase distribution. These variables are taken from the eigenmodes and -functions. Moderate amplitudes, 7% of the external velocity u_e for the varicose and 10% of u_e for the sinuous mode, are applied to the steady base flow. Figure 5.5 illustrates the results.

The upper part of Figure 5.5 (a) illustrates the perturbation structure of the varicose mode. As expected from the analysis of the eigenfunctions above, the streamwise amplitudes oscillate symmetrically, and a varicose flow pattern is

formed in combination with steady velocity components (upper part of Figure 5.5 (b)). The perturbation structure of the sinuous mode (lower part of Figure 5.5 (a)) consists of a pair of streamwise amplitudes oscillating in the opposite direction. By this perturbation's behavior, the steady flow is modified into a wavy flow pattern (lower part of Figure 5.5 (b)). These two flow patterns are the typical fundamental varicose and sinuous mode of streamwise streaks (Andersson et al., 2001).

5.2.2 Experimental measurements

In the LST, whose governing equations are formulated as an eigenvalue problem as shown in Chapter 2, each eigenmode is calculated independently. However, in practical flows, the eigenmodes occur concurrently and might influence each other. Thus, to find an experimental existence of each eigenmode and to investigate interactions between the modes is valuable for a physical understanding of flow instability. Experimental measurements of the present work have been performed under a *natural* condition, i.e. without any spectral control. Therefore,

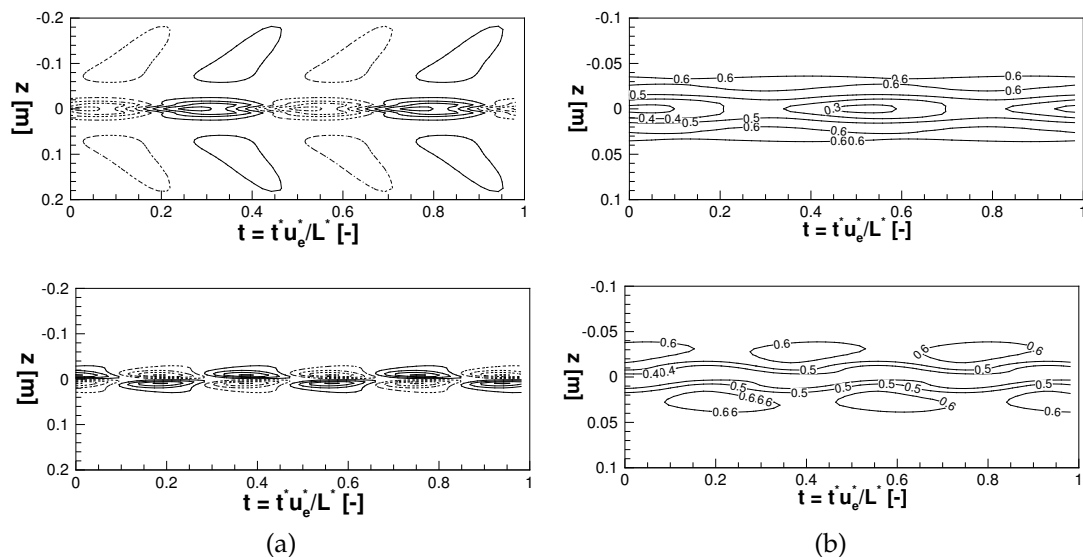


Figure 5.5: Temporal evolution of (a) streamwise perturbation and (b) superposition with steady base flow $u = \bar{u} + u'$ of varicose (upper part) and sinuous (lower part) mode at $x = 2.7 m$. Dashed lines indicate negative values and superscript * means dimensional value

a careful acquisition and evaluation of signals is required to correctly identify each instability mode. The signal processing for acquiring high-resolved signals was already explained in Section 3.4, and evaluation of the acquired signals and comparisons with the theoretical eigenmodes are introduced in this subsection.

Signal evaluation As seen in the previous subsection, the varicose and sinuous eigenmode behave symmetrically and asymmetrically with respect to the spanwise coordinate. To separate experimentally the velocity signals into symmetrical (varicose) and asymmetrical (sinuous) parts, as explained in Section 3.4, two identical hot-film probes were installed at the same spanwise distance from the symmetry plane at $z = 0.0 \text{ m}$ which simultaneously acquired the signals. Figure 5.6 (a) shows an example of the signals. The signals from both probes correlate strongly with each other. It means that a symmetrical instability is dominant. At

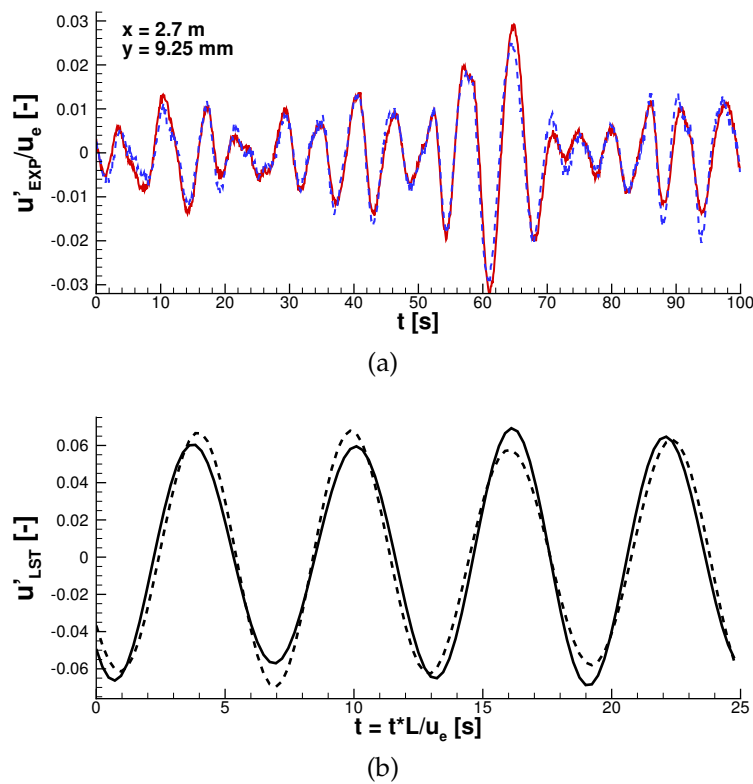


Figure 5.6: (a) Experimental signal of the streamwise amplitude component at $z = 9.5 \text{ mm}$ (solid) and $z = -9.5 \text{ mm}$ (dashed line) ($x = 2.7 \text{ m}, y = 9.25 \text{ mm}$) (b) simulation of their difference

a closer look to the peak of the signals, however, an alternating occurrence of amplitude peaks of each signal (red-solid and blue-dashed line in the figure) on the opposite side is observed due to the asymmetric sinuous mode.

This can be inferred from the simulated signal in Figure 5.6 (b). Theoretical eigenfunctions selected from the varicose and the sinuous eigenmode at the same positions where the experimental signals are collected are expanded temporally by Equation (5.2) with their own frequencies (hence the initial phase difference was not considered). The amplitudes of the sinuous mode are normalized by its maximum value and new amplitudes corrected by the maximum varicose amplitude with an amplitude ratio $\epsilon_{vari}/\epsilon_{sinu} = 5$ are applied like,

$$\begin{aligned} u'_{LST,R} &= u'_{LST,vari} + \frac{u'_{LST,sinu}}{|u'_{LST,sinu}|_{max}} \cdot \frac{|u'_{LST,vari}|_{max}}{\epsilon_{vari}/\epsilon_{sinu}} \\ u'_{LST,L} &= u'_{LST,vari} - \frac{u'_{LST,sinu}}{|u'_{LST,sinu}|_{max}} \cdot \frac{|u'_{LST,vari}|_{max}}{\epsilon_{vari}/\epsilon_{sinu}} \end{aligned} \quad (5.3)$$

where the subscripts R and L mean the position $z = 9.5$ and -9.5 mm, respectively, where the hot-film probes are located, so the corrected sinuous amplitudes were added and subtracted, respectively. Amplitudes were not scaled between the experimental and simulated signals due to an intention for qualitative comparisons only. A behaviour very similar to the experimental signals is observed also in the theoretical ones in Figure 5.6 (b), but due to the fact that the present study had been performed under a natural condition without external disturbance control as mentioned previously, the streamwise disturbance signals versus time in the experiment are less harmonic.

Figure 5.7 shows the Fourier transformed spectra of the acquired signals from each probe. First of all, both magnitudes and shape of the amplitudes are quite similar to each other, as expected from the direct comparisons of the time traces above in Figure 5.6. Particularly, the distribution of absolute phase differences between these two amplitudes in Figure 5.7 (b) is almost $|\Delta\Phi| = 0$ at $y = 0.012$ m where the amplitudes are mostly developed. This implies that the symmetrical

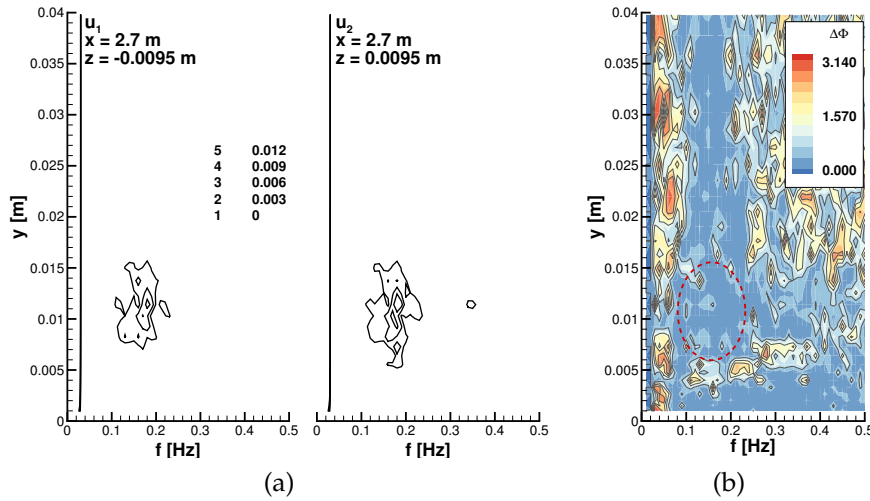


Figure 5.7: (a) Disturbance amplitude at $x = 2.7$ m in frequency domain from probe 1 and 2. (b) Absolute phase difference ($|\Delta\Phi|$). Red dashed line indicates the area where large amplitudes are mostly located

property is a dominant factor characterizing the flow instability of the streaky layer in this study. In other words, the varicose mode is the dominant mode, although the sinuous mode grows maximally up to $x = 2.7$ m according to the theoretical growth rates in Figure 5.3 (b).

Quantitative comparisons To obtain the unstable eigenmodes for the experiment, signal separation into varicose and sinuous components was performed by Equation (3.8), and the results at $x = 2.7$ m are shown in Figure 5.8. The spectral amplitude distributions of the varicose mode in Figure 5.8 (a) are quite similar to the amplitudes from a single probe in Figure 5.7 (a) in shape and magnitude. On the contrary, the amplitudes of the sinuous part are rather faint and are approximately five times smaller than the varicose part (also see x -axis on Figure 5.8 (b)).

For comparisons with experimental results, the theoretical angular frequencies ω_r can be transformed into dimensional frequencies by

$$f = \frac{\omega_r u_e}{2\pi L} \quad (5.4)$$

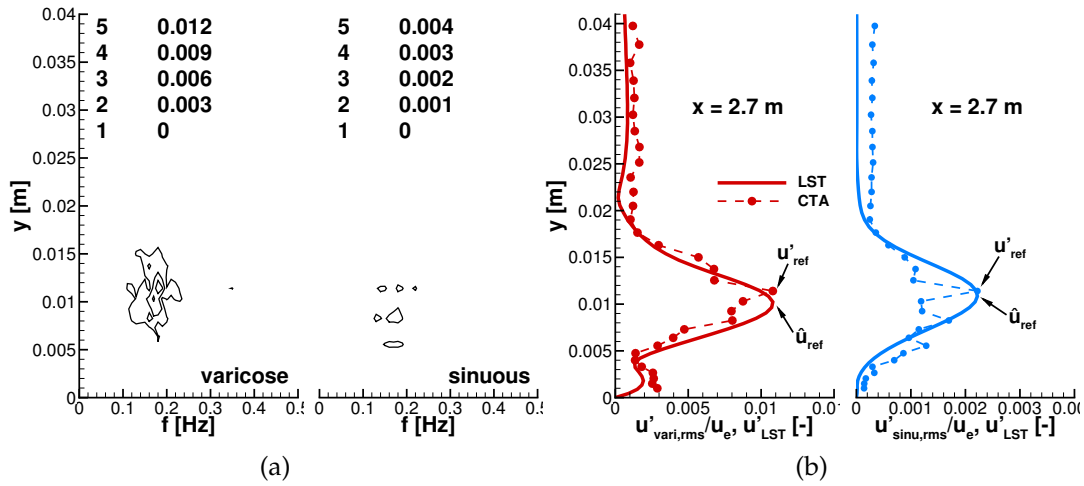


Figure 5.8: Numerically separated varicose (left) and sinuous (right) signal (a) in the frequency domain and (b) rms -values in comparison with LST. Arrows indicate wall-normal positions where the reference values \hat{u}_{ref} and u'_{ref} are selected

where the reference length is $L = 1$ m. First, the $\omega_r = 12.8$ of the varicose mode in Figure 5.3 (b) leads to a frequency $f = 0.16$ Hz. The experimental amplitudes of the varicose component in Figure 5.8 (a) are distributed around $f = 0.18$ Hz, which is satisfactorily close to the theoretically predicted frequency $f = 0.16$ Hz. Second, the theoretical angular frequencies of the sinuous mode $\omega_r \approx 14$ corresponds to $f \approx 0.18$ Hz. The experimental sinuous amplitudes in Figure 5.8 (a) lie between $f = 0.13$ and 0.21 Hz. This spans the theoretical prediction well, but essentially the experimental sinuous amplitudes were unsatisfactory. To compare the magnitude and mode shape of the experimental results with the theoretical ones, the normalized theoretical eigenfunctions \hat{u}/\hat{u}_{ref} were adjusted by non-dimensional experimental amplitudes of streamwise disturbances u'_{ref}/u_e

$$u'_{LST} = \frac{\hat{u}}{\hat{u}_{ref}} \cdot \frac{u'_{ref}}{u_e} \quad (5.5)$$

where the theoretical and experimental reference amplitudes \hat{u}_{ref} and u'_{ref} are taken at the maximum value in wall-normal direction. The theoretical amplitudes were extracted at $z = 9.5$ mm, where the hot-film probe was located, and compared with rms -valued experimental streamwise disturbances in Figure 5.8 (b).

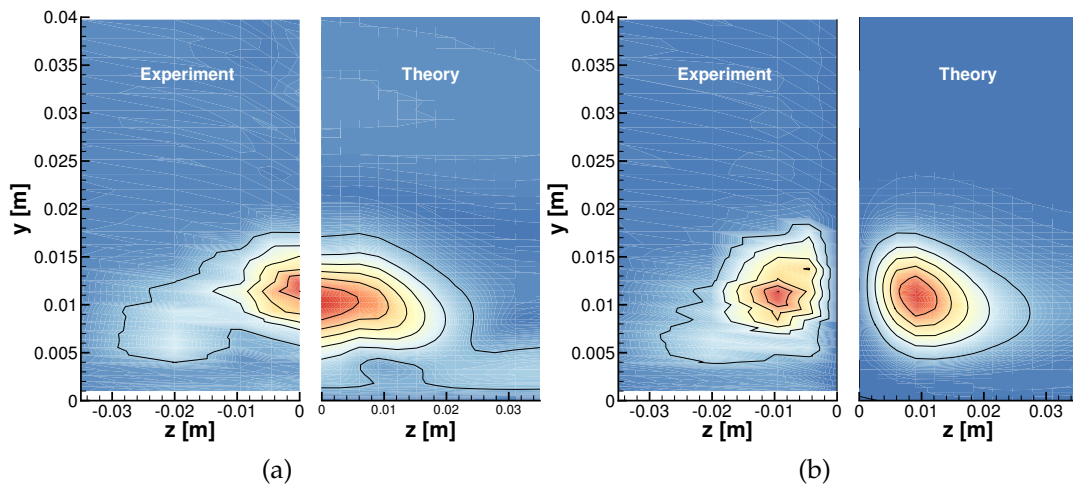


Figure 5.9: Comparison of experimental amplitude u'/u'_{max} (left side) with the theory \hat{u}/\hat{u}_{max} (right side) in a 2D plane at $x = 2.7 m$. (a) varicose and (b) sinuous mode

The amplitude profile of the varicose mode shows a good agreement between theoretical and experimental results. Peaks at both $y = 0.002$ and $0.01 m$ are adequately reproduced. The sinuous mode exhibits, however, two-point oscillations near $y = 0.01 m$, where the amplitude is maximum. Some experimental noise is also observed in the upper boundary layer above $y = 0.0158 m$. In summary, the instability of the streaky flow generated by the roughness element is dominated by the varicose mode, while the sinuous mode in aspects of both magnitude and spectrum is somehow hidden by the larger varicose mode and/or some other disturbances, as well as experimental noise.

Qualitative comparison As mentioned in Subsection 3.4.1, experimental amplitudes were measured at several spanwise positions at $x = 2.7 m$ by widening the distance between the two probes at the same intervals. After a normalization by their maximum value, the results are depicted on a two-dimensional plane perpendicular to the flow direction and compared with the theoretical results in Figure 5.9. Despite the weakness of the experimental sinuous mode, the mode shape agrees well with the theoretical eigenfunction; see Figure 5.9 (b). On the other side, the maximum amplitude of the experimental varicose mode in the

middle $z = 0.0 \text{ m}$ (Figure 5.9 (a)) is located a little higher than the theoretical one and has a shaper peak. The works of White (2002) and Fransson et al. (2004) also found that the experimental streaks slightly move upward in a downstream direction, but the numerical simulation in the present study did not catch that. The differences of amplitude concentration may be caused by the technical limitation that a simultaneous signal acquisition of two hot-film probes is impossible at $z = 0.0 \text{ m}$, i.e. interval $\Delta z = 0.0 \text{ m}$. So, for the varicose amplitudes, only signals from a single probe at $z = 0.0 \text{ m}$ were inserted, and the sinuous amplitudes were assumed to be zero. Nevertheless, it is notable that the presence of both the varicose and sinuous modes has experimentally been identified in an *uncontrolled* practical flow.

5.2.3 Streamwise development of disturbances

Theoretical eigenfunction The theoretical eigenfunctions which are calculated independently at selected streamwise positions could be interlinked with each other in streamwise order by applying e^N -factors

$$\tilde{u}(X, y, z) = \frac{\hat{u}_X(y, z)}{\hat{u}_{X, \max}(y, z)} \cdot e^N(X), \quad N = \int -\alpha_i dX \quad (5.6)$$

where X is the streamwise position where stability calculations were performed. As explained in section 5.1, the spatial growth rates α_i were obtained by the Gaster transformation from temporal growth rates ω_i and integrations were carried out by a trapezoidal rule at every streamwise position X . Figure 5.10 illustrates the results. The varicose amplitudes (Figure 5.10 (a)) develop initially with disturbances from a high shear layer detached from the top of the roughness element in the middle at $x = 2.5 \text{ m}$ and streamwise streaks here are not fully developed yet. From $x = 2.7 \text{ m}$, additional local maxima based on wall-normal velocity gradients of the streaks as explained in the previous section, begin to appear apart from the centre. Further downstream, the outside amplitudes at $z = \pm 0.08 \text{ m}$ grow grad-

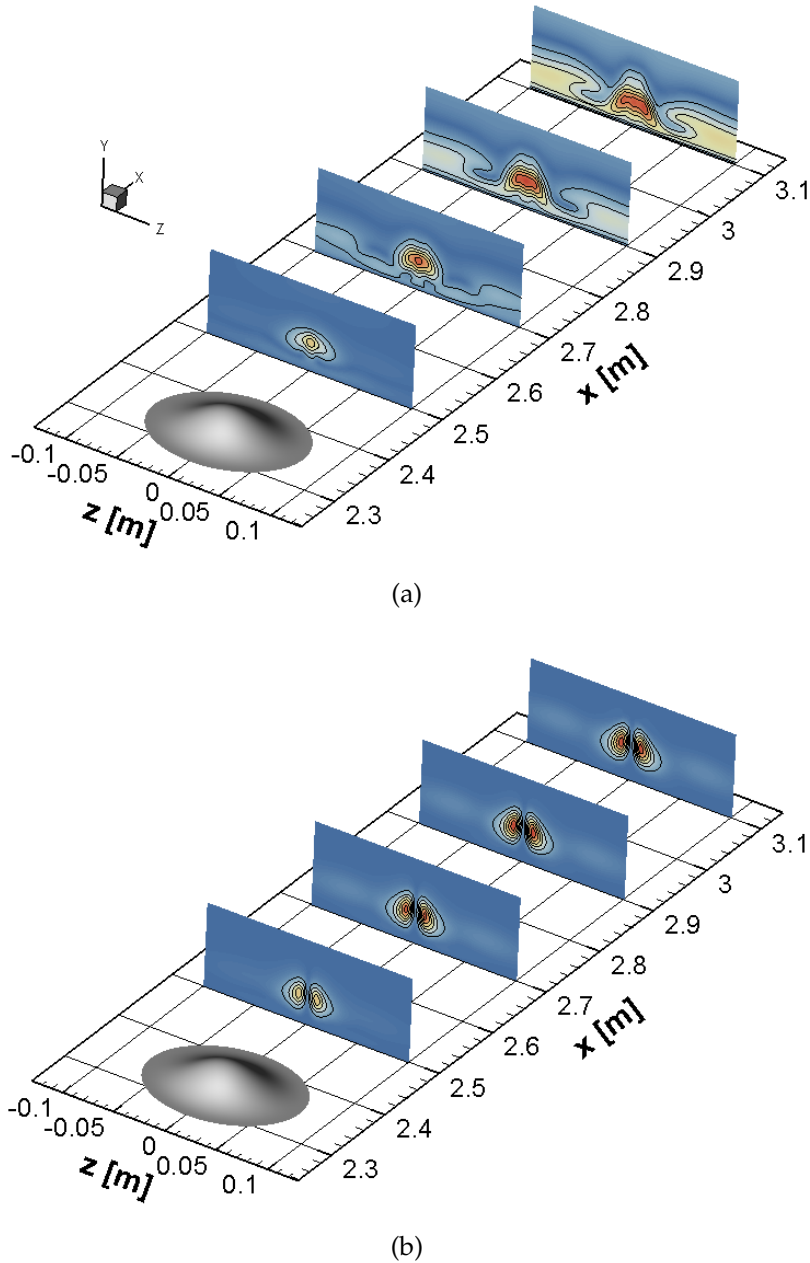


Figure 5.10: Development of streamwise velocity perturbation of (a) varicose and (b) sinuous mode. Both *color* and *solid line* indicate amplitudes \tilde{u} corrected by the e^N -factor

ually according to the increasing of the streaks, while the amplitude along the center line decrease in accordance with the lower growth rates in Figure 5.3 (b). In contrast, the streamwise evolution of the sinuous mode in Figure 5.10 (b) does not show considerable changes in both mode shape and distribution in the middle of $z = \pm 9.5 \text{ mm}$. Amplitudes reach their maximum at $x = 2.8 \text{ m}$. These results

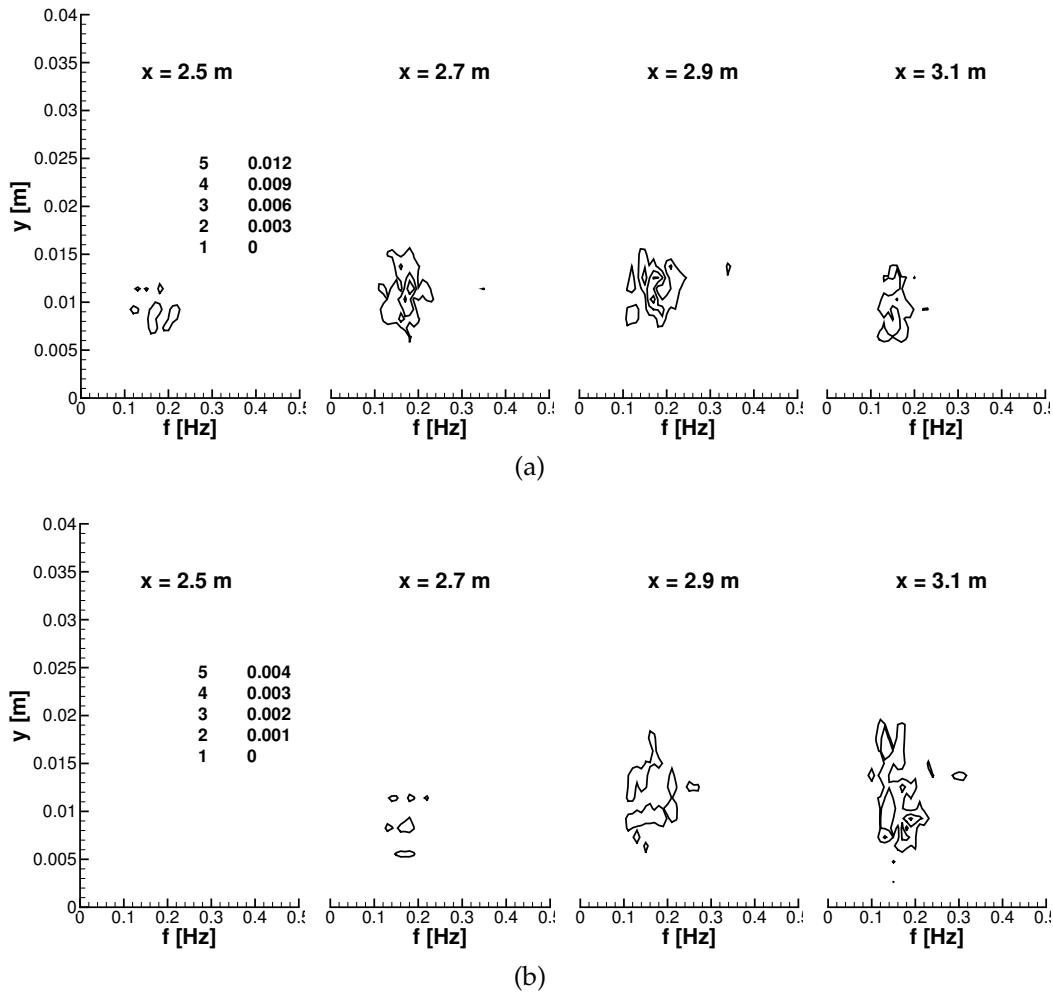


Figure 5.11: Amplitude development of streamwise velocity perturbation. (a) varicose and (b) sinuous mode

are also observed in the study of Denissen and White (2013) who investigated a secondary instability based on roughness-induced transient growth.

Experimental disturbance The evolution of the experimental varicose and sinuous mode in the downstream direction is illustrated in Figure 5.11. According to the eigenmodes in Figure 5.3 (b), amplitudes of the varicose mode grow up to $x = 2.9$ m and then decrease gradually. The experimentally measured amplitudes in Figure 5.11 (a) follow this theoretical prediction. Their frequency is also constantly maintained between $f = 0.1$ and 0.2 Hz well. Even though a smaller contour level than for the varicose mode has been used for depicting the sinuous amplitudes in Figure 5.11 (b), no contour lines are seen at $x = 2.5$ m. These sin-

uous amplitudes grow without cease in the downstream direction, in contrast to the theoretical result, in which the disturbances grow up to $x = 2.7 \text{ m}$ and then decrease. The spectral distribution of the experimental amplitudes widens in the downstream direction. However, the center of the distribution is maintained at about $f = 0.18 \text{ Hz}$, as assumed in the previous section 5.1.

Comparisons of theory and experiment To compare the theoretical and experimental streamwise development of disturbances, the theoretical eigenfunctions were corrected once again in the same manner as Equation (5.5)

$$\tilde{u}'_{LST} = \frac{\tilde{u}}{\tilde{u}_{ref}} \cdot \frac{u'_{ref}}{u_e} \quad (5.7)$$

where experimental (u'_{ref}) and theoretical (\tilde{u}_{ref}) reference amplitudes were selected from the maximum values in wall-normal direction at 2.7 m , as indicated in Figure 5.12. The superscript tilde indicates that the independently calculated eigenfunctions are arranged in a streamwise direction by the e^N -method, as in Equation (5.6). Generally, because experimental disturbances evolve in a test facility, i.e., develop spatially, the spatial stability analysis should be performed for comparison with experimental results. However, as mentioned in Section 5.1, transforming the temporal growth rates into spatial ones using Gaster's transformation is acceptable for the present study. Moreover, the streaky layer in the present study is quasi-parallel to the streamwise direction (cf. Section 4.2) and the mode shapes of the theoretical eigenfunctions gradually evolve in a streamwise direction. This means that the mode shapes are less dependent on streamwise station. The e^N method is then used only to predict the streamwise growth of the theoretical eigenfunctions, but not for scaling of the experimental results. The experimental amplitudes have been measured using hot-film probes and comparisons in Figure 5.12 show how the measured amplitudes evolve compared to the theoretical predictions. Therefore, the temporal stability calculation with the e^N

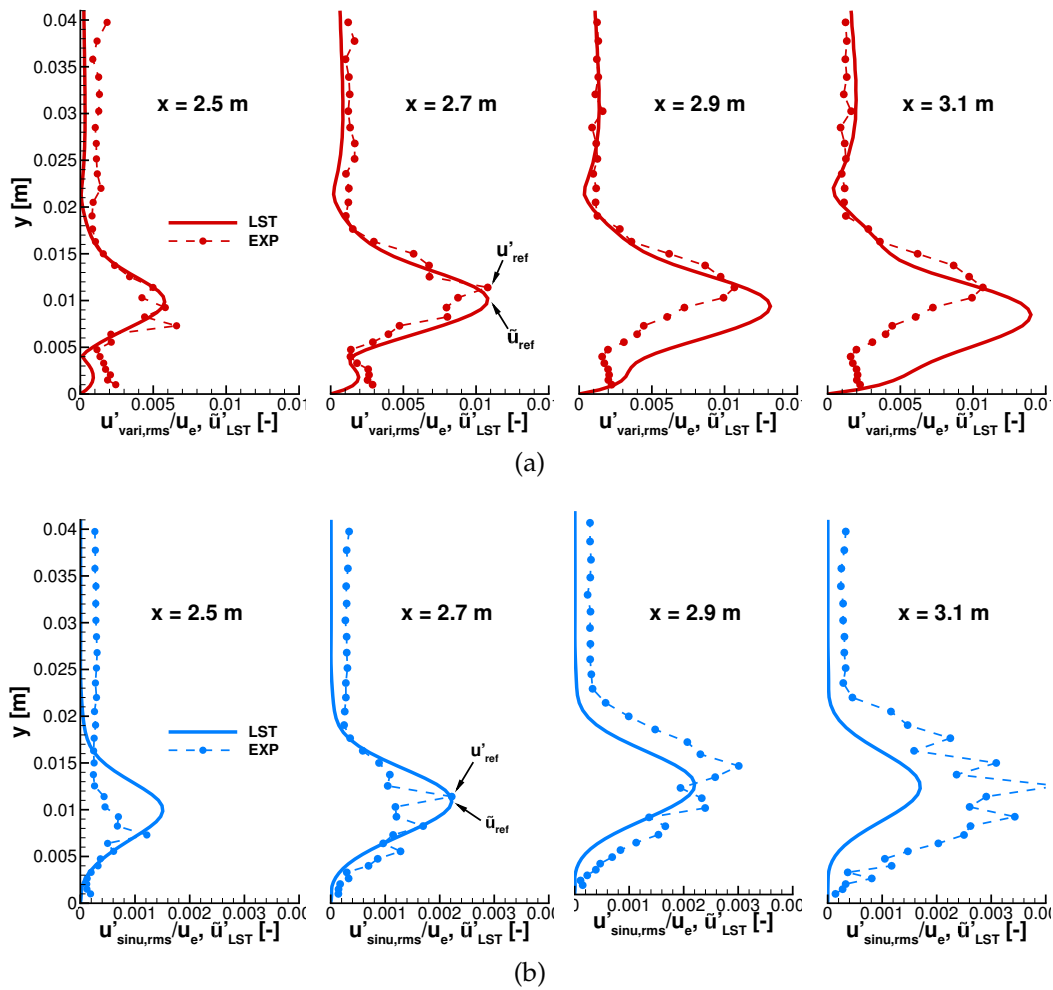


Figure 5.12: Theoretical (*solid line*) and experimental (*circle on dashed line*) disturbance amplitude profiles of (a) varicose and (b) sinuous mode. Arrows indicate positions in y -direction of theoretical and experimental reference amplitudes

method is appropriate for investigating the streamwise development of disturbances on the present streaky layer.

As a result, both mode shapes and magnitude of amplitudes of the experimental varicose mode show a good agreement with the theory at the first two streamwise positions closer to the roughness element $x = 2.5$ and 2.7 m (see Figure 5.12 (a)). The growth rate between these two streamwise positions is also reasonable. The decrease of the experimental amplitudes further downstream at $x = 2.9$ and 3.1 m is faster than theoretically predicted. The slight upward movement of the peak amplitude in wall-normal direction has already been observed in Figure 5.9 (a). In the upper part of the boundary-layer $y > 0.02$ m, the experi-

mental profiles remain constant at about $u'_{vari,rms}/u_e = 0.0015$, while the theoretical eigenfunctions are changing in the downstream direction. These values may imply experimental noise, rather than describing eigenfunctions, although they show a good agreement at $x = 2.9 m$.

Figure 5.12 (b) shows the sinuous mode. The experimental amplitude profile at $2.5 m$ is smaller, particularly at $y = 0.01 m$ where the varicose mode becomes quickly dominant owing to a strong wall-normal shear. After that, the sinuous mode grows faster than the varicose mode and fills up the deficiency at $x = 2.7 m$. However, a zig-zag pattern appears on the amplitude profile, which seems to imply that larger noise than modal amplitudes exists. It should be noticed once again that the present measurements were implemented in a *natural* manner without any spectral control and their amplitude versus time is less harmonic and includes irregular phase jumping, as already illustrated in Figure 5.6 (a). Further downstream at $x = 2.9$ and $3.1 m$, the experimental amplitudes grow continuously, in contrast to the gradual decaying of the theoretical amplitudes according to the eigenvalues as seen in Figure 5.3 (b). Deviation from the *linear* theoretical profiles may occur by experimental *nonlinear* growth, as mentioned in Chapter 4; the nonlinear behavior will be explored in the next chapter.

5.3 Asymmetric external forcing

As shown in the previous section, the varicose mode is dominant. Thus, the sinuous disturbances are much smaller than the varicose ones and their agreement with the theoretical results is less good in both mode shape and frequency. In addition, unavoidable experimental noise seems to interfere with clarification of the sinuous mode. To overcome these difficulties, an increase of the relative magnitudes of the sinuous amplitude was tried by forcing asymmetrical external disturbances. The experimental setup and operations were already introduced in Section 3.5, and the initially forced asymmetrical disturbances and comparisons

of forced eigenmodes with unforced natural ones are described in this section.

Forced initial disturbance The wake of the wire placed upstream of the leading edge (cf. Figure 3.9) is steady ($Re_D \approx 80$) such that the initial disturbances consist of a small streamwise velocity defect which is periodically moving back and forth in spanwise direction. Before reaching the leading edge, these disturbances are constant in wall-normal direction to the flat plate. When they enter the boundary-layer, they are stretched in streamwise direction. Thus, the initial disturbances contain a wide spectrum of streamwise and spanwise wave numbers due to their small spanwise extent compared to the amplitude of its displacement at the beginning. Moreover, some mechanical uncertainties with the traversing device can also lead to an unintended fuller frequency spectrum.

However, farther downstream the forcing signal develops into a quasi-harmonic signal with a dominant fundamental frequency ($f = 0.225 \text{ Hz}$) and some higher-harmonic ($f = 0.46 \text{ Hz}$) disturbances as seen in Figure 5.13 (a). It confirms that the forced signals are in true anti-phase as intended. Besides, Figure 5.13 (b) clearly shows a distinct growth of disturbances in the sinuous mode by asymmetric forcing in the free-stream flow. On the other hand, the figures concur-

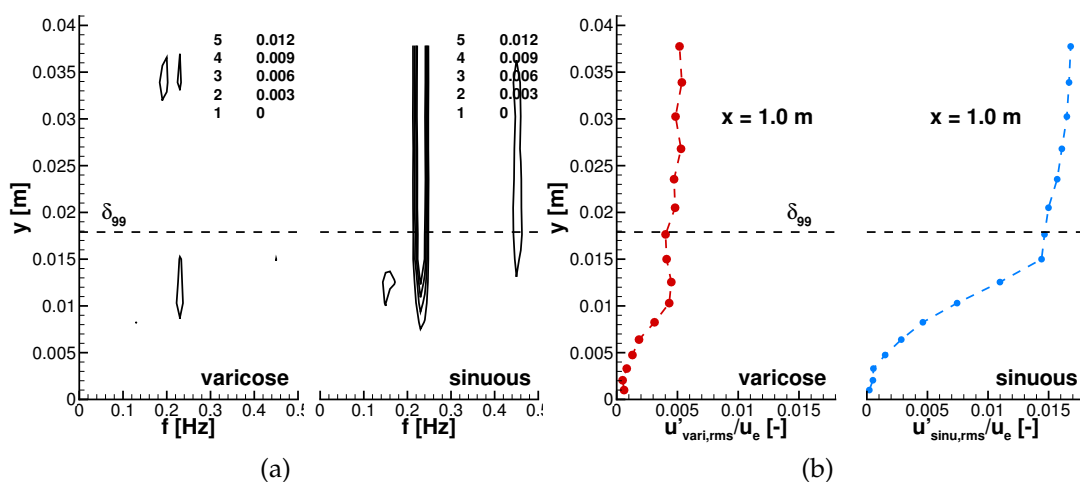


Figure 5.13: (a) Spectral distribution and (b) *rms*-value of varicose and sinuous forced disturbances at $x = 1.0 \text{ m}$. δ_{99} is the boundary-layer thickness of the Blasius flow

rently reveal that the forced disturbances do not penetrate into the boundary-layer (shear-sheltering effect). Moreover, disturbances ingested into the boundary-layer are damped upstream according to the LST. This should be considered carefully to interpret results farther downstream behind the roughness element.

Additionally, some noise is amplified in both the varicose and sinuous mode at around $f = 0.15 \text{ Hz}$. Interestingly, this frequency is close to that of the most unstable TS wave for a Blasius boundary layer at $x = 1.0 \text{ m}$. Thus, it could be supposed that a non-negligible varicose part in the wide spectrum of wave numbers is introduced by unavoidable mechanical difficulties of the external forcing for increasing the turbulence intensity in the free-stream. And some irregularity could also appear in the boundary-layer when the periodically forced disturbances encounter the leading edge of the flat plate. However, such agreement is coincidental because TS waves should excite varicose disturbances rather than sinuous ones. Thus, the reason for this unexpected additional frequency maximum is not yet clear.

Spectral comparison with unforced case In Figure 5.14, spectral distributions of the forced amplitudes are compared with the natural case, i.e., with and without the external forcing disturbances. Although the asymmetrical excitation only was forced, amplitudes of both varicose and sinuous mode in the boundary-layer are amplified concurrently. An increase of the varicose amplitudes can be observed in Figure 5.14 (a). At the first streamwise position near the element roughness $x = 2.5 \text{ m}$, the forced amplitudes seem very similar to the natural case. Further downstream, a larger growth of the amplitudes than in the natural case is observed. However, it is not as amplified as the sinuous mode, which needs higher contour levels than the natural case in Figure 5.14 (b). It should be emphasized that the amplitudes of the forced sinuous mode are centered around $f = 0.16 \text{ Hz}$, as in the natural case, despite the external input frequency of $f = 0.225 \text{ Hz}$. As seen previously, the external forcing disturbances are prevented by shear-shelter-

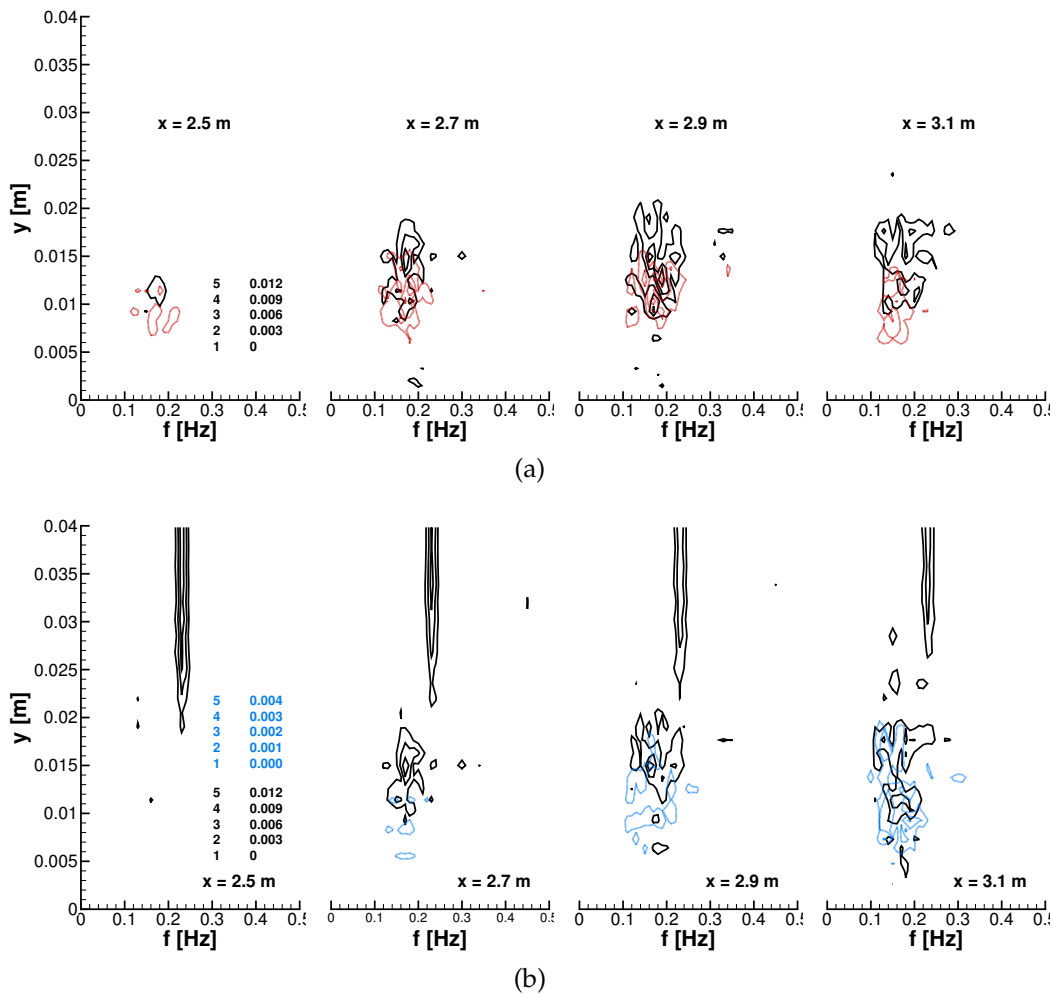


Figure 5.14: Comparison of forced amplitude (*black line*) by external disturbance input with natural case of (a) varicose (*red line*) and (b) sinuous (*blue line*) mode

ing from penetrating into the boundary-layer. Thus, the unstable eigenmode is dominated by flow-inherent characteristics.

Comparison of forced amplitudes with LST Comparisons of the forced disturbances with the theoretical eigenfunctions were performed in the same way as in the previous section. The forced disturbances were separated into varicose and sinuous parts, according to Equation (3.8), and their *rms*-valued amplitude profiles are depicted in Figure 5.15. Theoretical eigenfunctions were scaled by e^N -factors (cf. Equation (5.6)) once again to apply streamwise development of amplitudes and dimensionalized (cf. Equation (5.7)) by reference amplitudes, which are the maximum amplitudes in the boundary-layer at $x = 2.5 \text{ m}$, indicated in

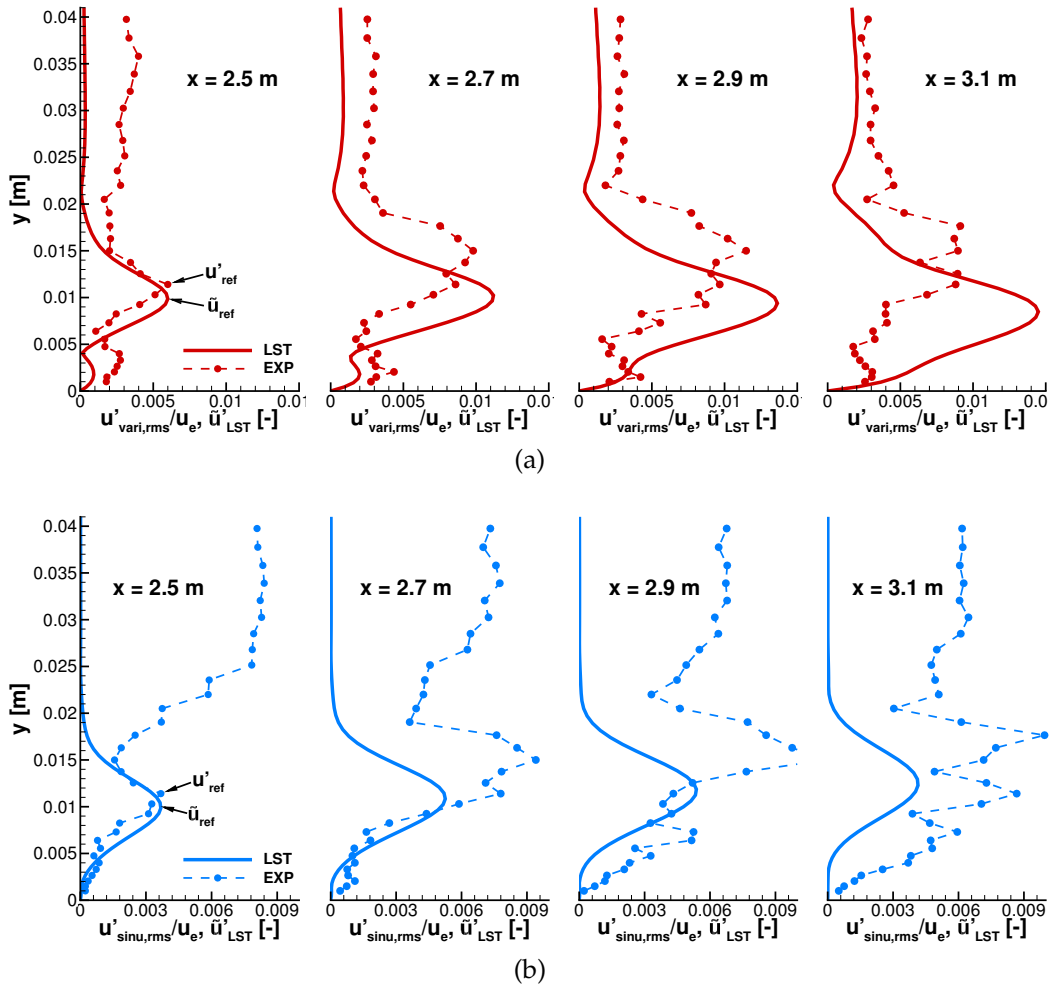


Figure 5.15: Comparisons of theoretical (*solid line*) and forced experimental (*circle on dashed line*) amplitude profiles of (a) varicose and (b) sinuous mode. Arrows indicate position in y -direction of theoretical and experimental reference amplitudes

Figure 5.15, for direct comparison with experimental results.

The varicose amplitudes are not considerably increased relative to the unforced case in Figure 5.12 (a), but amplitudes outside of the boundary-layer reach from about $u'_{sym,rms} = 0.001$ in the unforced mode up to about $u'_{sym,rms} = 0.003$. It seems that unexpected extra noise is added by the forcing mechanism. In comparison with the unforced case, the wall-normal peak of the forced amplitude profile starts at about $y = 0.01$ m at $x = 2.5$ m and moves further up and away from the eigenfunction's maximum in the downstream direction. More ruffled profiles than in the unforced case also imply an increased instability of the varicose mode

induced by the external asymmetric forcing.

The amplitudes of the forced sinuous mode are increased by a factor of about three in comparison to the unforced one in Figure 5.12 (b). In particular, a lack of amplitudes near $y = 0.01 \text{ m}$ at $x = 2.5 \text{ m}$ where the eigenfunctions are maximum is fully developed, as seen in Figure 5.15 (b). This implies that the sinuous mode can be artificially forced by an external disturbance input. In Figure 5.15 (b) the strong disturbance amplitudes in the free-stream, i.e., outside of the boundary-layer, are also seen, as like in Figure 5.14 (b). These large outer disturbances may become superposed with the inner-layer sinuous disturbances. Thus, the difference between theoretical and experimental profiles increases gradually in the downstream direction.

Chapter 6

Nonlinear Instability

6.1 Nonlinear secondary growth

Deviations of experimental disturbance profiles from the results of *linear* theory in the far-wake zone $x = 3.1 \text{ m}$ in Figure 5.12 raise the possibility of nonlinear growth of disturbances. Traces of the nonlinear secondary growth were also observed in Chapter 4 by ragged velocity profiles (see at $x = 3.5 \text{ m}$ in Figures 4.2 and 4.3), with disturbances concentrated in the lower frequency area (see Figures 4.2 (c) and 4.3 (c)). Such a lower-frequency unstable behavior can be observed in the perturbation velocity signal in Figure 6.1. In comparison with the signal at $x = 2.7 \text{ m}$ in Figure 5.6 (a), the disturbances in the far-wake zone $x = 3.1 \text{ m}$ oscillate with distinctly larger amplitude in a longer time duration.

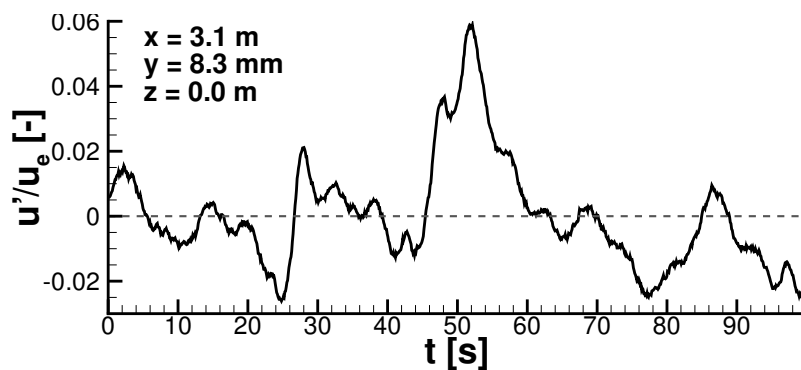


Figure 6.1: Time signal of streamwise disturbance containing nonlinear instability in the far-wake zone

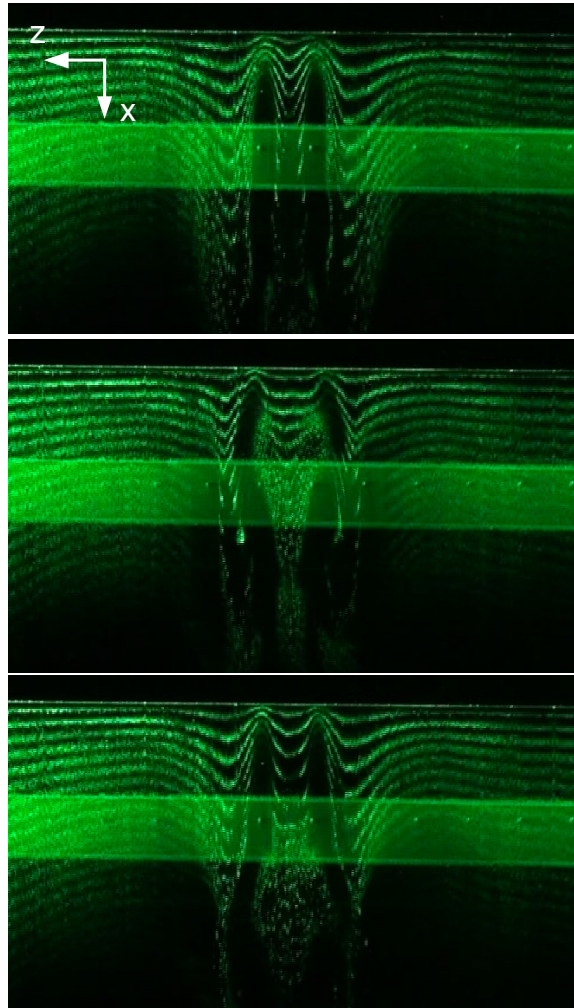


Figure 6.2: Successive ($\Delta t = 1$ s) video shots of nonlinear evolution of streaks. Cathode wire at $y = h = 8.3$ mm and $x = 3.0$ m. There is no relation with the velocity signal in Figure 6.1

The flow behavior in the far-wake zone was visualized by timelines using the hydrogen-bubble method (cf. Section 3.3), as depicted in Figure 6.2. A newly formed high-speed streak is observed in the middle of the first picture. Initially, a low-speed streak from separation was located here, as seen in Section 4.2. A continuous velocity increase by spanwise vorticity associated with the wall-normal high shear layer, which pulls down upper high-speed fluid and pushes up low-speed fluid, forms the high-speed streak in the downstream direction. In the far-wake zone, the spanwise vorticity becomes stronger, and a low-speed bulging lump, which appears as collapsed timelines on the second picture in Figure 6.2, occurs periodically. An instantaneous velocity field describing the low-

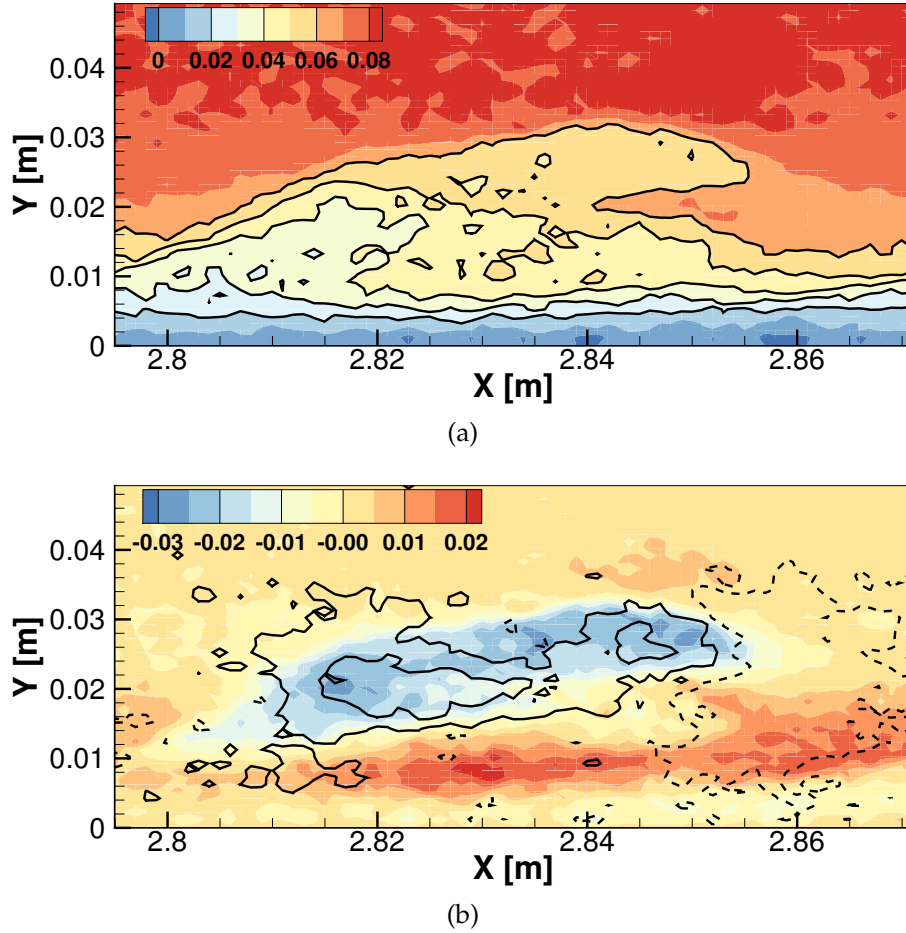


Figure 6.3: (a) An instantaneous velocity field of PIV measurements with a velocity increment (*solid lines*) $\Delta u = 0.01 \text{ m/s}$ from $u = 0.02$ to 0.06 m/s (b) velocity deviation $u' = u - u_{avg}$ (*color*) and positive (*solid*) and negative (*dashed line*) vertical velocity component $v' = v - v_{avg}$ with an increment $\Delta v' = 0.008 \text{ m/s}$ from $v' = -0.003$ to 0.013 m/s

speed bulging lump was captured by PIV measurements in Figure 6.3 (a). In order to obtain unsteady fluctuations, the velocity field is subtracted by an averaged velocity field with 50 successive captures in a time interval $\Delta t = 1.0 \text{ s}$, as shown in Figure 6.3 (b). As a result of spanwise vorticity, the bulging lump consists of lifted-up negative perturbations following brought-down positive ones. This nonlinear behavior is consistent with the fundamental varicose mode (cf. Figure 5.5). A wavy motion, which is a typical behavior of secondary instability of streamwise streaks induced by either suction or high free-stream turbulence (Schmid and Henningson, 2000) is not observed. This means that the secondary instability of the streaky flow induced by a three-dimensional roughness element

is dominated by the fundamental varicose mode.

6.2 Breakdown

The breakdown of the streaky flow induced by a three-dimensional roughness element was triggered by increasing the free-stream velocity to $u_e = 0.1 \text{ m/s}$, i.e., an over-critical Reynolds number $Re_h = 456$. For depicting the three-dimensional flow structures in the breakdown process, a hydrogen-bubble carpet was adopted and illuminated by both a DPSS laser and a halogen lamp. Detailed setup and operation can be found in Section 3.3.

Temporal changes in a period of the vortical structures are analyzed in four time steps illustrated on (y, z) -planes (left side of Figure 6.4). At first, at $t = 0.0 \text{ s}$, a straight line is bent by strongly rotating vortices. It seems that high- (lower part) and low-speed streaks (upper part) are tipped downward and upward, respec-

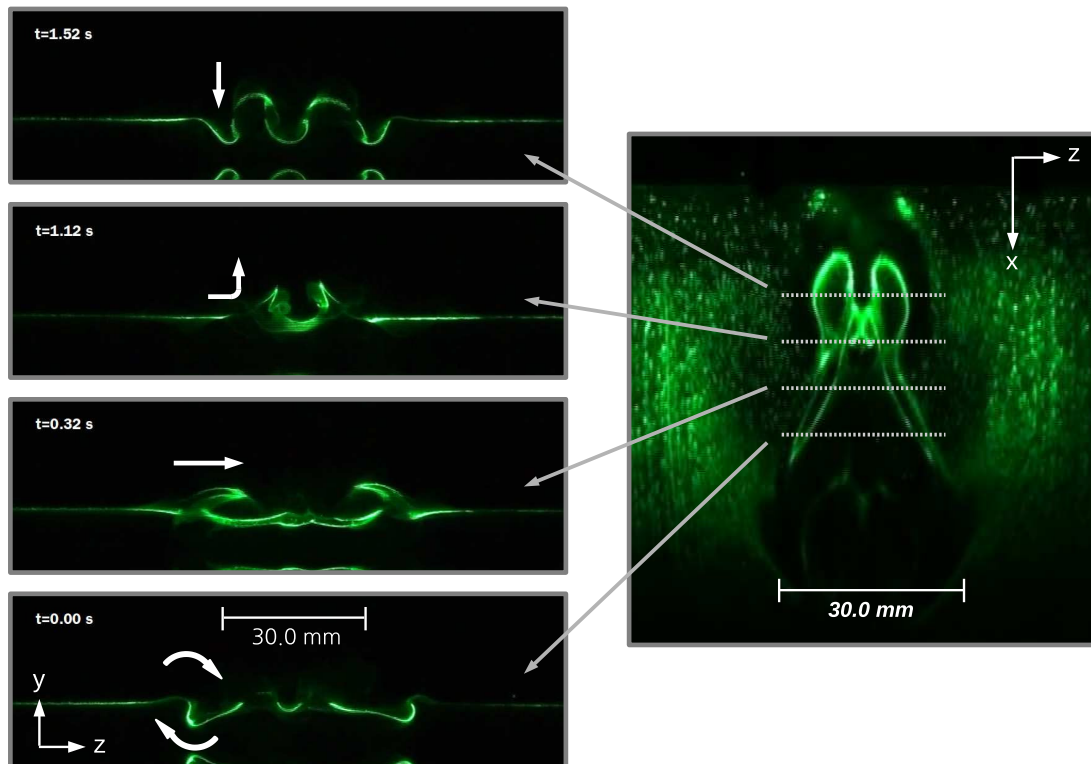
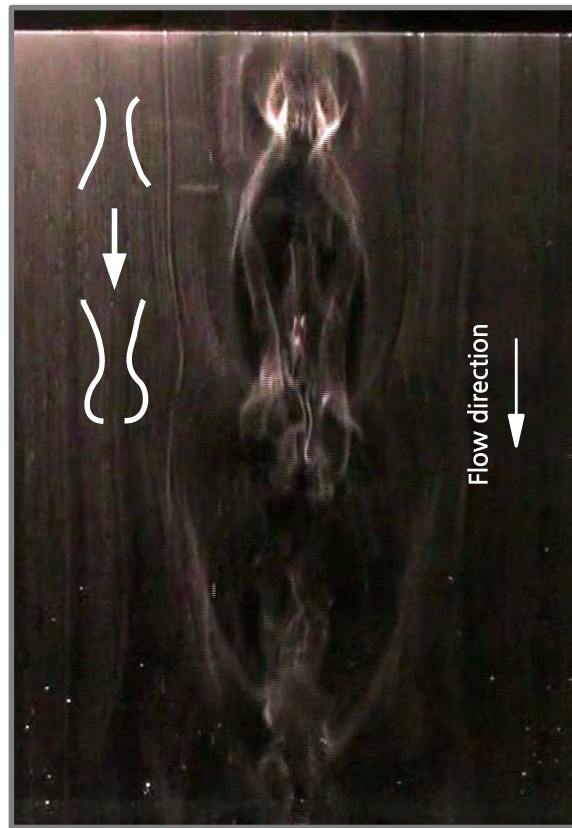


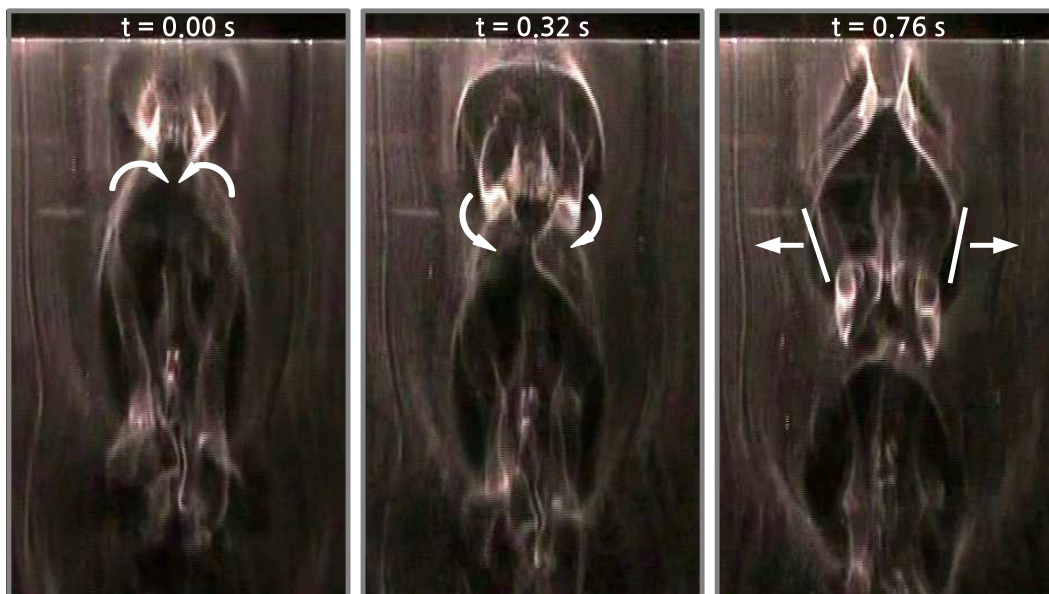
Figure 6.4: Decomposition of a three-dimensional vortical structure ((x, z) -plane on right side) at $x = 2.6 \text{ m}$ and $y = 8.3 \text{ mm}$ into four time steps ((y, z) -planes on left side)

tively. The upper parts (low-speed streaks) are shifted into the middle ($t = 0.32$ s), and such two parts from left and right side collide against each other in the middle ($t = 1.12$ s) and finally break down at $t = 1.52$ s. A two-dimensional cross-cut on a (x, z) -plane at $y = 8.3$ mm (on the right side of Figure 6.4) describes these whole processes as a butterfly-like structure, which flows periodically in a downstream direction.

Figure 6.5 shows a spatial development of these vortical structures further downstream. Three-dimensional structures in a longer distance can be illuminated by a halogen lamp. In Figure 6.5 (a), the butterfly-like vortex structure is also found and followed successively by a hairpin vortex. This transformation of vortex structures was decomposed in three time steps in Figure 6.5(b). At first, at $t = 0.0$ s, the low-speed velocity parts that are rolled and lifted up from both left and right side, meet in the middle, as explained in Figure 6.4. They are facing upstream higher velocity components and then rolling with respect to the spanwise coordinate ($t = 0.32$ s). This part forms into the head of the hairpin vortex and a following streamwise elongation of the rotating head of the vortex becomes the feet of the hairpin vortex ($t = 0.76$ s). The feet of the vortices spread out in a spanwise direction and enlarge the turbulent flow area further downstream. In this way, successively formed hairpin vortices flow in a downstream direction (Figure 6.6), and a laminar-turbulent transition is finally triggered (not shown here).



(a)



(b)

Figure 6.5: (a) Evolution from butterfly-like structure to hairpin vortex (b) time steps to hairpin vortex

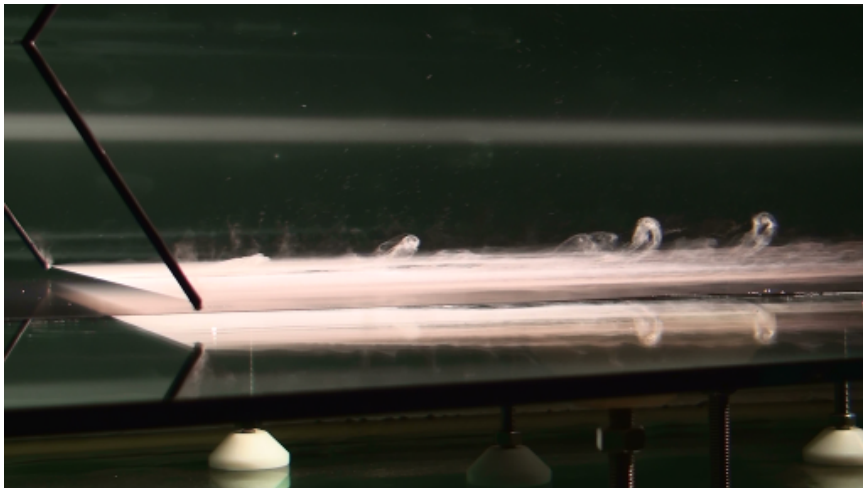


Figure 6.6: Side view of successively following hairpin vortices visualized by hydrogen-bubble carpet

Chapter 7

Summary and Conclusions

In the present study, the stability of a streaky boundary-layer induced by a \cos^3 -shaped roughness element has been investigated. For the underlying base flow, a numerical CFD calculation with a laminar solver and time-averaged experimental measurements using a hot-film method were performed in the laminar water channel (LWK) at the Institut für Aerodynamik und Gasdynamik (IAG), University of Stuttgart. Negative velocity components resulting from separation were measured by a mono-PIV system. As a result, a steady streaky layer consisting of high- and low-speed streaks in its wake was found. The high-speed streaks were generated by the lift-up mechanism based on streamwise counter-rotating vortices that arise on both flanks of the roughness element. The low-speed streak that appeared in the plane of symmetry originates from a flow separation behind the element.

Such a three-dimensional streaky boundary-layer generated by a roughness element gives rise to many unstable eigenmodes according to bi-global LST. Two highly unstable eigenmodes, which respectively oscillate symmetrically and asymmetrically with respect to the symmetric plane in the middle, were identified and accordingly termed the varicose and sinuous modes. The varicose amplitudes are perturbed by wall-normal velocity gradients of the streaky layer. The asymmetrical nature of the sinuous amplitudes is caused by opposite signs of the

spanwise velocity gradient and is responsible for a wavy motion of the streaks. In other words, these two most unstable modes belong to each shear layer in wall-normal and spanwise directions.

The present study mostly focused on experimental investigations for confirming the existence of these unstable modes in practical flow and for analysing their instability. Experimental disturbances, which consist of mixed disturbances, originated in two different ways, i.e., by wall-normal and spanwise shear layers, respectively, were acquired by two simultaneously operating hot-film probes, and separated into a varicose and a sinuous part. Comparisons with theoretical eigenfunctions showed a good agreement in general. The varicose mode based on a high shear layer first dominates the sinuous one, after which a continuous increase of the sinuous mode is observed in the far-wake zone, whereas the varicose amplitudes gradually decrease.

Owing to a relatively low signal-to-noise ratio, the sinuous mode is more susceptible to measurement errors. For this reason, forcing asymmetrical amplitudes in the free-stream were tried in order to amplify the sinuous mode. The sinuous mode was enhanced about three times compared to the unforced case and revealed amplitude profiles closer to the eigenfunction predicted by linear stability theory. However, shear sheltering prevents the external disturbances from entering the boundary layer. Hence, only amplitudes of the eigenmode were amplified in the boundary-layer, but an unintentional mismatch of forcing frequency occurs. Consequently, a separate forcing for a specific eigenmode has been achieved by external disturbances, confirming that the sinuous disturbances for the present experimental set-up are an eigenfunction of the streaky laminar base flow. However, this has been only a preliminary test, and a new careful method for forcing the sinuous mode is required to control directly inner boundary-layers and to amplify the sinuous mode at an exact frequency.

Farther downstream, the streaky layer started nonlinear secondary growth and exhibited a motion like the fundamental varicose mode. This indicates that

fundamental instability of the streaky boundary-layer induced by a roughness element is dominated by the varicose mode. A breakdown process under an over-critical condition $Re_h = 456$ was explored by observing the vortical structures of the nonlinear streaky layer that evolve into hairpin vortices.

Appendix A

Technical Data

Table A.1: Laminar water channel

Channel type	Closed return channel
Construction	Fiberglass-sandwich construction
Flow medium	Water (softened)
Water conditioning	Ion exchanger; Chlorination; Bypass filtration with filter 10, 2.5, 1.2, 0.2 μm
Power section	2 counter-rotating axial pumps with asymmetrical blade; Power transmission pro flywheel (400 kg) and drive belt; RPM-regulated motor (2.3 kW)
Rectifier	2 honeycomb rectifiers at diffuser entrance
Diffuser	10 m long diffuser with angle change $5.9^\circ \rightarrow 5.0^\circ$
Nozzle	Three-dimensional contraction (7.7 : 1) by free water surface
Calming section	3 10x textile screens (crosswise) and 1 precision screen (steel single wire, $\varnothing 0.1/mm$)
Test section	$1.2 \times 0.5 \times 10$ m, 3 glass walls and a free water surface
Vibration isolation	Air sleeve footing. Rubber sleeve for transmission components and drive belt for motor

Thermal isolation	Room on basement with heat-insulating walling. All components are constructed by heat-insulating sandwich-material
Temperature stability	$< 0.05 \text{ }^\circ\text{C/day}$
Velocity range	$0.05 \sim 0.2 \text{ m/s}$
Turbulent intensity $Tu = \sqrt{u'^2}$	$< 0.05 \%$ ($0.10 \sim 10 \text{ Hz}$) and $< 0.15 \%$ ($0.01 \sim 10 \text{ Hz}$) by free-stream velocity $u_e = 0.15 \text{ m/s}$

Table A.2: PIV system

Seeding particle	Type	Nylon-Particle (Toray SP-500)
	Specific weight	$\rho = 1.02 \text{ g/cm}^3$
	Diameter	$5 \text{ }\mu\text{m}$
Laser sheet	Laser type	Double pulse Nd:YAG (Quantel Brilliant Twins)
	Energy	150 mJ/pulse
	Wave length	532 nm
	Pulse duration	4 ns
	Repetition rate	10 Hz
Camera	type	CCD, SVGA sensor (0.12 mm/px)
	Resolution	$1280 \times 1024 \text{ px}$
	Pixel size	$6.7 \mu\text{m}$
	Discretization	12 bit
	Lens focal length	50 mm
	Objective	Nikkor 1 : 1.4
	min. time duration	$1 \text{ }\mu\text{s}$

Appendix B

Installation of the Flat Plate in the Test Section

The entire length of the flat plate in the test section of the LWK is 8 m and consists of six glass plates whose length is respectively either 1.0 or 1.5 m with a thickness 8 mm. The first plate has an elliptical nose with a ratio 10 : 1 by which the excess velocity near the leading edge is kept as low as possible. Figure B.1 (a) shows a streamline flowing over the leading edge with no detachment at the installed nose plate.

The edges of the glass plates are chamfered to prevent a chipping off (see

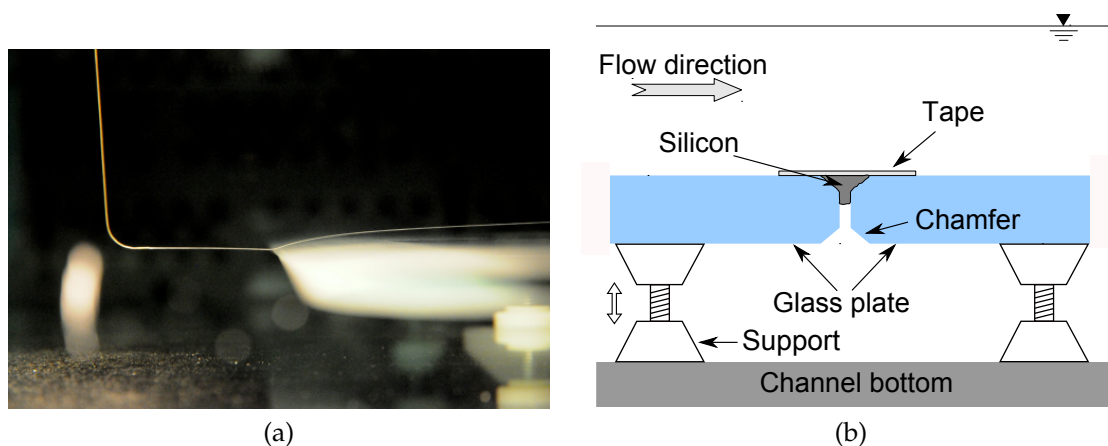


Figure B.1: (a) Streamline flowing over the elliptic leading edge (b) packing junction between two plates with chamfers

Figure B.1 (b)). This results in a wedge-shaped slot at the joint on both upper and lower part of the plates. These slots were filled up with silicon and sealed by adhesive tape with a 0.05 *mm* thickness. The tape is useful for compensating the unevenness of the soft silicone. The influence of 0.05 *mm* thickness of the tape can be neglected in view of the boundary-layer thickness which is at least 2 orders thicker. In the same manner, the roughness element model was mounted on the middle of the glass plate.

Because of the flexibility of the *glass* plates, they are bending on the supports. By a careful controlling of the height of each support, the six glass plates could be aligned in parallel with each other. The slope angle of the whole connected plate was calculated by measuring the heights from the bottom of the plate up to the water surface at every 1 *m* in streamwise direction. The maximum tilt angle was 0.029 °.

Flow visualization The installation of the glass flat plates was validated qualitatively by a flow visualization method using the dye-streak technique of Hoyt and Sellin (1995). To retain the dye-streak over a long running track, a liquid mixture having attributes of shear thickening and high extensional viscosity has been used. Its recipe is

2 % C₁₆TASal 50 *ml*

0.5 % PEG 25 *ml*

Tap water 100 *ml*

White Paint 1 *ml*.

The surfactant solution (2 % C₁₆TASal) for the shear thickening consists of the same amount of hexadecyltrimethylammonium bromide (C₁₉H₄₂B₂N) and sodium salicylate (C₇H₅NaO₃). PEG (polyethylene glycol, HO(C₂H₄O)_n) is known as a drag reducing additive. Because the solutions are initially colorless, a small amount of conventional white emulsion paint was added as a dye.



Figure B.2: Flow visualizations of laminar-turbulent transition on the flat plate by dye-streaks observed in (a) spanwise direction (b) wall-normal direction. (a) and (b) were captured independently

Figure B.2 shows the visualized laminar-turbulent transition on the newly installed flat plate as explained above. Up to $x = 4.0$ m, the flow remained stable. At the streamwise position $x = 4.5$ m from the leading edge, the dye-streak is swinging slightly in the spanwise direction, and at $x = 5.0$ m the oscillation is seen clearly. It is notable that the flow is swinging earlier in the spanwise direction than in the wall-normal direction. The flow is still laminar up to here. At $x = 5.5$ m, a deflection of the flow can be seen and the flow becomes fully

turbulent at $x = 6.0$ and 6.5 m.

The free-stream velocity was measured by an optical method. A little white ball was dropped on the water surface and filmed by a digital camera. 6 successive images of the flowing ball were captured and measured each moved distance using an image-editing software. A time duration was obtained from a fixed filming frequency of the camera. Calculation of the free-stream velocity was repeated 9 times and the averaged velocity was $u_e = 0.133$ m/s. So, the corresponding Reynolds number at $x = 5.5$ m is

$$\text{Re}_x = \frac{xu_e}{\nu} \approx 700000 \quad (\text{B.1})$$

where, $\nu = 1.0 \times 10^{-6}$ m²/s is a kinematic viscosity of water at 20 °C. In previous measurements of Wiegand (1996) conducted in the same LWK, a distinct kink in the velocity profile that resulted from a strong growth of the displacement thickness of a developed turbulent boundary layer was found at $x = 5$ m ($\text{Re}_x = 725000$ with a free-stream velocity $u_e = 0.145$ m/s). Therefore, it can be concluded from the comparison of the critical Reynolds numbers that a required quality for a laminar boundary-layer flow was achieved on the current installation of the glass flat plate.

Appendix C

Calibration of the CTA System with Hot-film Probe

Setup and calibration of the CTA system using hot-film probes for the present study were principally performed by following the manufacturer's instruction manual (Dantec, 1983). This appendix introduces some specifics at the LWK during the calibration procedure. Other experimental parameters were selected mostly from the previous work of Wiegand (1996) who studied the stability of TS waves in the same way as in the present study by the CTA method using a hot-film.

Probe resistance and overheat adjustment To sensitively catch the changes of temperature inside the flow, an over-heating temperature of the hot-film sensor is applied by an overheat adjustment which is calculated based on the resistance of the sensor. To measure the resistance, first of all, the entire circuit resistance R_{TOT} and the cable resistance R_C are measured by a measuring function on the *Dantec 15C17* CTA bridge component. A probe lead resistance R_L is indicated on the probe container by the manufacturer. Accordingly, the sensor resistance is

calculated as $R_0 = R_{TOT} - (R_C + R_L)$. An overheat ratio $a = 5\%$ is applied

$$R = (1 + a)R_0 \quad (C.1)$$

and a new total resistance is obtained

$$R_{TOT(HOT)} = R + (R_C + R_L). \quad (C.2)$$

This resistance is inserted into the CTA bridge again and the sensor is now heated.

By the overheat ratio $a = 5\%$, the temperature of the sensor

$$T_{sensor} = T_0 + \frac{R - R_{20}}{\alpha_{20}R_{20}} \quad (C.3)$$

$R_{20} = \text{Sensor resistance at } T_0 = 20^\circ\text{C} [\Omega]$

$\alpha_{20} = \text{Temperature coefficient of sensor at } T_0 = 20^\circ\text{C} [\%/^\circ\text{C}]$

reaches between $T_{sensor} = 30 \sim 35^\circ\text{C}$ for an operating temperature and a bubble formation around the probe that occurs when the temperature exceeds 60°C (Wiegand, 1996) could be prevented.

Calibration curve The CTA bridge outputs continuous temperature changes on the heated sensor as an electric signal of voltages. To transform the magnitude of voltage into velocity, a calibration curve obtained as below has been used. Firstly, a hot-film probe combined with a probe support was located at $x = 1.0\text{ m}$ from the leading edge and in the spanwise middle at $z = 0.0\text{ m}$. The location of the probe was selected $y = 7.5\text{ cm}$ which is the middle from the bottom plate to free water surface. Then, free-stream velocities in the test section were controlled by stepwise increasing the pump frequency of the LWK from $f = 0.0\text{ Hz}$ for an initial zero velocity until $f = 19.0\text{ Hz}$ with increments either $\Delta f = 1$ or 2 Hz . This increasing

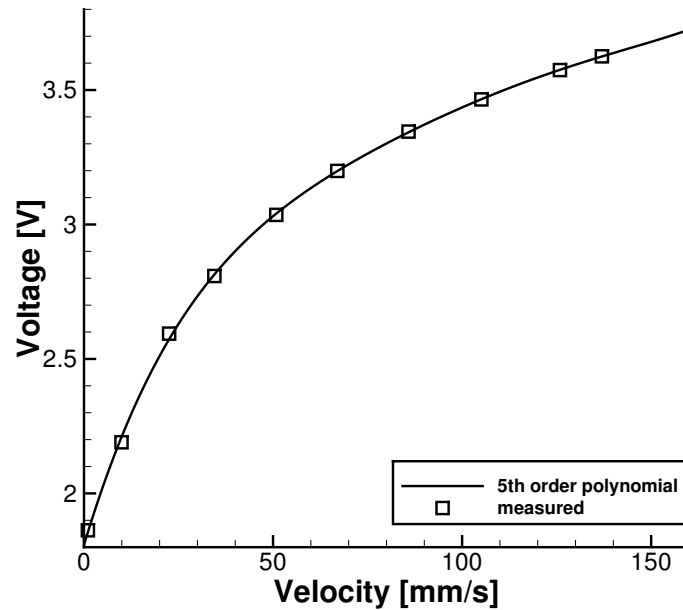


Figure C.1: Calibration curve fitted by 5th order polynomial

order from lower to higher velocity enables to regulate the velocity changes in the whole channel faster and stabler than contrariwise (cf. Wiegand (1996)). Additionally, a sufficient waiting time is needed for a uniformity of the flow after every velocity increase. The velocities for comparing with output voltages from the CTA bridges were measured by a hydrogen-bubble method (cf. Section 3.3). Successive time lines consisting of hydrogen bubbles were captured by a digital camera. Distances between the bubble lines (Δx) obtained by a graphic software were calculated for velocities with a pulse duration time (Δt) of the time lines. A single particle method had been also used to measure the free-stream velocity. A small particle is laid on the free-water surface in the channel and its moving distance and time are taken by an USB digital camera in perpendicular direction. Finally, a calibration curve was fitted by 5th order polynomial as illustrated in Figure C.1.

Unless either the measuring equipments are replaced or water temperature changes in a large range, the calibration curve can be used continuously. To reflect a small changes of water temperature after the calibration, the probe resistance R_0 has been measured every day before the measurements and a new circuit

resistance $R_{TOT(HOT)}$ with the over heat 5 % was inserted. For a thermal stability of the CTA bridge, a warming time was set 2 hours after switch-on of the devices on every day.

Bibliography

- ACARLAR, M. S. AND SMITH, C. R. 1987. A study of hairpin vortices in a boundary layer. Part 1. Hairpin vortices generated by a hemisphere protuberance. *J. Fluid Mech.* 175, 1–41.
- ANDERSSON, P., BERGGREN, M., AND HENNINGSON, D. S. 1999. Optimal disturbances and bypass transition in boundary layers. *Phys. Fluids* 11, 1, 134–150.
- ANDERSSON, P., BRANDT, L., BOTTARO, A., AND HENNINGSON, D. S. 2001. On the breakdown of boundary layer streaks. *J. Fluid Mech.* 428, 29–60.
- BRUUN, H. H. 1995. *Hot-wire anemometry, principles and signal analysis*. Oxford University Press.
- BUTLER, K. M. AND FARRELL, B. F. 1992. Three-dimensional optimal perturbations in viscous shear flow. *Phys. Fluids* 8, 1637–1650.
- CHOUDHARI, M. AND FISCHER, P. 2005. Roughness-Induced Transient Growth. In *35th AIAA Fluid Dyn. Conf. Exhib.* AIAA 2005-4765. Toronto, Ontario Canada.
- COSSU, C. AND BRANDT, L. 2004. On Tollmien–Schlichting-like waves in streaky boundary layers. *Eur. J. Mech. - B/Fluids* 23, 815–833.
- DANTEC. 1983. Instruction manual 56C17 CTA bridge. Ph.D. thesis, Dantec documentation department.
- DANTEC. 2005. *Probes for hot-wire anemometry*. Dantec Dynamics.

- DENISSEN, N. A. AND WHITE, E. B. 2013. Secondary instability of roughness-induced transient growth. *Phys. Fluids* 25, 11, 114108.
- DUCHMANN, A., GRUNDMANN, S., AND TROPEA, C. 2013. Delay of natural transition with dielectric barrier discharges. *Exp. Fluids* 54, 1461.
- ELOFSSON, P. A., KAWAKAMI, M., AND ALFREDSSON, P. H. 1999. Experiments on the stability of streamwise streaks in plane Poiseuille flow. *Phys. Fluids* 11, 4, 915–930.
- ERLEBACHER, G. AND HUSSAINI, M. 1991. Nonlinear evolution of a second-mode wave in supersonic boundary layers. *Appl. Numer. Math.* 7, 1, 73–91.
- FRANSSON, J. H. M., BRANDT, L., TALAMELLI, A., AND COSSU, C. 2004. Experimental and theoretical investigation of the nonmodal growth of steady streaks in a flat plate boundary layer. *Phys. Fluids* 16, 10, 3627–3638.
- FRANSSON, J. H. M., BRANDT, L., TALAMELLI, A., AND COSSU, C. 2005. Experimental study of the stabilization of Tollmien–Schlichting waves by finite amplitude streaks. *Phys. Fluids* 17, 054110.
- FRANSSON, J. H. M. AND TALAMELLI, A. 2012. On the generation of steady streamwise streaks in flat-plate boundary layers. *J. Fluid Mech.* 698, 211–234.
- FRANSSON, J. H. M., TALAMELLI, A., BRANDT, L., AND COSSU, C. 2006. Delaying transition to turbulence by a passive mechanism. *Phys. Rev. Lett.* 96, 064501.
- FRIEDERICH, T. AND KLOKER, M. J. 2012. Control of the secondary cross-flow instability using localized suction. *J. Fluid Mech.* 706, 470–495.
- GREEN, J. E. 2008. Laminar flow control – Back to the future ? In *38th Fluid Dyn. Conf. Exhib.* AIAA 2008-3738. Seattle, Washington.

- GROSKOPF, G., KLOKER, M. J., AND MARXEN, O. 2008. Bi-global secondary stability theory for high-speed boundary-layer flows. In *Proc. Summer Progr. 2008*. Center for Turbulence Research, Stanford University, 55–72.
- GROSKOPF, G., KLOKER, M. J., STEPHANI, K. A., AND MARXEN, O. 2010. Hypersonic flows with discrete oblique surface roughness and their stability properties. In *Proc. Summer Progr. 2010*. Center for Turbulence Research, Stanford University, 405–422.
- HACK, M. J. P. AND ZAKI, T. A. 2014. Streak instabilities in boundary layers beneath free-stream turbulence. *J. Fluid Mech.* 741, 280–315.
- HERBERT, T. 1988. Secondary instability of boundary layers. *Annu. Rev. Fluid Mech.* 20, 487–526.
- HERZOG, F. M. 2013. Bachelorarbeit. Ph.D. thesis, Universität Stuttgart.
- HOYT, J. AND SELLIN, R. 1995. A turbulent-flow dye-streak technique. *Exp. Fluids* 20, 38–41.
- JOSLIN, R. D. AND GROSCH, C. E. 1995. Growth characteristics downstream of a shallow bump: Computation and experiment. *Phys. Fluids* 7, 12, 3042–3047.
- KACHANOV, Y. S. 1994. Physical mechanisms of laminar-boundary-layer transition. *Annu. Rev. Fluid Mech.* 26, 411–482.
- KACHANOV, Y. S. AND LEVCHENKO, V. Y. 1984. The resonant interaction of disturbances at laminar-turbulent transition in a boundary layer. *J. Fluid Mech.* 138, 209–247.
- KENDALL, J. 1981. Laminar boundary layer velocity distortion by surface roughness: Effect upon stability. *AIAA Pap.* 81–0195.
- KLEBANOFF, P. S., TIDSTROM, K. D., AND SARGENT, L. M. 1962. The three-dimensional nature of boundary layer instability. *J. Fluid Mech.* 12, 1–34.

- KLOKER, M. J. 2008. Lecture material. Ph.D. thesis, Universität Stuttgart.
- KOCH, W., BERTOLOTTI, F. P., STOLTE, A., AND HEIN, S. 2000. Nonlinear equilibrium solutions in a three-dimensional boundary layer and their secondary instability. *J. Fluid Mech.* 406, 131–174.
- LANDAHL, M. 1980. A note on an algebraic instability of inviscid parallel shear flows. *J. Fluid Mech.* 98, 243–251.
- LANG, M., RIST, U., AND WAGNER, S. 2004. Investigations on controlled transition development in a laminar separation bubble by means of LDA and PIV. *Exp. Fluids* 36, 1 (Jan.), 43–52.
- LEHOUCQ, R. B., SORENSEN, D. C., AND YANG, C. 1998. *ARPACK Users' Guide : Solution of Large Scale Eigenvalue Problems with Implicitly Restarted Arnoldi Methods*. SIAM.
- LUCHINI, P. 2000. Reynolds-numbers-independent instability of the boundary layer over a flat surface : optimal perturbations. *J. Fluid Mech.* 404, 289–309.
- MATSUBARA, M. AND ALFREDSSON, P. H. 2001. Disturbance growth in boundary layers subjected to free-stream turbulence. *J. Fluid Mech.* 430, 149–168.
- MORKOVIN, M. V. 1968. Critical evaluation of transition from laminar to turbulent shear layers with emphasis to hypersonically travelling bodies. *AFFDL-TR-68-149*.
- MORKOVIN, M. V. 1985. Bypass transition to turbulence and research Desiderata. In *Transit. Turbine, NASA Conf. Publ.* 2386. 161–204.
- PIOT, E., CASALIS, G., AND RIST, U. 2008. Stability of the laminar boundary layer flow encountering a row of roughness elements: Biglobal stability approach and DNS. *Eur. J. Mech. - B/Fluids* 27, 6, 684–706.

- PRANDTL, L. 1904. Über Flüssigkeitsbewegungen bei sehr kleiner Reibung. In *Verhandlg. III. Intern. Math. Kongr. Heidelberg*, 484–491.
- RAFFEL, M., WILLERT, C. E., WERELEY, S. T., AND KOMPENHANS, J. 2007. *Particle Image Velocimetry, A Practical Guide*, 2nd ed. Springer.
- RAYLEIGH, J. 1880. On the stability, or instability, of certain fluid motions. *Proc. London Math. Soc.* 11, 57–72.
- RESHOTKO, E. 2001. Transient growth: A factor in bypass transition. *Phys. Fluids* 13, 5, 1067–1075.
- RESHOTKO, E. AND LEVENTHAL, L. 1981. Preliminary experimental study of disturbances in a laminar boundary layer due to distributed roughness. *AIAA Pap.* 81–1224.
- REYNOLDS, O. 1883. An experimental investigation of the circumstances which determine whether the motion of water shall be direct or sinuous, and of the law of resistance in parallel channels. *Phil. Trans. Roy. Soc. Lond.* 174, 935–982.
- RICCO, P., LUO, J., AND WU, X. 2011. Evolution and instability of unsteady nonlinear streaks generated by free-stream vortical disturbances. *J. Fluid Mech.* 677, 1–38.
- RIST, U. AND FASEL, H. 1995. Direct numerical simulation of controlled transition in a flat-plate boundary layer. *J. Fluid Mech.* 298, 211–248.
- RIZZETTA, D. P. AND VISBAL, M. R. 2007. Direct Numerical Simulations of Flow Past an Array of Distributed Roughness Elements. *AIAA J.* 45, 8 (Aug.), 1967–1976.
- SCHLICHTING, H. 1933. Zur Entstehung der Turbulenz bei der Plattenströmung. *Nachr. Ges. Göttingen, Math. Phys. Klasse*, 182–208.

- SCHLICHTING, H. AND GERSTEN, K. 2000. *Boundary-Layer Theory*, 8th ed. Springer-Verlag.
- SCHMID, P. J. 2007. Nonmodal Stability Theory. *Annu. Rev. Fluid Mech.* 39, 129–162.
- SCHMID, P. J. AND HENNINGSON, D. S. 2000. *Stability and Transition in Shear Flows*. Springer-Verlag.
- SCHRAUF, G. 2005. Status and perspectives of laminar flow. *Aeronaut. J.* 109, 1102, 639–644.
- SCHUBAUER, G. B. AND SKRAMSTAD, H. K. 1943. Laminar-Boundary-Layer Oscillations and Transition on a Flat Plate. *NACA Adv. Confid. Rep.* 909, 327–357.
- SHAHINFAR, S., SATTARZADEH, S. S., FRANSSON, J. H. M., AND TALAMELLI, A. 2012. Revival of Classical Vortex Generators Now for Transition Delay. *Phys. Rev. Lett.* 109, 074501.
- THEOFILIS, V. 2003. Advances in global linear instability analysis of nonparallel and three-dimensional flows. *Prog. Aerosp. Sci.* 39, 4, 249–315.
- TOLLMIEEN, W. 1929. Über die Entstehung der Turbulenz. 1. Mitteilung *Nachr. Ges. Wiss. Göttingen, Math. Phys. Klasse*, 21–44.
- TOLLMIEEN, W. 1935. Ein allgemeines Kriterium der Instabilität laminarer Geschwindigkeitsverteilungen. *Nachr. Ges. Wiss. Göttingen, Math. Phys. Klasse, Fachgr. I 1*, 79–114.
- TUMIN, A. AND RESHOTKO, E. 2004. The problem of boundary-layer flow encountering a three-dimensional hump revisited. In *42nd AIAA Aerosp. Sci. Meet. Exhib.* AIAA 2004-101. Reno, Nevada.
- VAUGHAN, N. J. AND ZAKI, T. A. 2011. Stability of zero-pressure-gradient boundary layer distorted by unsteady Klebanoff streaks. *J. Fluid Mech.* 681, 116–153.

- WESTIN, K. J. A., BOIKO, A. V., KLINGMANN, B. G. B., KOZLOV, V. V., AND ALFREDSSON, P. H. 1994. Experiments in a boundary layer subjected to free stream turbulence. Part 1. Boundary layer structure and receptivity. *J. Fluid Mech.* 281, 193–218.
- WHITE, E. B. 2002. Transient growth of stationary disturbances in a flat plate boundary layer. *Phys. Fluids* 14, 12, 4429–4439.
- WHITE, E. B. AND ERGIN, F. G. 2003. Receptivity and transient growth of roughness-induced disturbances. In *33rd AIAA Fluid Dyn. Conf. Exhib.* AIAA 2003-4243. Orlando, Florida.
- WIEGAND, T. 1996. Experimentelle Untersuchungen zum laminar-turbulenten Transitionsprozeß eines Wellenzuges in einer Plattengrenzschicht. Ph.D. thesis, Universität Stuttgart.
- WÖRNER, A. 2004. Numerische Untersuchung zum Entstehungsprozess von Grenzschichtstörungen durch die Interaktion von Schallwellen mit Oberflächenrauigkeiten. Ph.D. thesis, Universität Stuttgart.

Curriculum Vitae

Name Shin Yong-su
Date of birth November 7th, 1978
Place of birth Seoul, Korea Republic
Nationality Korean

1997-2000 B.S. in Mechanical Engineering, Hanyang University
(Ansan, Korea Republic)

2001-2003 Military Service, Field artillery officer, Korean Army

2004-2005 M.Sc. in Mechanical Engineering, Hanyang University
(Seoul, Korea Republic)

2007-2013 Research Assistant, Institute for Aerodynamics and Gas
Dynamics, University of Stuttgart *(Stuttgart, Germany)*

2015- Senior Research Engineer, Aerodynamic Development
Team, Hyundai Motor Company *(Hawseong, Korea Re-
public)*